UNIVERSITAT POLITÈCNICA DE VALÈNCIA
Departamento de Comunicaciones

Scalability analysis and designs for large-scale programmable rf-photonic integrated circuits: Modelling, design and implementation

Ph. D. Thesis

by

Erica Sánchez Gomariz

Supervisors:

José Capmany Francoy
Daniel Pérez López
Prometheus DasMahapatra

Valencia, November 2023

Universitat Politècnica de València

Institute of Telecommunications and Multimedia Applications

Photonics Research Labs

8G Building
Cno. de Vera, s/n
46022, Valencia
Spain

Tel: +34 963879580

Web: www.iteam.upv.es - www.prl.upv.es

E-mail: info@iteam.upv.es

"Aprendí que lo difícil no es llegar a la cima,
sino jamás dejar de subir."
- Walt Disney

Thesis Reviewers:
David Marpaung
Maurizio Burla
Guillermo Carpintero

About the author

Erica Sánchez Gomariz received a B.Sc. degree in telecommunications technology engineering from the Universidad Miguel Hernández de Elche, Elche, Spain, in 2016. At the same time, she also did two internships, at Bioengineering Institute and Signal and Communications Theory Department of the same university.

Then, she obtained an M.Sc. degree in telecommunication technologies, systems, and networks from the Universitat Politècnica de València, València, Spain in 2017.

In 2018, she started her Ph. D. and joined the Photonic Research Labs (PRL) group at Instituto de Telecomunicaciones y Aplicaciones Multimedia (iTEAM) of the Universitat Politecnica de Valencia, Valencia, Spain. Her Ph. D. is focused on integrated photonics. Specifically, in system scalability, evolution, and performance of future programmable photonic integrated circuits.

Currently, she has started working as an application and software engineer at iPronics Programmable Photonics. S.L.

She can be contacted at ersango@iteam.upv.es and erica.sanchez@ipronics.com

OrCID: 0000-0002-3221-9926

Webs: www.prl.upv.es, www.ipronics.com

Valencia, Spain, November 2023

Acknowledgments

Llegado este momento y aunque una de mis expresiones favoritas es "¡Qué sola!" sé que tengo mucha gente a mi alrededor a la que agradecer haber llegado hasta aquí.

Empezando por José Capmany, gracias por darme la oportunidad de, sin apenas conocerme, empezar este doctorado en un grupo de investigación tan top como el tuyo, el cual me ha permitido aprender todo lo que sé.

Esa oportunidad también se la debo a Daniel Pérez, gracias por guiarme, aconsejarme y enfocar mi cabezonería, en muchas ocasiones, para sacar lo mejor de mí. Gracias por confiar de nuevo en mi en esta nueva etapa, espero poder seguir aprendiendo de ti día a día.

A la que también le debo gran parte de esta Tesis es a Ana María Gutiérrez. Gracias *patrona* por estar siempre que te necesitamos sin importar cuantas tareas más estés haciendo en paralelo. Todo lo que sé de Laboratorio es gracias a ti. Gracias por hacer divertido el tiempo dentro y fuera del trabajo, has cambiado mi idea de "En el trabajo no se puede tener amigos de verdad". Sé que nos quedan muchas cosas por vivir y sé que las voy a seguir disfrutando contigo y con tu familia!

Hablando de laboratorio, tengo que dar las gracias al "Nini" de Luis Vallejo que, aunque se queje, siempre está para ayudarnos con cualquier experimento infernal que tengamos (aunque sea desde el lugar más remoto de Mordor), muchas de las cosas que sé sobre la RF son gracias a ti.

Como no hacer mención al otro doctorando que ha sufrido la ERC Grant tanto como yo, Aitor López gracias por tener siempre unas palabras bonitas cuando lo hemos necesitado. Sé que te va a ir genial en tu nueva etapa.

Sin olvidarme de Gloria Micó, Luis Bru y Jesús Benítez. El "Sala Piensa team", vosotros fuisteis los encargados de darme la bienvenida al grupo y de verdad que ha sido y es un placer compartir esta experiencia con vosotros.

Por supuesto, agradecer a "Los Huaweis", Cristina Catalá, José Rausell y Pablo Martínez-Carrasco, haberle devuelto la alegría al grupo. Y aunque a veces os odie y os quiera en la misma proporción vosotros habéis marcado la diferencia esta última etapa de mi Tesis. Ya sabéis que os sigo y os seguiré muuy de cerca, sois los siguientes, y por supuesto ¿hoy se sale?.

También dar las gracias a Diego Pérez, por las fructíferas discusiones sobre links de microondas y modulaciones. Sé que en Málaga siempre están las puertas abiertas.

Dar las gracias a David Martínez y Marian Aguilar por devolver la gestión y organización al grupo y hacer que trabajar sea mucho más fácil.

Por último, agradecer al resto de compañeros del Photonic Research Lab (PRL) la ayuda que siempre están dispuestos a dar.

Mi cuban crew, en concreto Danaisy Prado, tener una amiga dentro del ITEAM ha sido un apoyo muy importante para mí. Gracias por meterme caña con la tesis (por mi bien). Esos "Nos vemos en la tercera planta?" después de un día/reunión dur@ me han dado la vida. Además, sé que vamos a seguir viviendo muchos momentos juntas.

The IPronics team, ha sido un placer poder compartir desarrollos con vosotros durante mi tesis. En especial, gracias al departamento de software por permitirme compaginar el final de mi tesis con la incorporación oficial a vuestra familia. También, agradecer a Juan Fernández su apoyo y consejos en esta última etapa. Eres un crack, capaz de contagiar la ilusión por la fotónica a todos los de tu alrededor. Es un orgullo ser parte de vuestro equipo.

Agradezco también al European Research Council (ERC) Advanced Grant UMWP-Chip, a la Universitat Politècnica de València y a iPronics, Programmable Photonics S.L. por hacer posible la realización de este trabajo.

Por otro lado, en lo personal quiero agradecer el apoyo incondicional que siempre tengo de mis amigas: Anita, Vasiliki, Naiara, Youmana y Sarai. Sinceramente, podría escribiros una tesis a cada una, en concreto a Youmana y Sarai, pero creo que sabéis de sobra lo que significáis para mí, así que solo diré gracias, estoy orgullosa de teneros.

Por último, pero no menos importante, darle las gracias a mi familia. Especialmente a mis padres, sin su apoyo y educación nunca podría haber llegado tan lejos.

Abstract

Microwave photonics brings together the worlds of radiofrequency engineering and optoelectronics and it has attracted great interest in the last few decades. It added value stems from the fact that, on one hand, it enables the realization of key functionalities in microwave systems that either are complex or even not directly possible in the radiofrequency domain. On the other hand, it creates new opportunities for information and communication systems and networks. Hence, microwave photonics is used to enable specialized functions such as high-frequency signal generation, modulation, and signal processing, particularly in communication, radar, and sensing applications.
In the context of programmable photonics, versatility emerges by allowing dynamic manipulation of light signals, making them adaptable for generic purposes across optical networks, optical computing, adaptive optics, research and development, and quantum photonics. Then, it provides a flexible platform for optical applications, showcasing their complementary roles in modern photonics technology.

Hence, programmable photonic integrated circuits have been recently proposed and promise to be a solution to compete with application-specific designs. However, current demonstrations and proof-of-concepts have only integrated a limited number of components and represent small and moderate-complex circuits.

This work aims to answer the questions dealing with the system scalability and evolution of future programmable photonic integrated circuits. The analysis and proposal of solutions will include two main parts: the first one will study the scalability of programmable circuits in terms of system integration, including a comprehensive study of optical interfacing. Secondly, due to the need for loss compensation that arises when using integrated photonics, we will consider the performance of end-to-end analytical microwave photonics models with amplified links (optical power budget, signal noise, microwave photonic links key performance indicators, and power consumption). Once completed, we will make use of moderate complexity designs to evaluate our performance estimators for both optical signal processing and microwave photonic applications.

Resumen

La fotónica de microondas, la cual une los mundos de la ingeniería de radiofrecuencia y la optoelectrónica, ha generado un gran interés en las últimas décadas. Su valor añadido se deriva del hecho de que, por un lado, permite la realización de funcionalidades clave en los sistemas de microondas que son complejas o directamente imposibles en el dominio de la radiofrecuencia. Por otro lado, crea nuevas oportunidades para los sistemas y redes de información y comunicación. Por lo tanto, la fotónica de microondas se utiliza para habilitar funciones especializadas como generación de señales de alta frecuencia, modulación, procesamiento de señales, particularmente en aplicaciones de comunicación, radar y detección.

En el contexto de la fotónica programable, la versatilidad surge al permitir la manipulación dinámica de las señales de luz, haciéndolas adaptables para propósitos genéricos a través de redes ópticas, computación óptica, óptica adaptativa, investigación y desarrollo y fotónica cuántica. Por lo que, proporciona una plataforma flexible para aplicaciones ópticas, mostrando funciones complementarias a la tecnología fotónica moderna.

Por lo tanto, los circuitos integrados fotónicos programables proponen y prometen ser una solución para competir con diseños específicos de aplicaciones. Sin embargo, las demostraciones actuales y las pruebas de concepto solo han integrado un número limitado de componentes y representan circuitos de complejidad pequeña y moderada.

Este trabajo tiene como objetivo responder a las preguntas relacionadas con la escalabilidad del sistema y la evolución de futuros circuitos integrados fotónicos programables. El análisis y propuesta de soluciones constará de dos partes principales: la primera estudiará la escalabilidad de los circuitos programables en términos de integración de sistemas, incluyendo un estudio exhaustivo de las interfaces ópticas. En segundo lugar, debido a la necesidad de compensación de pérdidas que surge al utilizar fotónica integrada, consideraremos el rendimiento de modelos analíticos de fotónica de microondas de extremo a extremo con enlaces amplificados (balance de potencia óptica, ruido de señal, indicadores clave de rendimiento de enlaces fotónicos de microondas y consumo de energía). Una vez completado, utilizaremos diseños de complejidad moderada para evaluar nuestros estimadores de rendimiento tanto para el procesamiento de señales ópticas como para aplicaciones fotónicas de microondas.

Resùm

La fotònica de microones, la qual uneix els mons de l'enginyeria de radiofreqüència i l'optoelectrònica, ha generat un gran interés en les últimes dècades. El seu valor afegit es deriva del fet que, d'una banda, permet la realització de funcionalitats clau en els sistemes de microones que són complexes o directament impossibles en el domini de la radiofreqüència. D'altra banda, crea noves oportunitats per als sistemes i xarxes d'informació i comunicació. Per tant, la fotònica de microones s'utilitza per a habilitar funcions especialitzades com a generació de senyals d'alta freqüència, modulació, processament de senyals, particularment en aplicacions de comunicació, radar i detecció.

En el context de la fotònica programable, la versatilitat sorgeix en permetre la manipulació dinàmica dels senyals de llum, fent-les adaptables per a propòsits genèrics a través de xarxes òptiques, computació òptica, òptica adaptativa, recerca i desenvolupament i fotònica quàntica. Pel que, proporciona una plataforma flexible per a aplicacions òptiques, mostrant funcions complementàries a la tecnologia fotònica moderna.

Per tant, els circuits integrats fotònics programables proposen i prometen ser una solució per a competir amb dissenys específics d'aplicacions. No obstant això, les demostracions actuals i les proves de concepte sol han integrat un nombre limitat de components i representen circuits de complexitat xicoteta i moderada.

Aquest treball té com a objectiu respondre a les preguntes relacionades amb l'escalabilitat del sistema i l'evolució de futurs circuits integrats fotònics programables. L'anàlisi i proposta de solucions constarà de dues parts principals: la primera estudiarà l'escalabilitat dels circuits programables en termes d'integració de sistemes, incloent-hi un estudi exhaustiu de les interfícies òptiques. En segon lloc, a causa de la necessitat de compensació de pèrdues que sorgeix quan s'utilitza fotònica integrada, considerarem el rendiment de models analítics de fotònica de microones d'extrem a extrem amb enllaços amplificats (balanç de potència òptica, soroll de senyal, indicadors clau de rendiment d'enllaços fotònics de microones i consum d'energia). Una vegada completat, utilitzarem dissenys de complexitat moderada per a avaluar els nostres estimadors de rendiment tant per al processament de senyals òptics com per a aplicacions fotòniques de microones.

Contents

List of Figures

List of tables

List of acronyms

ASPIC	Application-Specific Photonic Integrated Circuits
ADC	Analog-to-Digital Converter
ASE	Amplified Spontaneous Emission
BB	Building Block
BS	Bar State
BS	Base-Station
BUL	Basic Unit Length
CITC	Chip Integration Technology Center
CMOS	Complementary Metal-Oxide-Semiconductor
CO	Central Office
CP	Cross Phase
CROW	Coupled Resonator Optical Waveguide
CS	Cross State
CW	Continuous Wave
DBR	Distributed Bragg Reflector
DC	Direct Current
DFB	Distributed-Feed Back
DL-RAMZI	Dual Loaded Ring-Assisted Mach-Zehnder Interferometer
DP-MZM	Dual Parallel Mach-Zehnder Interferometer
DSP	Digital Signal Processor
EAM	Electro-Absorption Modulator
EDFA	Erbium Doped Fiber Amplifier
EO	Electro-Optic
EOPM	Electro-Optic Phase Modulator
ER	Extinction Ratio
FIR	Finite Impulse Response
FoM	Figure of Merit
FPGA	Field Programmable Gate Arrays
FPPGA	Field Programmable Photonic Gate Arrays
FP-SOA	Fabry-Perot Semiconductor Optical Amplifier
FR	Front Reflector
FSR	Free Spectral Range
G	Gain
GaAs	Gallium arsenide
GDS	Graphic Data System
GPIB	General Purpose Interface Bus
GSG	Ground Signal Ground
HHI	Heinrich-Hertz-Institut
IF	Front Isolation
IIR	Infinite Impulse Response
IL	Insertion Loss

IM	Middle Isolation
IMD	Inter-Modulation Distortion
IMWP	Integrated Microwave Photonics
InP	Indium phosphide
IoT	Internet of Things
IQ	In-phase and Quadrature
IR	Rear Isolation
K	Coupling Factor
LCA	Lightwave Component Analyzer
LiNbO3	Lithium niobate
LIV	Light-Current-Voltage
MEDA	Multichannel Electrical Driving Array
MEMA	Multichannel Electrical Monitoring Array
MFD	Mode Field Diameter
MMI	Multi-Mode Interferometer
MPW	Multi Project Wafer
MQW	Multiple-Quantum-Well
MWP	Microwave Photonics
MWPL	Microwave Photonic Link
MW-PSP	Microwave Photonic Signal Processor
MUA	Monitoring Unit Array
MZI	Mach-Zehnder Interferometer
N	Noise Power Spectral Density
NF	Noise Figure
OA	Optical Amplifier
OADM	Optical Add-Drop Multiplexer
OE	Opto-Electric
OIP	Output Intercept Point
ORR	Optical Ring Resonator
OSA	Optical Spectrum Analyzer
PC	Polarization Controller
PD	Photodetector
PDK	Process Design Kit
PIC	Photonic Integrated circuit
PMCI	Current-Injection Phase Modulator
PMP	Programmable Multifunctional Photonics
PNA	Performance Network Analyzer
PP	Programmable Photonics
PS	Phase Section
PUC	Programmable Unit Cells
QCSE	Quantum-Confined Stark Effect
RAMZI	Ring-Assisted Mach-Zehnder Interferometer
RF	Radio Frequency
RIN	Relative intensity noise

RR	Rear Reflector
SCISSOR	Side-Coupled Integrated Spaced Sequence of Optical Resonators
SFDR	Spurious Free Dynamic Range
Si3N4	Silicon Nitride
SL-RAMZI	Single Load - Ring-Assisted Mach-Zehnder Interferometer
SMF	Single-Mode Fiber
SNR	Signal to Noise Ratio
SOA	Semiconductor Optical Amplifier
SOI	Silicon-On-Insulator
SSC	Spot Size Converters
TC	Tunable Coupler
THz	TeraHertz
TW-SOA	Travelling-Wave Semiconductor Optical Amplifier
UMZI	Unbalanced Mach-Zehnder Interferometer
VSG	Vector Signal Generator
WLAN	Wireless Local Area Networks

Chapter 1. Structure and Thesis Objectives

1.1. Motivation

Photonics, a multidisciplinary field focused on the generation, manipulation, and transmission of light particles known as photons, encompasses a wide array of technologies. This field, which includes lasers, optical fibers, and various photonic devices, finds applications in telecommunications, medical imaging, and sensing. Within this diverse area, Microwave Photonics (MWP) stands out as a specialized subfield that merges microwave and optical technologies. MWP exploits the unique characteristics of microwaves and photons to create high-speed communication systems for civil applications, including wireless communication [4], satellite communications [5], distributed antenna systems [6], optical signal processing [10], medical imaging using terahertz (THz) waves and optical coherence tomography techniques [8].

The demand for ever-increasing speed, bandwidth, and dynamic range in these novel applications necessitates devices that are not only fast but also compact, lightweight, low-power, highly tunable, and resistant to electromagnetic interference. Consequently, future networks are expected to support high data rates, making energy-efficient solutions like pico- or femtocells a viable alternative to traditional macrocell networks, which require high-power base stations.

Traditionally, MWP signal processors and links have relied on discrete optoelectronic devices and standard optical fibers, resulting in configurations that are large, expensive, and power-intensive, with limited flexibility [1]. However, the emergence of Integrated Microwave Photonics (IMWP), aimed at incorporating MWP components/subsystems into photonic circuits, offers promising solutions. IMWP, an area of active scientific and technical research, is crucial for developing both cost-effective and advanced analog optical front-ends. Efforts in this field have explored various technologies, including III-V semiconductors [2], hybrid configurations [3]–[5], silicon [4], [5], and Si3N4 (TripleX) [6] technologies, focusing on applications like filtering, broadband tunable phase shifters, and true time delay lines. Other MWP functionalities have also been demonstrated by partially using integrated circuits. For example, broadband tunable phase shifters and true time delay lines have been reported based on cascaded Semiconductor Optical Amplifiers (SOAs) devices [7], [8], passive silicon on insulator [9], and Si3N4 [10] optical rings, and passive III-V photonic crystal waveguides.

While integrated microwave photonics solutions have made strides, most developments have been centered around Application Specific Photonic Integrated Circuits (ASPICs). These ASPICs, optimized for specific applications and technology platforms, often result in cost-inefficient processes for a wide range of applications. Recognizing these limitations, the field of integrated Programmable Photonics (PP) has emerged, enabling the reconfiguration and programming of photonic integrated circuits to accommodate multiple applications [11]–[15]. This approach has led to the creation of complex reconfigurable circuits that can adapt to different circuit topologies and applications based on software control.

However, the advent of programmable photonics, particularly in its application to RF-photonics, poses several challenges. The scalability of proposed structures,in terms of performance, losses and system integration, raises crucial questions. The complexity of these circuits necessitates lengthy and costly iterations, slowing down progress. Additionally, the lack of simulation and design frameworks compatible with the flexibility of this technology has hampered developments, creating uncertainty around its practical applications.

To address these challenges, there is a critical need for a comprehensive end-to-end model encompassing optical signal amplification, microwave photonic signal processing, and arbitrary waveguide mesh arrangements. Such a model would not only assist future designers but also enable the development of accurate performance estimation models. This holistic approach is essential for identifying and overcoming the limits of large-scale programmable Photonic Integrated Circuits (PICs), propelling the field forward and paving the way for practical applications.

1.2. Thesis Objectives

The objective of this thesis is to enable large-scale, programmable photonic integrated circuits for analogue signal processing, providing the required flexibility and scalability to perform optical signal and microwave photonic processing along with real-time reconfiguration and characterization specific to a wide variety of applications. This implies the identification of the limitations in programmable photonic integrated circuit design and architectures and propose solutions to enable their future evolution.

The structure for the work to be developed is based on the architecture of a general reconfigurable Microwave Photonic Signal Processor (MWPSP). The first goal is to study the scalability limits arising from the design of large-scale MWP and optical signal processor, that can perform all the main functions carried by current MWP and optical systems by suitable programming and reconfiguration of its elements. The starting point for this objective is the previously proposed concept of programmable photonic integrated circuit and field programmable photonic gate arrays [11]–[15], which is composed of subsystems, each of which is a collection of connected fixed-and-variable components. This architecture is in principle capable of performing multiple optical and microwave photonic signal processing functionalities provided that its optical subsystems can be reconfigured by means of suitable control signals. The main limitation of the present architecture is however that the complexity of the circuits that can be programmed depends on the number and performance of its integrated reconfigurable resources.
Although moderate-complex systems relying on this architecture have shown promising results, current demonstrations are limited by dozens of integrated resources. Since large-scale programmable PICs would extend the capabilities of current demonstrations the scope of this thesis is to study which applications would benefit from their emulation in a programmable PIC and to identify and address the main scalability limits.

Afterward, microwave photonics links and systems end-to-end theoretical analysis activity will be developed to get complete characterization examples of the main overall Figures of Merit (FoM) (Radio Frequency (RF) Power Gain, Noise Figure (NF), and Dynamic Range) of the structures in terms of the parameters defining each of its constituents. As a consequence of this, a functional top-level design framework will be produced.

To accomplish these objectives, the work is structured as follows:

Chapter 2, titled "Fundamentals of Microwave Photonics," provides a comprehensive overview of photonics and its applications in microwave photonic links and systems. We began by outlining the essential parameters for evaluating the performance of discrete microwave photonic systems. Recognizing the limitations of these systems, such as cost, size, and power consumption, the discussion emphasizes the advantages of integrated microwave photonics as a viable solution for overcoming these constraints.

The text delves into the benefits offered by integrated photonics and offers a brief survey of various integration platforms. Additionally, the chapter explores the potential of integrated programmable photonics, highlighting its superior flexibility when compared to application-specific photonic integrated circuits.

A significant portion of the chapter is dedicated to addressing a key challenge in integrated photonics: high losses. To mitigate this issue, the chapter proposes a practical solution involving the incorporation of optical amplifiers. These amplifiers are examined in detail, evaluating their impact on the overall system behavior.

In summary, the chapter not only outlines the fundamentals of microwave photonics but also underscores the importance of integrated solutions, exploring their benefits and providing innovative approaches to enhance their performance, making it a valuable resource for readers interested in this field.

Chapter 3, titled "Scattering Matrix Generator of Complex Photonic Integrated Circuits," presents groundbreaking contributions to the field through the introduction of a novel computational method based on the single-cell inductive approach methodology. This innovative technique has been instrumental in advancing our understanding of complex photonic integrated circuits.

The chapter systematically compares the newly developed computational method with two existing approaches, assessing computational times and accuracy trade-offs across various typical application examples and circuit sizes. Through rigorous analysis, it becomes evident that the inductive methodology excels, especially in scenarios involving numerous optical paths and a high volume of feedback and feedforward loops. In such situations, the inductive methodology not only ensures superior simulation quality but also significantly reduces simulation times. This speed advantage becomes particularly critical in the context of complex circuits with a large number of optical ports.

The significance of this research lies in its ability to enhance our comprehension of intricate systems at the single-cell level. The innovative approach not only outperforms existing methods but also covers the way for a more profound scalability analysis. Consequently, this chapter not only contributes to the scientific knowledge in the field but also offers a valuable framework for researchers and practitioners seeking to explore the complexities of photonic integrated circuits.

Chapter 4, titled "End-to-End Analytical Model of Amplified Links," presents a significant contribution to the field by developing two comprehensive models. The first model involves the derivation of an intensity modulation with direct detection simulator, aimed at evaluating the figure of merits for filtered microwave photonic link systems incorporating optical amplifiers. This mathematical derivation is then translated into a Python program and applied to discrete and integrated realistic scenarios. These scenarios include a microwave photonics optical fiber link and MWP integrated systems with reconfigurable

integrated filters. The analysis focuses on determining the optimal position for adding the optical amplifier gain in these setups.

In parallel, following a similar methodology, the chapter also presents a model for MWP links employing I-Q modulation and balanced detection. This configuration offers an advantage by canceling out or suppressing common-mode noise sources typically found in direct detection systems. The model is applied to a specific case representing the front-haul segment in a 5G link between the central office and the base station. Three examples with varying optical input powers and amplifier gain values are evaluated, demonstrating the versatility of the model.

In summary, the developed models offer a versatile and fast tool for analyzing a wide range of cases that combine optical amplification with fiber and photonic chip elements. These models not only calculate optical properties but also assess the performance metrics of chosen architectural configurations. Noteworthy in the field, this MWP model incorporates optical amplification and considers additional noise sources, marking a significant advancement. The model enhances our understanding and predictive capabilities in the realm of MWP systems, with far-reaching implications for applications in telecommunications, sensing, and optical signal processing.

1.2.1. Original contributions of this Thesis

In this thesis, we introduce a computational method founded on mathematical induction coupled with a single-cell modelling methodology. This innovative approach can be applied to highly complex photonic circuit topologies, including square, hexagonal, triangular, and feedforward configurations, providing a versatile tool for studying the scalability of emerging multipurpose programmable photonic processors.

Then, our work also lies in the development of a comprehensive end-to-end Microwave Photonics (MWP) analytical and numerical model. This model not only calculates the optical and RF performance metrics of the chosen architecture but also incorporates optical amplification and related noise into a programmable microwave photonic structure. This integration of optical amplification and noise factors within a programmable framework represents a significant leap forward in the field, as it allows for the evaluation of scalable optical programmable systems.

Furthermore, our research extends beyond theoretical realms. We conduct rigorous experimental validations involving diverse MWP links with varying degrees of integration. Through detailed comparison between the tools performance estimations and the results obtained in the laboratory, we establish the reliability and effectiveness of our computational method in real-world scenarios.

In summary, this thesis not only pioneers a novel computational methodology but also demonstrates its practical applicability through experimental validations. The integration of optical amplification and noise considerations into programmable microwave photonic structures opens new avenues for research and development, making a profound impact on the field of photonic processors and significantly advancing the understanding of scalable, multipurpose photonic systems.

Chapter 2. Fundamentals of Microwave Photonics

2.1. Introduction

Microwave photonics is a multidisciplinary field that involves optical, microwave, and electrical engineering [16]. It is focused on the application of photonic methods in generating, controlling, processing, and transmitting microwave signals [17]. This microwave signal refers to an electromagnetic wave with a frequency typically ranging from 300MHz to 300GHz. As can be seen in Figure 2.1, it falls in the frequency range between radio waves and infrared radiation in the electromagnetic spectrum.

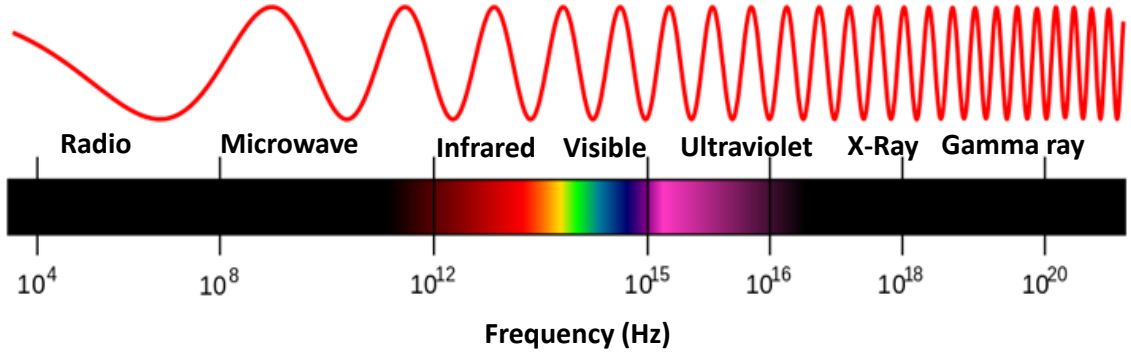

Figure 2.1. Electromagnetic spectrum.

Microwaves are widely used for communication, especially in technologies such as satellite communication or wireless local area networks (WLANs). In addition, microwaves are also used in applications such as radar, remote sensing, and medical treatments. Microwave signals have a shorter wavelength and higher frequency than radio waves, making them suitable for high-speed data transfer over short distances. Nowadays, the most employed method for these applications is low-speed electronics. Nonetheless, its speed is restricted to a few GHz due to the electronic sampling rate. As a result, photonics distinctive features producing and handling ultra-wideband, high-frequency microwave signals offer a promising alternative for wideband microwave applications. In this chapter, we will cover the fundamental principles of microwave photonics, which will include an overview of a microwave photonics links structure and its performance metrics, along with their figures of merit. Moreover, we extend our reach by explaining how microwave links can be transfer into a technology that integrates multiple optical components on a single chip, enabling compact optical systems. Given the ever-increasing need for flexible and adaptable optical systems that can respond to changing demands and applications emerge, we follow up the work by analyzing the inclusion of programmable photonic engines to a microwave photonic. Anticipating that these integrated systems have high losses as a main drawback, in this work, we will analyze a solution to this problem by using semiconductor optical amplifiers.

2.1.1. Microwave Photonic Links and systems

It should be noted that an essential element of any system or network for distributing radio frequency signals via optical methods is the microwave photonic link [18]. Figure 2.2 shows

a typical configuration of an MWP link, which we will use to introduce several fundamental concepts.

As can be seen in Figure 2.2, RF signals are injected into the modulator at frequencies f_{RF1} and f_{RF2}. Then, the light, from an optical source, is modulated to up-convert the spectrum to the optical region. So, now it is centered at $\omega + f_{RF1}$ and $\omega + f_{RF2}$, where ω, is the central frequency of the laser. After that the optical signal can be processed, filtered…etc. by optical systems. These optical elements can be used to transform the spectral features of the input signal. Consequently, the simplicity or complexity of the configuration will depend on the transfer function $H(\omega)$ of the system. Finally, an optical receiver, usually a photodetector (PD) is used for the frequency down-conversion. This device is a p-n junction that converts the energy of the light into electric current depending on its efficiency, defined as responsivity ($\Re$). The PD beat the optical sidebands of the spectrum with the optical carrier to recover the RF signal after being performed by the MWP link [3].

As an example, an input RF tone with a RF frequency is introduced into the link, the resulting output RF signal consists of three elements. Firstly, there is the desired input tone itself, which presents a low amplitude due to losses within the system. Secondly, there is noise that is distributed across a specific spectral range. Lastly, there are nonlinear harmonic distortion components that emerge at multiples of the RF frequency. These three phenomena determine the quality of the Microwave Photonic Link (MWPL) and can be quantified figures of merit.

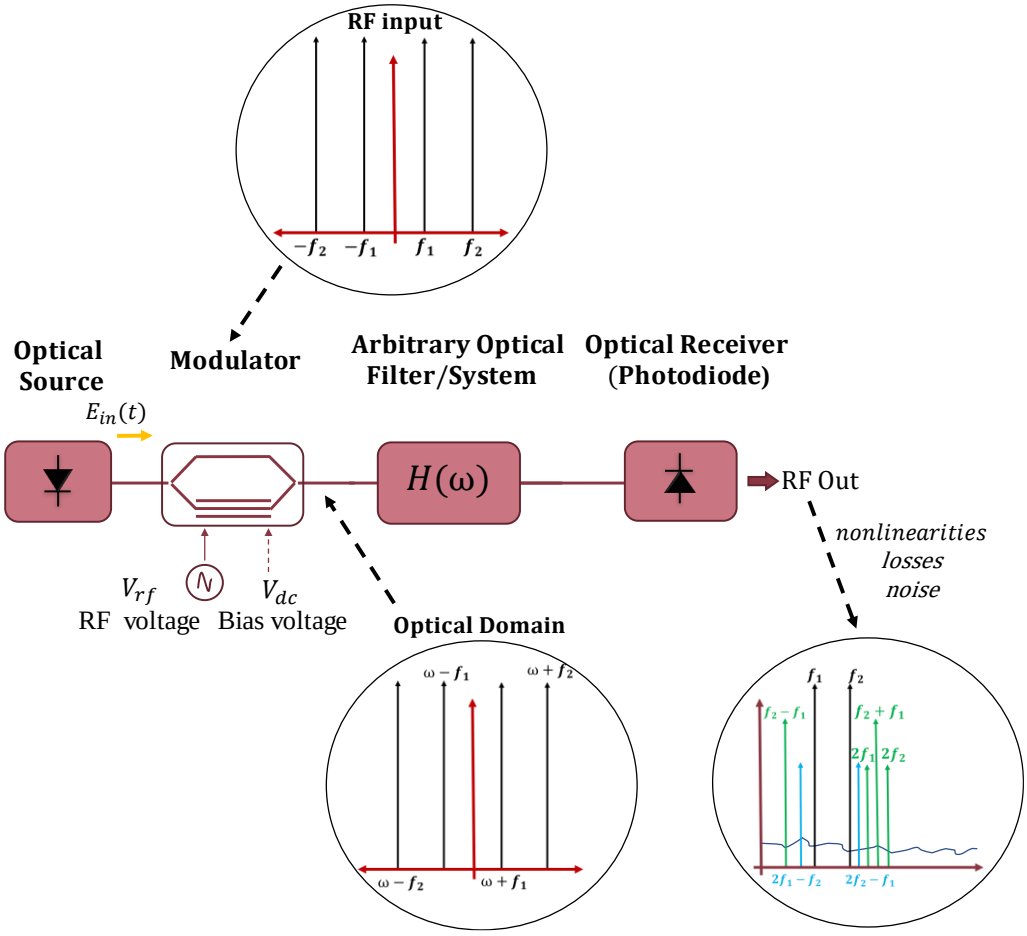

Figure 2.2. Diagram of a typical Microwave Photonic Link.

2.1.2. Figures of merit

Figures of Merit in a microwave link refer to quantitative measures or parameters used to evaluate the performance and quality of the link. These metrics provide valuable insights into various aspects of the links functionality, efficiency, and overall performance. In the context of a microwave link, common figures of merit include metrics such as link Gain (G_{RF}), Noise Figure (NF), Spurious-Free Dynamic Range (SFDR), Signal-to-Noise Ratio (SNR), and Inter-Modulation Distortion (IMD). These FoMs help to evaluate and compare the performance of microwave links in terms of their ability to transmit and receive signals accurately, efficiently, and with minimal degradation. In Chapter 4, we provide a more detailed definition of them.

2.2. Integrated MWP

Microwave links as we know them historically are made up of discrete components, which give us a wide variety of functionalities. However, they are limited by their complexity, high costs, and power consumption. This is where integrated links become relevant [18].

The main challenge of MWP is to decrease costs, size, and power consumption. Properly integrating photonics with electronics in architectural design choices has the potential to revolutionize the scaling laws of high-bandwidth systems. This synergy of photonics and electronics enables optimization of performance, power, footprint, and overall cost-effectiveness. In addition, integrated microwave photonics offers much more than this because the fact of confining the light to a smaller space enhances its interaction, originate often non-linear effects. These events, jointly with the evolution towards new concepts such as reconfigurability, can make IMWP achieve good performances such as modulation bandwidth, spectral resolution, noise efficiency, and reconfigurability.

2.2.1. Photonics Technology Platforms

Depending on the integration platform chosen the applications, performance, and size of the photonic integrated circuit will change. Initially, integrated MWP was showcased in a wide group of materials, such as Gallium Arsenide (GaAs), Lithium Niobate (LiNbO3), and doped silica. However, in recent years, the majority of integrated MWP circuits have predominantly relied on three key platforms for monolithic integration: indium phosphide (InP), silicon-on-insulator (SOI), and silicon nitride (Si3N4) as you observe in Figure 2.3 (a-c) respectively [17], [18]. These materials platforms have achieved the necessary level of maturity to be regarded as practical choices for realizing photonic integrated circuits. The circuits can take the form of monolithic, hybrid, or heterogeneous designs. Moreover, in the main working within the wavelength ranges of 1.3 and 1.55 μm [11], [18]. Hence, we start providing a brief overview of these photonic technologies:

- **Indium Phosphide**: It is the only platform that permits the monolithic integration of diverse active and passive photonic components like lasers, modulators, optical amplifiers (OA), tunable devices, and photodetectors. Moreover, this platform facilitates the development of compact circuits due to present a large list of available components for integrations (e.g., passive optical filters, arrayed waveguide gratings, Semiconductor Optical Amplifiers, optical sources, etc.). However, the drawback of this material is that optical waveguides have relatively high losses, and it presents problems in the integration with electronics in the same PIC [17], [18].
- **Silicon-On-Insulator:** Within the scope of this technology the waveguides can exhibit a wide range of losses and minimum bend radius depending on the thickness of the silicon layer and the geometry of the waveguides. Also, it shows strong third-

order optical nonlinearities, which can be advantageous for ultrafast signal processing, but it can suffer from high non-linear loss. Therefore, it is not a recommended material for light sources, optical modulators, or photodetectors. Although using doping, high-speed modulators and photodetectors have been demonstrated [11], [17]. Nonetheless, the main advantage of SOI lies in its potential suitability with Complementary Metal-Oxide-Semiconductor (CMOS) fabrication procedures, thereby enabling the integration of electronic and photonic components on a single chip with a small footprint.

- **Silicon Nitride:** Waveguides are gaining in popularity due to the potential for ultra-low loss operation. As based on layer deposition, post-manufacturing processing, and geometry, silicon nitride waveguides can be easily adapted to exhibit ultra-low propagation loss and be compact. In addition, the nonlinear coefficient of silicon nitride is about ten times smaller than that of silicon. However, active elements such as lasers, modulators, and detectors can only be built on this passive material through hybrid integration with other material platforms such as indium phosphide, graphene, or piezoelectric materials [17].

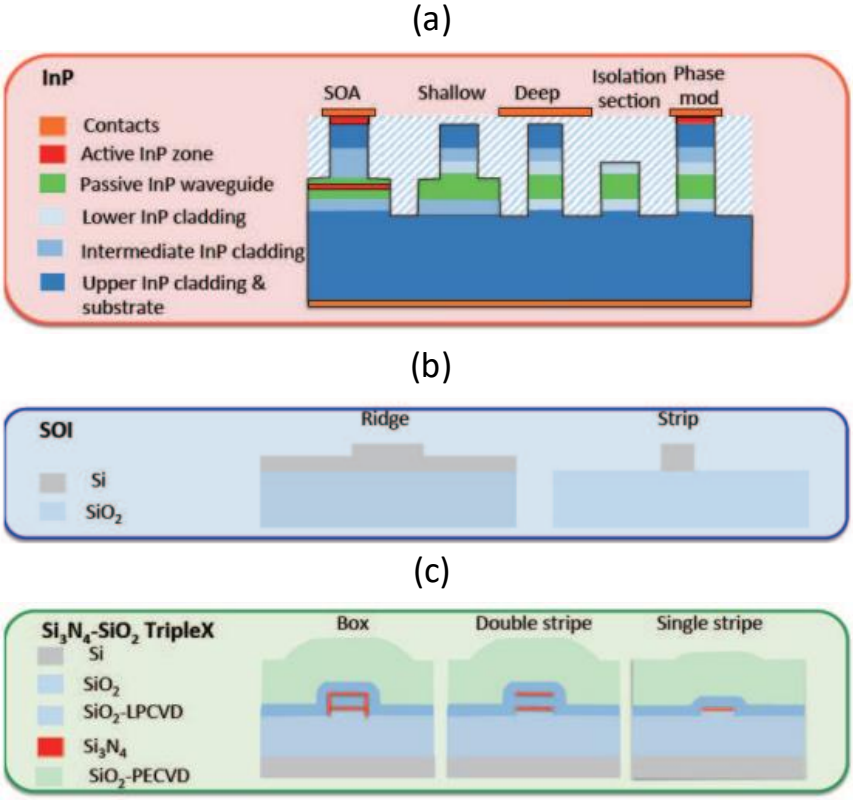

Figure 2.3. Example of the structure of a waveguide in (a) InP, (b) SOI, and (c) Si3N4-SiO2 platforms.[18]

2.3. Programmable photonics

Till now, IMWP has centred on what is known as application-specific photonic integrated circuits. These involve creating a circuit designed for a very particular and limited function in microwave photonics. Therefore, this tendency is causing a division, as the number of different technological solutions is almost as numerous as the applications, they are meant for [18].

The demonstration of successful multifunctional circuit operation in numerous ASPICs designs makes us question if we can create a simple and easy-to-repeat photonic hardware architecture. This architecture, when suitably programmed, holds the potential to execute the diverse functionalities essential for microwave photonics. This concept of programmable integrated microwave photonics draws inspiration from ideas like the electronics Field Programmable Gate array (FPGA) device or the advanced communications Digital Signal Processor (DSP) [18].

Programmable photonics emerges due to the need for flexible optical systems that can be dynamically reconfigured to meet specific application requirements. A completely characteristic approach involves a universal MWP signal processor that can be integrated into a single chip. This processor could then be programmed to carry out a range of functions. Consider it like how field-programmable gate arrays work in the electronics world. These use a single hardware platform that can be reconfigured through software to handle a wide array of tasks, see an example in Figure 2.4.

The main part of the programmable optical processor is its optical core (see Figure 2.4. (a)). At this point, the basic signal processing operations happen using photonics. Ideally, this optical core should be designed with a versatile structure that can carry out different functions based on various electronic control signals (observe Figure 2.4. (c-d)). In actual applications, from the reconfigurable photonic circuits suggested in prior literature, the ones that might be fitting for this core include those using a series of finite impulse response cells (like Mach-Zehnder Interferometers (MZI)) or infinite impulse response cells (like ring cavities), or even a mix of these approaches.

Nonetheless, the architecture, continues to face limitations in several aspects. Firstly, its flexibility is constrained, given that specially designed photonic subsystems must be integrated and linked within the optical core. Secondly, its scalability is limited by the use of predetermined size photonic components as fundamental component of more complex circuits. Lastly, it faces losses due to the significant number of optical routing and switching components that must be crossed to realize complex configurations [18], [19].

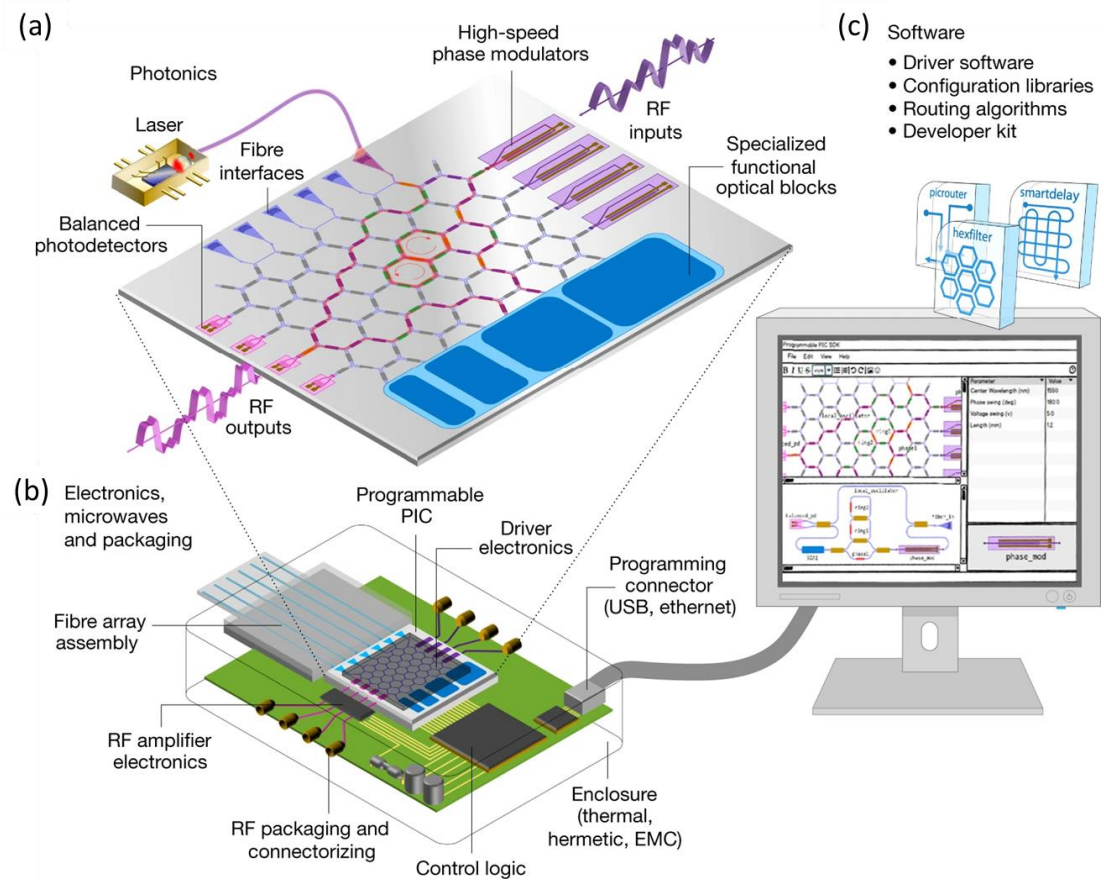

Figure 2.4. Programmable photonic integrated circuits require several functional layers. (a) Photonic chip has a programmable mesh of photonic gates connected to control electronics, optical fibres, and high-speed modulators and detectors to translate between the optical and microwave domains. (b) Photonic chip packaged together with analogue and digital driver electronics. (c) Software algorithms and programming layers give the user access to the photonic functionality. RF, radiofrequency [20].

2.3.1. Scalability

Scalability within programmable integrated photonics refers to the ability of processors aforementioned to efficiently accommodate growth and increased complexity as demands or requirements change. It involves the capacity to expand the waveguide mesh maintaining performance, flexibility, and functionality. In this context, it typically includes considerations for adding more waveguides, integrating additional components, and adapting the architecture to handle larger and more complex tasks without significant loss in efficiency or performance degradation. It is a key aspect when designing and employing programmable processors to ensure they can adapt to changing requirements with productivity and cost-effectiveness.

The relevance of the optical losses experienced by microwave photonic systems derives from the direct impact that they have on the radio frequency losses of RF schemes, which increases quadratically with this parameter. Therefore, most of the efforts during the development of embedded MWP prioritized the reduction of losses on the chip. In addition, improves the integration of numerous components within a single chip and the demonstration of device reconfiguration.

The large-scale programable processors are susceptible to accumulating more optical losses when compared to application-specific photonic integrated circuits. To mitigate these losses, on-chip amplifiers can be strategically placed, either within the waveguide network itself or off-chip. When integrated with a waveguide cavity, these amplifiers have the potential to constitute a programmable laser, or alternatively, their nonlinear characteristics can facilitate all-optical signal processing [20].

2.4. Principles of Semiconductor Optical Amplifiers

Integrated semiconductor optical amplifiers are a critical component of modern photonic integrated circuits, and they play a crucial role in applications in the field of photonics. These devices are typically fabricated using semiconductor materials and they are integrated into PICs alongside other optical components like waveguides, modulators, and detectors. Overall, integrated SOAs offer an alternative and efficient solution to compensate for insertion losses in PICs.

2.4.1. Operating principles

A semiconductor optical amplifier is an optoelectronic device capable of amplifying an input light signal under specific operating conditions. Its active region provides gain to the input signal, with an external electric current supplying as the energy source for this amplification process as shown in Figure 2.5. An embedded waveguide confines the propagating signal wave to the active region. Afterward, electrons and holes are introduced into the active region, generating a population inversion that facilitates the amplification of the input light [21]. As a result, the amplified output signal is inevitably accompanied by additive noise, a consequence of the amplification process itself, making complete noise elimination impossible [22].

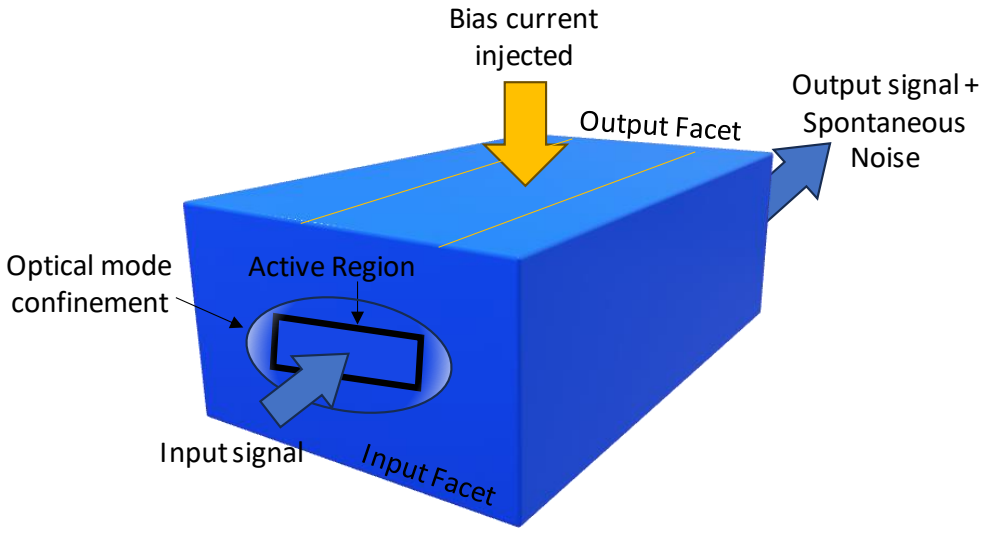

Figure 2.5. Schematic of a SOA.

SOAs are typically categorized into two primary types as defined in Figure 2.6. (a) Fabry-Perot SOAs (FP-SOA), where reflections from the end facets significantly impact the signal (multiple paths through the amplifier), and Figure 2.6. (b) Travelling-Wave SOAs (TW-SOA), where reflections are negligible (a single path through the amplifier) [22].

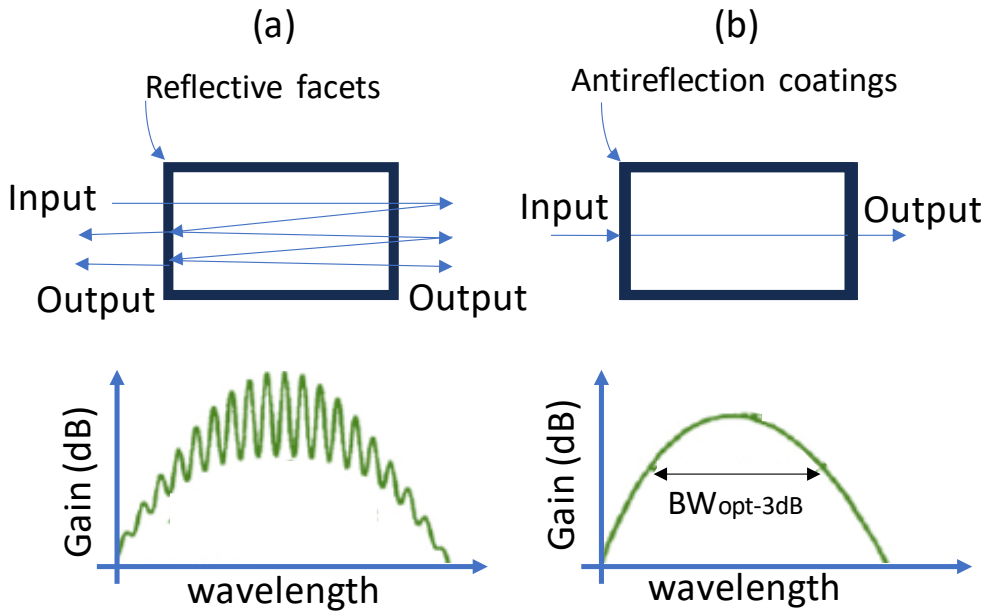

Figure 2.6. Schematics of the basic types of SOAs and their gain spectra (a) Fabry-Perot SOA, where you can see ripples in the gain spectrum caused by reflections at the end facets, and (b) Travelling-wave SOA, holds a smooth gain spectrum [22].

SOAs are typically made from semiconductor materials, like those used in lasers and diodes. Moreover, they are compact and can provide high gain. However, they are susceptible to nonlinear effects and may introduce noise, limiting their use in certain applications.

Chapter 3. Scattering matrix generator of complex photonic integrated circuits

3.1. Introduction

Programmable Multifunctional Photonics (PMP) enables the configuration of multiple optical and electro-optical processing operations employing reconfigurable photonic integrated platforms [23][12]. The core of the architecture relies on the interconnection of Programmable Unit Cells (PUC) -which can be implemented with Mach-Zehnder interferometers [24] or programmable directional couplers [15][25]. The architecture includes two phase actuators that can rely on a wide range of physical effects. Depending on the interconnection pattern, different programmable photonic circuit topologies have been demonstrated, as square [15], triangular [24][26] and hexagonal [13][27] arrangements. The application of these programmable photonic circuits provides a potential alternative to application-specific photonic integrated circuits implementing the main required functionalities in microwave photonic systems and radio-over-fiber transmission [15], [17]. It also supports the emulation of arbitrary linear transformations, a key operation in many other fields of application such as quantum processing [27], [28]–[34]], boson sampling [35]–[37] and neuromorphic computing [38], [39]. Hence, the support of these features -amongst many others- will allow this technology -in cooperation with current digital processing solutions- to become a key enabler of additional, enhanced signal processing schemes and applications. The resulting architecture enables the synthesis and discretization of optical circuit topologies within the programmable photonic cells, originating multipurpose photonic processors or Field Programmable Photonic Gate Arrays (FPPGAs) [14].

However, the performance of some of the previous applications is associated to the scalability and upgrade of current programmable circuits. In practice, there exist several limitations: footprint optimization [40], accumulated losses, imperfect coupling splitting ratios [41], phase control, parasitic back-reflections, loss imbalances, fabrication errors (gradients through the circuit in thickness or temperature) and drift in time [42]. This calls for efficient alternatives to check the viability of such circuits when employing current fabrication techniques and imperfect photonic components, as well as to provide a means for carrying out statistical analysis of their targeted performance to predict and avoid any possible issues arising, leading to significant cost reduction in hardware fabrication. In addition, the availability of reliable and efficient circuit simulation tools is mandatory to sustain and foster the development of programmable photonic circuit routines and automated tools.

On this front, the work proposed in [42] presented a simulation method for arbitrary photonic waveguide meshes and demonstrated its performance. The work relied on the inductive method derivation employing subsets (lattices) of waveguide meshes as primitive cells. The use of subsets limited the arbitrariness of the simulation method and demanded considerable customization efforts for alternative architectures. Moreover, computation efficiency was not reported.

Tackles this issue, this chapter is focused on the detailed procedure to compute the final dispersion matrix S(n) of a complex photonic integrated processor using an inductive single-cell approach method. This method is able to reproduce the spectral response of

any 2D arbitrary photonic circuit arrangement based on hyper-coupled cells. Then, in Section 3.3, we analyze and compare the computational elapsed times and key benefits and limitations between the inductive method developed here and a graph theory perspective, following the work introduced in [43], under different application scenarios.

3.2. Inductive method to compute the scattering matrix of arbitrary waveguide mesh arrangements

The method that we present in this chapter pursues the simulation of the frequency response (scattering matrix) of large-scale 2D waveguide meshes formed by programmable units cells. Following and upgrading the work [42], we employ an analogous strategy using mathematical inductive computation [44] that builds up the mesh iteratively adding pieces sequentially. The key differentiating factor is that previous works employ a set of PUCs connected in a Y-shape (Trilattice) as a basic building block. Here, we employ a single PUC as the basic building block, Figure 3.1. (a), allowing us to re-use the model for arbitrary waveguide topologies. This enables the implementation of meshes with different topologies (hexagonal, square, triangular, feedforward, etc. (see Figure 3.1. (b))) without the need to change the shape of the block that we are using as a base of the inductive method. For the remaining of the work, the single-cell approach is demonstrated on hexagonal meshes.

3.2.1. Analytical modelling

Firstly, we are going to explain the procedure to obtain the scattering matrix of hexagonal arbitraries waveguide meshes. Then, for each proposed interconnection scenario, its signal flow graph and the new structure scattering matrix obtained after the joint would be described.

To start, we need to define and model the scattering matrix of the PUC. This 2x2 device must be able to provide arbitrary splitting factors and phase response though the control of its phase actuators. The model of the PUC depends on its architecture. Specifically, it can be implemented with beamsplitters, phase actuators or tunable beamsplitters [15], [25]. However, the classical configuration employs a Mach-Zehnder Interferometer topology (Figure 3.1. (c)) which is loaded with a phase shifter on each arm. This tunable structure can synthesize three different states: Cross State (CS) where the light path connects port 1 to 3 and 0 to 2, Bar State (BS) switch where the input light follows a straight path connecting ports 1 to 2 and 0 to 3. Then, the third state is Tunable Coupler (TC) where you can control what ratio of light goes from the input port (for example port 1) to the output ports (in this case 2 and 3) tunning the phases of the heaters on the arms of the MZI, (observe Figure 3.1. (a)).

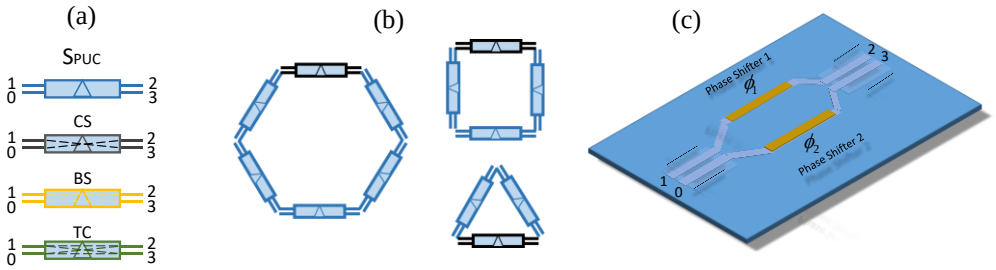

Figure 3.1. (a) Lattice/PUC used as a basic building block and different states in which it can be implemented (Cross State, Bar State, and Tunable Coupler State), (b) Interconnection of several PUCs forming closed cells with different topologies (hexagonal, squared, and triangular) using a single PUC as a basic building block and (c) MZI used to implement each programmable unit cell.

Moreover, to simplify the modeling, we can consider negligible backscattering or signal reflections as these will not dominate over optical crosstalk contributions. Eq. (3.1) represents the 4x4 scattering matrix (S_{PUC}) that models the internal behaviour of each PUC.

$$S_{PUC} = \begin{bmatrix} S_{00} & S_{01} & S_{02} & S_{03} \\ S_{10} & S_{11} & S_{12} & S_{13} \\ S_{20} & S_{21} & S_{22} & S_{23} \\ S_{30} & S_{31} & S_{32} & S_{33} \end{bmatrix} = -je^{-j\Delta} \begin{bmatrix} 0 & 0 & \cos\theta & -\sin\theta \\ 0 & 0 & \sin\theta & \cos\theta \\ \cos\theta & \sin\theta & 0 & 0 \\ -\sin\theta & \cos\theta & 0 & 0 \end{bmatrix} \cdot \alpha e^{-j\omega\tau} \quad (3.1)$$

where Δ is the sum of the phases of each arm of the MZI (Φ_1 and Φ_2) divided by 2, θ is the subtraction of these phases divided by 2, α are the Insertion Losses (IL) of the couplers, ω is the optical frequency and τ is the propagation delay.

Then, we compute the scattering matrix of every PUC that makes up the mesh structure, employing their phase configurations. Next, we proceed with the inductive method employing the scattering matrix of n-order mesh using the matrix S(n-1) of the immediately previous mesh and S_{PUC}(n) of the new block to be connected. The calculation process depends on how the new block is connected to the older structure - the number of new ports added to the mesh by performing a new join- and whether a cell is being closed. As a result, there are four possible interconnection scenarios between the new additional lattice and the previous lower-order mesh. As shown in Figure 3.2, these scenarios are classified according to the number of ports that are being used to make the connection. Note that although the same scenarios are described in [42], the resulting equations will be different due to the change on the minimum block architecture employed.

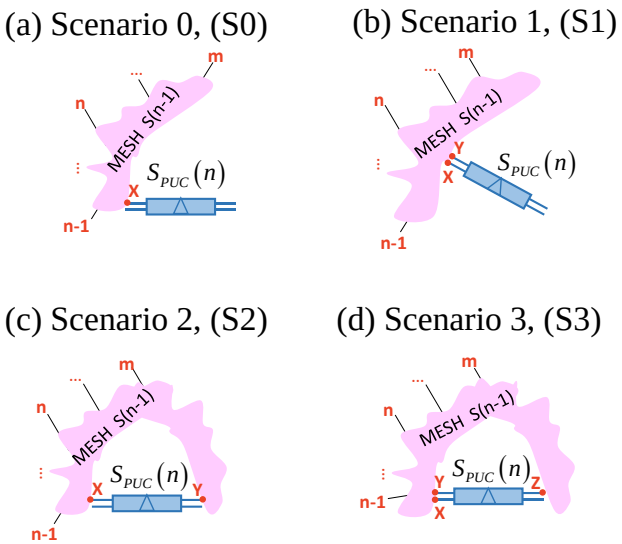

Figure 3.2. Description of the inductive method for obtaining the scattering matrix of a hexagonal 2D waveguide mesh composed of n PUCs by adding a unit S_{PUC}(n) to a hexagonal 2D waveguide mesh composed of n-1 PUCs. (a) Interconnection scenario 0. (b) Interconnection scenario 1. (c) Interconnection scenario 2. (d) Interconnection scenario 3.

***Scenario 0 (S0)*:** This scenario is the easiest case that we can use to enlarge the mesh. As can be seen in Figure 3.3. (a1), it represents the union of the new lattice with the

structure of order (n-1) through a single port, X. Considering that port number 1 of the PUC is used as a connection node X with the previous mesh or structure. Therefore, the number of ports of the resultant structure is increased by two, thus increasing the size of the scattering matrix of the new mesh. The signal flow diagram shown in Figure 3.3. (a2), defines the interconnection possibilities between the n-1 order mesh and the new PUC added through the interface node X. Using the diagram, a system of Eqs. (3.2) is defined, considering all the possible path contributions between the free ports of the older structure. Thus, the coefficients of the scattering matrix that models the mesh are recalculated. The resulting matrix, shown in Figure 3.3. (a3) can be divided into four submatrices. The first submatrix (Submatrix 1, SM1) defines the coefficients related to the connection between the input-output ports of the n-1 order structure, ergo, it excludes the input-output paths that involve the additional ports that have been created after the union of the new lattice. This means that the SM1 coefficients can be inherited directly from the n-1 matrix we already knew, so we do not need to recalculate them. Afterward, the second case (Submatrix 2, SM2) relates the interconnection creates between the input ports from the older mesh (n-1) and the output ports of the new PUC ($S_{PUC}(n)$). Then, the third (Submatrix 3, SM3) models the paths between input/output ports of the joined lattice. Finally, the last possibility (Submatrix 4, SM4) describes the inputs of the new PUC to the output ports of mesh n-1.

Submatrix 1 coefficients: $$S^{N}_{m,n} = X^{'} = S^{N-1}_{m,n}$$

Submatrix 2 coefficients: $$S^{N}_{\{n\ldots n+2\},n} = TS$$

Submatrix 3 coefficients: $$S^{N}_{\{n\ldots n+2\},\{n\ldots n+2\}} = Th_{xx}G + Z$$

Submatrix 4 coefficients: $$S^{N}_{n,\{n\ldots n+2\}} = GU$$

(3.2)

***Scenario 1 (S1)*:** As we can notice in Figure 3.2. (b), the union nodes between the structures are two, X and Y. Ports 0 and 1 on the same side of the PUC are used to perform the join. Consequently, the connection the resulting arrangement do not increase the number of free ports that it has, as can be observed Figure 3.3. (b1). Then, Figure 3.3. (b2). and (b3) illustrates the graph and the resulting scattering matrix obtained, after solving the system of equations, following the same methodology that has been explained in the case of S0. As can be seen in Eqs. (3.3), the resulting equations are more complex than Eqs. (3.2), since two interface nodes (X and Y) are required.

SM1: $$S^{N}_{m,n} = X = S^{N-1}_{m,n}$$

SM2: $$S^{N}_{\{n-1\ldots n\},n} = OE^{'} + TS$$

SM3: $$S^{N}_{\{n-1\ldots n\},\{n-1\ldots n\}} = \mathrm{OP}(h_{yy} + \mathrm{GN}) + \mathrm{T}(\mathrm{G}h_{xx} + \mathrm{MP}) + Z$$

SM4: $$S^{N}_{n,\{n-1\ldots n\}} = \mathrm{F}^{'}\mathrm{P} - \mathrm{UG}$$

(3.3)

***Scenario 2 (S2)*:** This joint does not increase the number of free ports either. Again, two nodes, X and Y, form the union but these are located one on each side of the PUC (see Figure 3.3. (c1)). Should be noted that in this scenario, the number of closed cavities/feedback loops increase by one. In this case, can appear a recirculation of light between the interface nodes and the newly added lattice as shown, by connections V and W, in the signal flow graph (observe Figure 3.3. (c2)).

Therefore, using the diagram, we can model the Eqs. (3.4) of each submatrix in this scenario. Formerly, we can observe in the definition of these equations a geometric sum of contributions due to the possibility of recirculation inside the mesh. In addition, in this case, it should be noted that the SM1 coefficients cannot be inherited from the n-1 order scattering matrix, as occurs in scenarios 0 and 1. Hence, they must be recalculated following the aforementioned system of equations.

Finally, by solving the system of Eqs. (3.4), we can provide the matrix coefficients that characterize the new structure (see Figure 3.3. (c3)).

SM1:
$$S^{N}_{m,n} = \left[\frac{-(B^{'}E^{'}V + DSW + B^{'}SVWh_{yy} - B^{'}E^{'}MVW - DNSVW + DE^{'}VWh_{xx})}{(MW + NV - MNVW + VWh_{xx}h_{yy} - 1)} \right] + X$$

SM2:
$$S^{N}_{\{n-1\ldots n\},n} = \frac{(\mathrm{O(E^{'}(MW - 1) - SWh_{yy}) + T(S(NV - 1) - E^{'}Vh_{xx}))}}{(\mathrm{MW + NV - MNVW + VWh_{xx}h_{yy} - 1})} \tag{3.4}$$

SM3:
$$S^{N}_{\{n-1\ldots n\},\{n-1\ldots n\}} = \left[\frac{\mathrm{-(O(Ph_{yy} + G(N - MNW + Wh_{xx}h_{yy})) + T(Gh_{xx} + P(M - MNV + Vh_{xx}h_{yy})))}}{(\mathrm{MW + NV - MNVW + VWh_{xx}h_{yy} - 1})} \right] + Z$$

SM4:
$$S^{N}_{n,\{n-1\ldots n\}} = \frac{(\mathrm{F^{'}(P(NV - 1) - GWh_{xx}) + U(G(MW - 1) - PVh_{yy}))}}{(\mathrm{MW + NV - MNVW + VWh_{xx}h_{yy} - 1})}$$

***Scenario 3 (S3)*:** This scenario is the most complex because not only the number of free ports in the mesh is not increased, but the resulting structure also has two fewer free ports. As we can observe in Figure 3.3. (d1), three ports, X, Y, and Z, are used for the addition. For this reason, the interconnection diagram (Figure 3.3. (d2)) involves three interfacing nodes (X, Y, and Z). Highlighting, again, the possible recirculation between the nodes X and Z, and Y and Z of the interface and the new PUC joined, modelled by the connections C, E, K, and L of Figure 3.3. (d2).

The procedure to obtain the coefficients of the submatrices is similar to the three previous cases. The equations have greater complexity and density, so they will not be defined here. Although, we can be expressed the equation system using the signal flow graph (see Figure 3.3. (d2).) and apply the same methodology as the other scenarios. Then, the resulting scattering matrix sections of the scenario 3 is shown in Figure 3.3. (d3).

It is important to mention that, in all scenarios, the unions will always be made through the last port(s) of the mesh S(n-1). The detailed pseudocode to facilitate programming are provided in Appendix A. The programming and simulation have been carried out in Python programming language. The performance of this algorithm can be summarized as a methodology to compute the full scattering matrix that is not computationally time-dependent on the system configuration. Its application and benchmark are presented the next section.

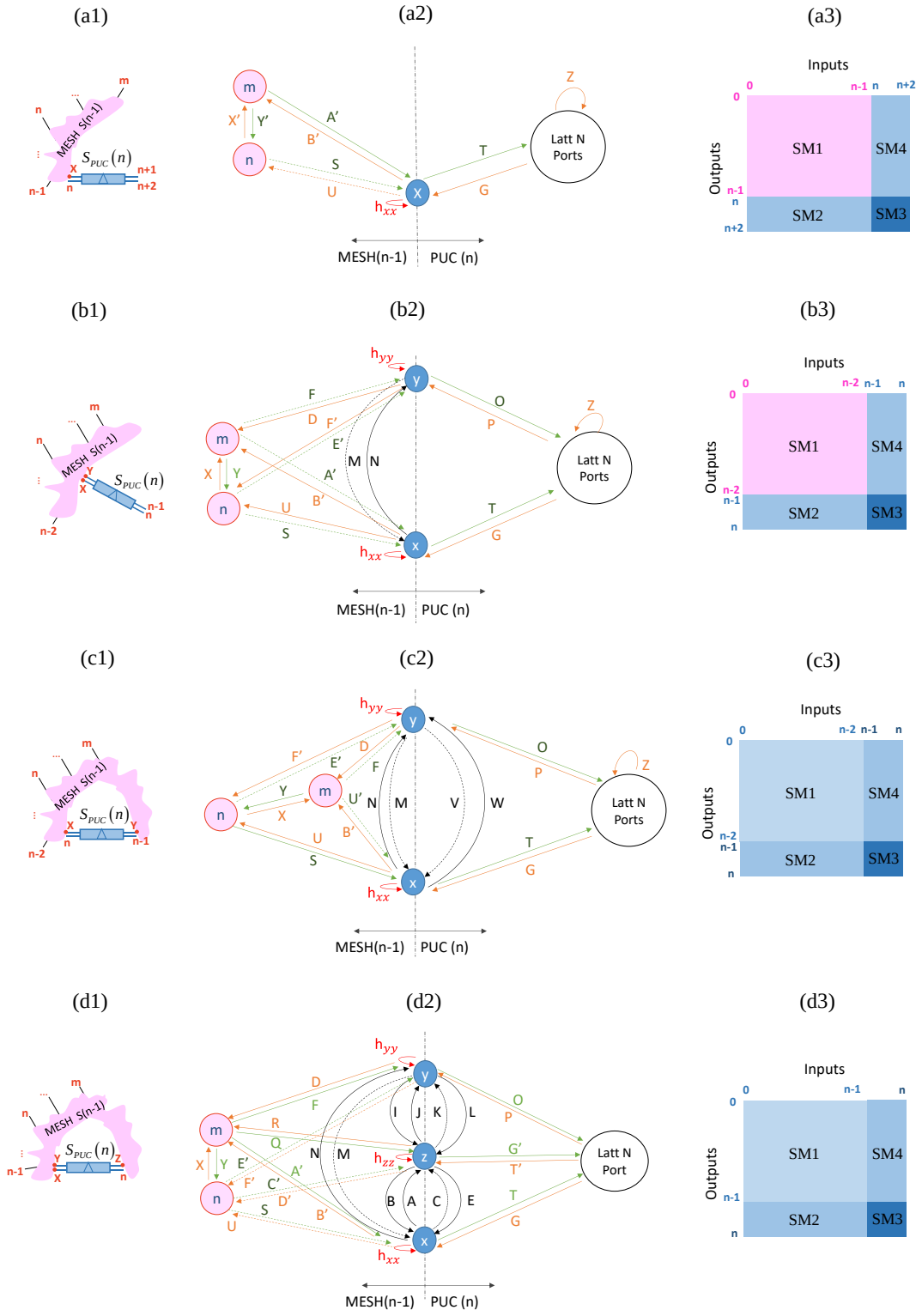

Figure 3.3. (a) Scenario 0, (b) Scenario 1, (c) Scenario 2 and (d) Scenario 3 and (1) Connection scheme of the additional lattice with mesh n-1 of each scenario, (2) Interconnection graph diagram with the labelled contributions of each scenario (3) Resulting scattering matrix sections of each scenario.

3.2.2. Method timing analysis

In this section, we present a scalability statistical analysis between the trilattice-based approach proposed in [42] and graph-based methodology [43] with the inductive single-cell method presented in this work for different mesh configurations.

The configuration examples are: a balanced Ring-Assisted MZI (RAMZI) filter, a Side-Coupled Integrated Spaced Sequence of Optical Resonators (SCISSOR) filter, 1x8 beamsplitter, an 8x8 unitary matrix, and all passive state case. For each case, we sweep over two parameters: the wavelength resolution (going through 3, 11, 101, and 1001 wavelength points for a span of 1 nm centered at 1550 nm) and the number of PUCs, which will determine the mesh size. For all examples (unless otherwise specified) we go through meshes of 34, 36, 45, 72, 81, 87, 134, 198, 397, 599, 799, and 1002 PUCs. The insertion loss of each PUC is initially set at 0.2dB.

Each circuit configuration involves the targeted circuit topologies and the configuration of the access waveguides to east and west ports. Once configured, we compute 10 times each simulation to enable the statistical analysis, employing two equally-equipped desktop computers: 4-core, and 3.60 GHz processors.

The first circuit is the balanced RAMZI filter, Figure 3.4 (a1) illustrates its synthesis in an 81-PUC mesh, using ports 15 and 33 as input/output. Hence, the lower arm of the RAMZI would pass through PUCs 33, 40, and 47 after being split in PUC 25 while the upper one would do so through PUCs 32, 39, and 46. The cavity of the structure is configured by PUCs 30, 31, 38, 44, and 45, all in bar state. The simplified schematic is illustrated in Figure 3.4 (b1).

Figure 3.4 (c1) contains the average elapsed time required for each simulation example. First, we can see that the inductive method, scales linearly with the number of points. As an example, the time of 1001 is 1000 times higher than the 3-point simulation at 1000 PUCs. Till, the graph-based approach timings overlap for different wavelength resolutions, indicating a better scalability with the number of points

However, we tested the handling of non-ideal components during the simulation. In such scenario, PUCs may present a phase response drift (resulting in deviated configurations) because of the combined effects of optical, thermal, and electrical crosstalk. More information about these effects and how to mitigate it can be found in [42], [45]. To do so, we modelled the coupling coefficients of each of the PUCs forming the RAMZI as truncated gaussian variables centered at their original (ideal) values and featuring a standard deviation (drift) of 0.02. Values lying below 0 (bar state) or above 1 (cross) are ‘mirrored’ by adding or subtracting respectively its absolute value to the original one. As illustrated in Figure 3.4. (d1), the graph-based approach significantly increases its computational time. In particular, focusing on the 600-PUC example, it is around 2.5 times slower and 2.5 times faster than the inductive method for 3 and 1001 points, respectively. In addition, it is 7 times slower than the graph approach with the perfect component case. Till, the computation time required for the inductive method is invariant to the non-idealities of the components.

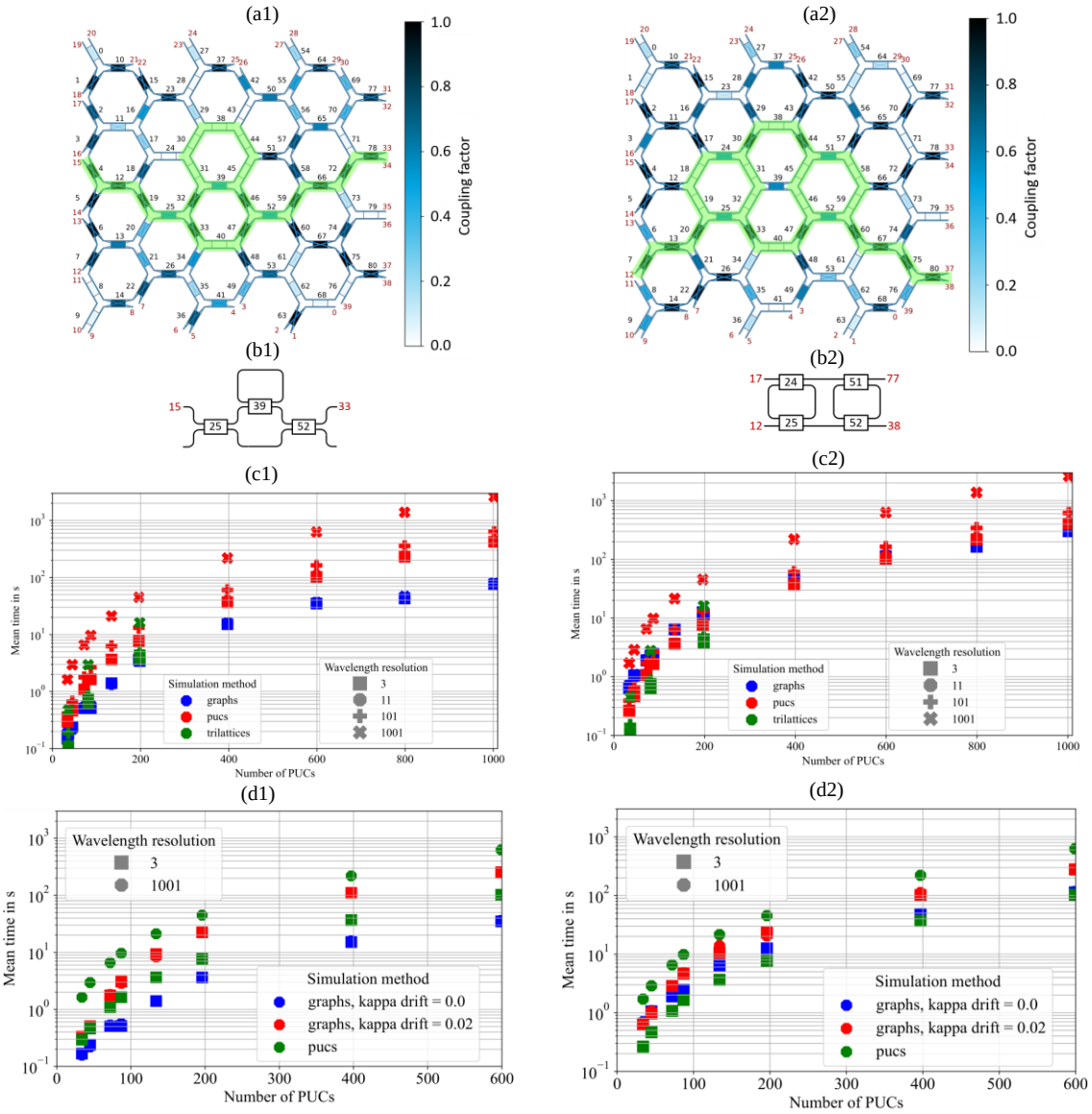

Figure 3.4. (a1) Synthesis of a balanced RAMZI filter in a simulated 81-PUC waveguide mesh using 15 and 33 as input/output ports, (b1) equivalent circuit synthetized, (c1) evolution of the mean elapsed time (in seconds) with the number of PUCs for the synthesis of this circuit for four different wavelength resolutions with ideal coupling coefficients and (d1) with coupling coefficients modelled as random variables featuring a drift with a standard deviation of 0.02. (a2) Representation of a SCISSOR in a simulated 81-PUC waveguide mesh using 15 and 33 as input/output ports, (b2) Schematic of equivalent circuit synthetized, (c2) Evolution of the mean elapsed time (in seconds) with the number of PUCs for the synthesis of this circuit for four different wavelength resolutions with ideal coupling coefficients and (d2) with coupling coefficients modelled as random variables featuring a with a standard deviation of 0.02.

Next, we present the simulation results for the optical SCISSOR defined in Figure 3.4 (a2) between ports 12 and 38. To configure this circuit, we set PUCs 2, 7, 11, 13, 17, 20, 30, 33, 44, 47, 57, 60, 65, 67, 70, 75 and 80 to cross state and PUCs 18, 19, 31, 32, 38, 40, 45, 46, 58 and 59 to bar state. At the same time, PUCs 24, 25, 51, and 52 are set in a Tunable Coupler State to allow light to travel back and forth and be coupled throughout the structure. Figure 3.4 (b2) illustrates the simplified scheme.

As with the previous example, Figure 3.4. (c2) illustrates the elapsed time for the different simulation approaches. In this case, the graph-based approach, applied to a second order Infinite Impulse Response (IIR), demands more computational time as the number of power contributions arriving at the output port reaches up to 31.
Consequently, the elapsed computation time of graph-based approach is larger than that of a trilattice-based one for smaller size meshes and lies much closer to that of a single-cell inductive method for larger size meshes and small wavelength resolutions.
Repeating the test for imperfect components with the same methodology as in the previous example, we can observe in Figure 3.4. (d2) that graph-based approach still outperforms inductive single-PUC approach for large wavelength points, offering better scalability. However, for a smaller number of points (3), the inductive method provides a faster computational time. For example, for 600-PUC meshes, the computation times are 275.85 and 103.8 seconds for the graph and inductive approach, respectively. Hence, growing to larger order IIR structures might prevent us from using this strategy and opt for inductive-based approaches.

Moving to a different configuration example, Figure 3.5. (a1) presents a 1x8 beam-splitter, outlined in Figure 3.5 (b1). Such circuit takes port 15 as input and 0, 5, 7, 22, 29, 31, 32, and 33 as outputs. Here, light is split in PUCs 12, 18, 19, 25, 33, 40, and 77, all in Tunable Coupler state.
As covered in Figure 3.5 (c1), for the mesh-sizes considered, the graph-based approach performs faster than the inductive one for lower number of spectral points. This no longer occurs, however, if we introduce non-ideal components such as in Figure 3.5. (d1). In this case, graph-based approach's computation time increases dramatically as a result of the appearance and spreading of multiple paths during the execution of this method that may not be discarded up to final stages of its execution. As an example, for the 600-PUC mesh and larger spectral vectors (1001 wavelength points), the graph-based approach requires around 1.6x more time than the inductive method, while the gap becomes of 10x for lower (3) number of points. This particular application demands higher resolution and number of points when validating the channel ripple conditions. Otherwise, the expected spectral behaviour is inherently flat. The presence of non-ideal configurations and the increment of optical outputs favor the selection inductive method approach.

The next example focuses on multiple input – multiple output applications. In particular, we configure the 8x8 optical matrix appearing in Figure 3.5. (a2) and represented in Figure 3.5. (b2). Here, we performed simulations for three mesh sizes of 198, 397, and 599 PUCs since it was not possible to allocate this structure in smaller-size meshes. In the figure, mesh ports 33, 34, 35, 36, 37, 38, 39, and 40 work as input ports and mesh ports 1, 2, 3, 4, 5, 6, 7 and 8 operate as output ports. Setting of an arbitrary linear matrix requires the configuration of the Tunable Couplers, driving PUCs 10, 11, 12, 13, 28, 29, 30, 43, 44, 45, 46, 61, 62, 63, 76, 77, 78, 79, 94, 95, 96, 109, 110, 111 and 112. In addition, we configure the access waveguides following a similar approach as in the beamsplitter case. The PUCs interconnecting the TC-configured cells are set into Cross-State. The configuration of the TCs are selected employing random distributions to maintain the arbitrariness of the configuration process.

In this case, the graph-based approach is run iteratively for each input/output pair to complete the triangular matrix of the resulting scattering matrix. The results, in Figure 3.5. (c2), illustrate how the elapsed time of the graph approach is around 2 and 3 orders of magnitude larger than that of the inductive method for the larger and shorter wavelength vectors, respectively.

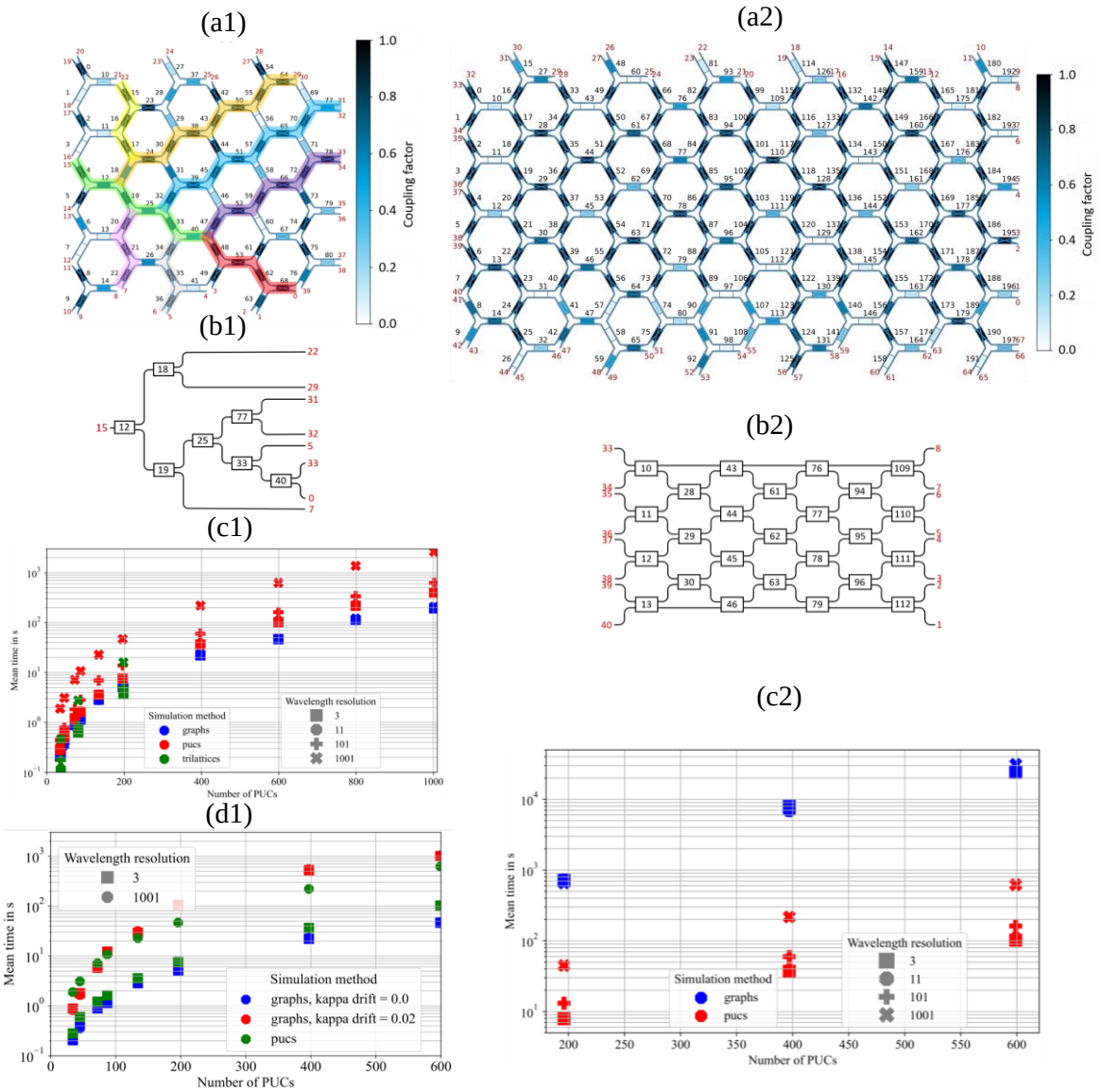

Figure 3.5. (a1) Representation of a 1x8 beam splitter in a simulated 81-PUC waveguide mesh using port 15 as input port and 0, 5, 7, 22, 29, 31, 32, and 33 as output ports, (b1) Schematic of equivalent circuit synthetized, (c1) Evolution of the mean elapsed time (in seconds) with the number of PUCs for the synthesis of these circuits four different wavelength resolutions with ideal coupling coefficients and (d1) with coupling coefficients modelled as random variables featuring a standard deviation of 0.02. (a2) Representation of an 8x8 identity matrix in a simulated 198-PUC waveguide mesh using ports 33, 34, 35, 36, 37, 38, 39, and 40 as input ports and 1, 2, 3, 4, 5, 6, 7 and 8 as output ports, (b2) Schematic of the equivalent circuit synthesized and (c2) Evolution of the mean elapsed time (in seconds) with the number of PUCs for the synthesis of these circuits four different wavelength resolutions.

Afterward, we conclude our set of experiments by simulating the full response (i.e., using all mesh ports as inputs and outputs) of the waveguide mesh under a random configuration. This represents a scenario with arbitrary complex configurations present on certain applications or uncalibrated circuits. An interesting application of this feature deals with neuromorphic computing engines [39], [46]. The results of the analysis are presented in Figure 3.6. For this application, motivated by the exigent computational times of the graph-based approach, we selected mesh sizes up to the 196-PUC waveguide mesh only.

As in the previous case, the graph-based approach runs iteratively for each input/output pair to complete the triangular matrix of the targeted scattering matrix. As for the beamsplitter and the 8x8 circuits, the randomness of PUC transmission states favors the existence of many candidate paths. This effect is exacerbated by the presence of internal feedback loops. Precisely, the performance of the graph-based approach is around 3 and 4 order of magnitude slower than the inductive method approach, for the longest and shortest wavelength vector, respectively.

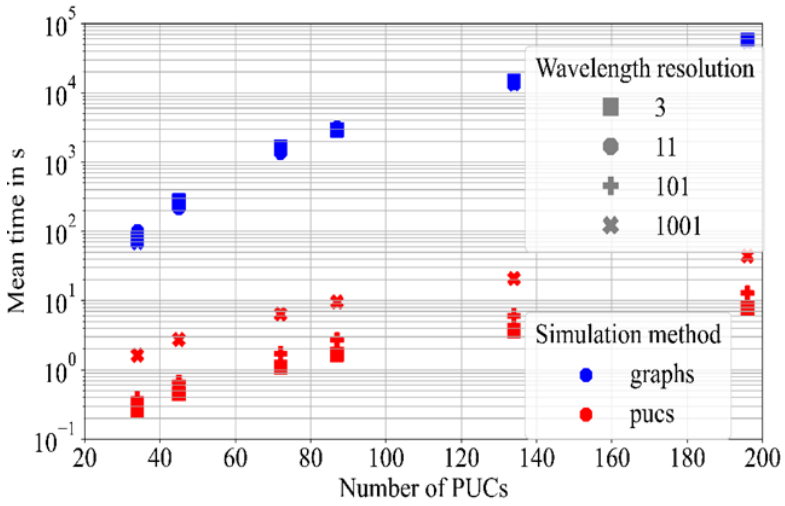

Figure 3.6. Evolution of the mean elapsed time (in seconds) with the number of PUCs for the obtention of the response of all ports in a passive waveguide mesh for four different wavelength resolutions.

Finally, to demonstrate the flexibility of the photonic hardware and the capabilities of the proposed simulation method we consider an optical switch with arbitrary switching schemes mixing (single port, multiport, and wavelength selection). The 196-PUC waveguide mesh under study is presented in Figure 3.7. We define two different configurations on it, hereinafter referred to as Config. A and Config. B and represented in Figure 3.7(a) and (b) respectively. Config. A includes the synthesis of two optical paths connecting ports 10-63 and 41-55, a 1x4 beamsplitter using port 48 as input and ports 30, 31, 33, and 34 as outputs, and a 2x1 combiner with input ports 13 and 14, port 20 acting as output and using port 47 to drain optical leakage. At the same time, Config. B contains a 1x6 beamsplitter (input port: 10, output ports: 13, 41, 47, 48, 55, and 63), two optical paths connecting ports 20 and 33 and 31 and 34, and an Optical Ring Resonator (ORR) between ports 14 and 30.

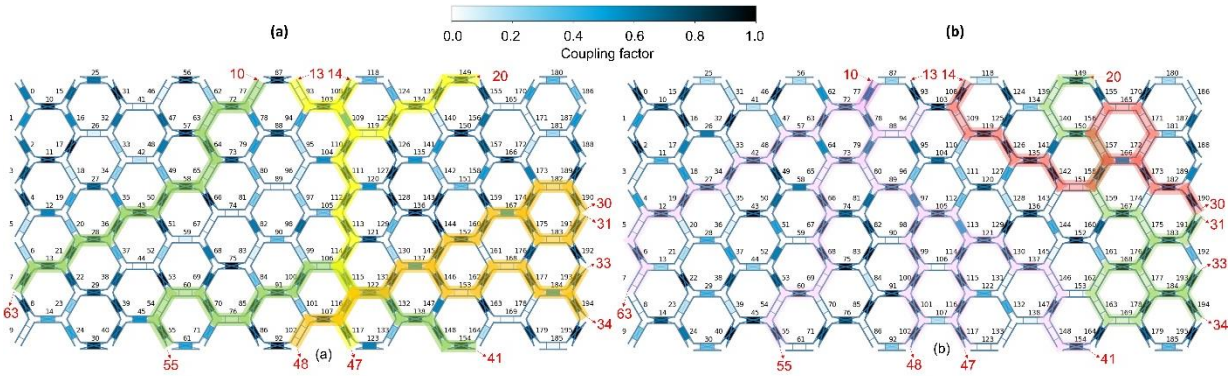

Figure 3.7. Waveguide mesh arrangement of 196 programmable unit cells configured as an arbitrary optical switch and processor including point-to-point (in green), point to multipoint (beamsplitters, in orange and pink), signal combiners (in yellow), and wavelength-sensitive filters (in red): (a) Configuration A, (b) Configuration B.

To exploit the analytical model developed, we determine three different use cases for the remainder of this work for both switch configurations. Case 1 represents a scenario using ideal components, in which the coupling factors of all PUCs constituting the synthesized circuits in both switches have no phase drift and therefore feature ideal Cross/Bar/Tunable Coupler States. For cases 2 and 3, we tested the handling of non-ideal components (i.e., presenting a phase response drift resulting in deviated configurations). To do so, we modelled the coupling coefficients as truncated gaussian variables centered at their original (ideal) values and featuring a standard deviation (drift) of a 2%. Values lying below 0 (Bar State) or above 1 (Cross State) are 'mirrored' by adding or subtracting respectively its absolute value from the original one. The difference between both use cases resides in the state of the remaining passive PUCs of the waveguide mesh, with random and all-cross coupling values for test cases 2 and 3 respectively. Once configured, we compute 50 times each simulation to enable a statistical analysis, employing two equally-equipped desktop computers including 4-core and 3.60 GHz processors.

As a benchmarking example, Figure 3.8. (a) illustrates the resulting spectral traces associated to Configuration A for the non-ideal component examples. In particular, we show the combination of ports when an input signal is injected through port 48. One can identify the optical targeted output ports of the 1x4 beamsplitter, the optical crosstalk at ports sharing common PUCs (< 20 dB), and the remaining ports (< 30 dB). Next, Figure 3.8. (b) shows the spectral traces associated to Configuration B for the non-ideal component examples. In particular, we show the combination of ports when an input signal is injected through port 14. We can identify the optical targeted output ports of the filtered channel, the optical crosstalk at ports sharing common PUCs (< 20 dB), and the remaining ports (< 30 dB). In addition, Table 3.1 includes the elapsed time (in seconds) required for each application scenario and standard deviations (between parentheses) of both switch configurations using graph-based and inductive methods. As can you observe in the Table, the inductive method is quite robust to possible non-ideal components. Since, the standard deviation between cases remains quite low and stable. In addition, once again we verify that it is independent of the state of the PUCs that do not are part of the path. However, graph method works slightly better than inductive in Case 1, with ideal components, but it is pretty sensitive to possible non-ideal components. Seeing that the elapsed time in Case 2 and 3 increases substantially compared to Case 1. Moreover, it behaves much faster when the remaining passive PUCs of the waveguide mesh are in Cross State, thus deriving the leakage that has occurred due to non-idealities.

To summarize the performance of the proposed methods we can conclude the following: First, the inductive method requires the computation of the whole scattering matrix of the structure, even if a subset of matrix elements is required. The computation time of this method is independent from the configuration of the PUCs. In addition, it scales linearly with the number of spectral points. In contrast, the graph-based is by nature port-pair oriented. However, it can be employed sequentially to extract complete scattering matrices. Multicore electronic processors could be employed to improve the efficiency of this task with parallel processing. The performance of the graph-based approach is significantly invariant with the number of wavelength points and depends on the system configuration. For this reason, the selection of the simulation method is application dependent. For applications with many closed optical paths and lower number of feedback and feedforward loops, the graph-based methodology performs faster simulations. This is also true when only a small subset of elements is required from the scattering matrix. In contrast, the use of the inductive approach provides faster simulation times for arbitrary complex circuits requiring large number of optical ports. Moreover, both methods provide additional flexibility when compared to the existing lattice-based inductive simulation method [42], allowing the design and its application to arbitrary circuit topologies.
In addition, all methods presented here can be applied to any highly coupled circuit topology (square, hexagonal, triangular, feedforward, etc.) and already support dynamic crosstalk

simulation. Consequently, both of them unfold as effective and versatile tools for the study of emerging multipurpose programmable photonic processors.

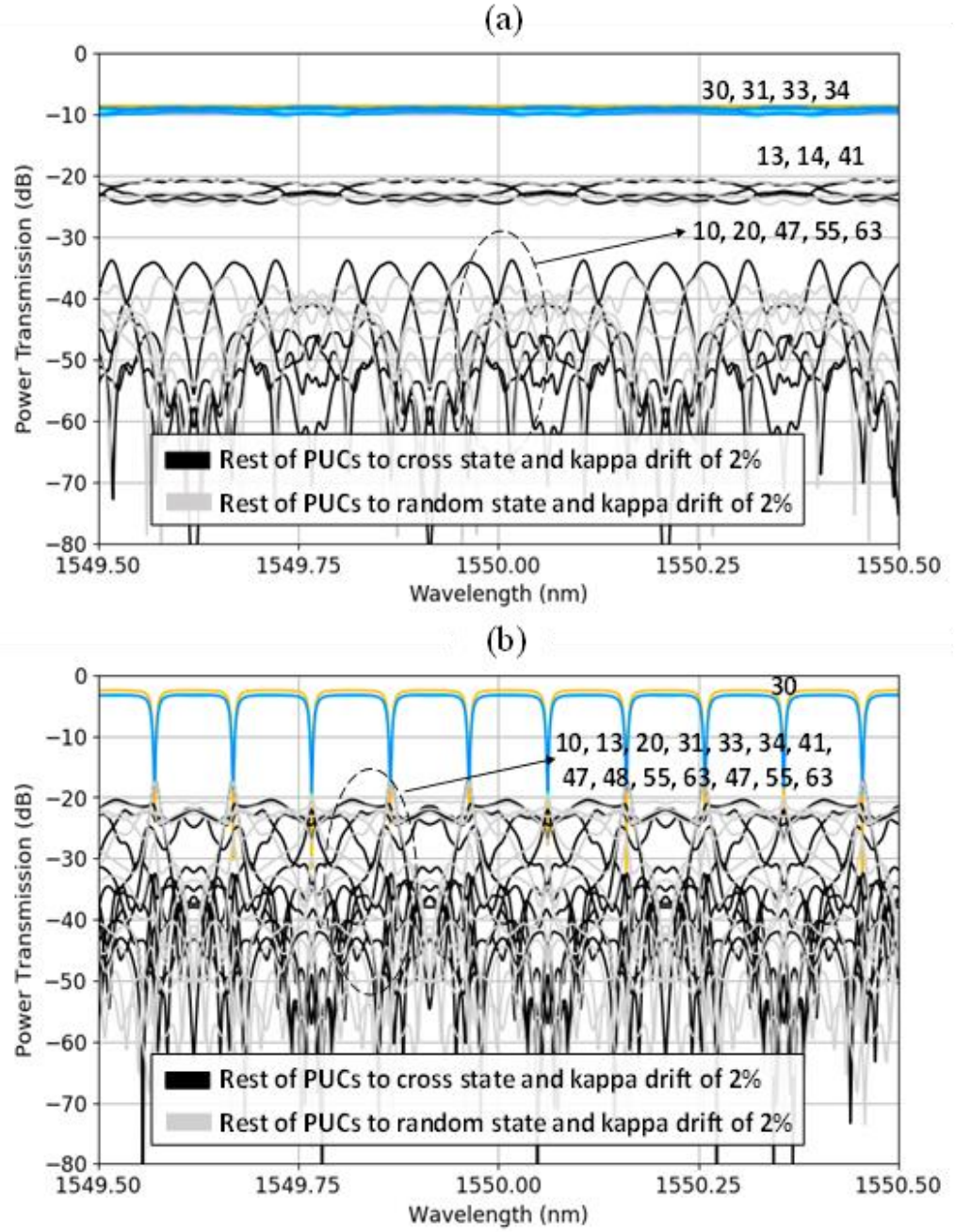

Figure 3.8. Spectral responses from every switch port highlighted in Figure 3.7. (a) under Configuration A, entering through port 48, (b) under Configuration B, entering through port 14. The simulation considers non-ideal 2%-drift at every programmable unit cell. Orange-colored spectra are provided using components with ideal coupling coefficients (case 1), while cyan- and navy-blue ones correspond to imperfect components featuring phase drifts of 2% while setting the passive phases of the remaining PUCs to random and cross state, respectively.

Table 3.1. Summary of the mean elapsed times (in seconds) and standard deviations (between parentheses) after 50 repetitions of the synthesis of both switch configurations A and B using graph-based and inductive methods under the three scenarios described in the text.

		Wvl. resol.	Case 1	Case 2	Case 3
Graph-based	Config. A	101	9.28 (0.25)	413.90 (35.03)	205.81 (34.25)
		1001	9.71 (0.18)	437.60 (49.41)	269.02 (29.06)
	Config. B	101	29.30 (0.56)	381.17 (43.69)	209.04 (25.49)
		1001	29.58 (0.49)	397.90 (36.80)	187.07 (27.91)
Inductive	Config. A	101	12.04 (0.21)	12.16 (0.16)	12.05 (0.13)
		1001	42.25 (0.41)	42.45 (0.39)	42.87 (0.26)
	Config. B	101	13.51 (0.31)	13.69 (0.18)	13.99 (0.67)
		1001	45.21 (0.80)	45.48 (0.37)	43.27 (0.62)

3.3. Experimental versus simulated measurements

In this section, we compare the responses obtained from the simulation tool, inductive method based presented above, with experimental results in hardware for different reconfigurable optical filters. To do this, we will use the commercial Smartlight optical processor from IPronics Programmable Photonics S.L. shown in Figure 3.9.

In Figure 3.9. (a), we see the Smartlight processor, which contains a laser 2nm range, with a central wavelength 1550 nm, a silicon photonics chip (C-band), Multichannel Electrical Monitoring unit Array (MEMA) with photodetectors at each optical output port and an integrated driving unit with full operational control. Then, the optical processor system design is shown in Figure 3.9. (b). Moreover, in Figure 3.9. (c), we observe in detail the PIC used for the experiment fabricated by AMF foundry and packaged optically and electrically by Chip Integration Technology Center (CITC) packager. The chip is pre-calibrated and self-characterized by software before the experiments by means of an autocalibration method [45]; so that, through a Multichannel Electrical Driving Array (MEDA) and using the information obtained from each PUC calibration curves, several structures can be synthesized by varying the state of the PUCs.

The hexagonal photonic mesh included in the measured chip, with 72 tuning units and 40 input/output ports is shown in Figure 3.9. (d). Where each PUC, taking into account the access guides, the multi-mode interferometers (MMIs) and the length of the arms that form part of the MZI is has a Basic Unit Length (BUL) of 811.46 micrometres. Then, the control of the electrical signals through the driving units was carried out by software using Smartlight software from iPronics, Programmable Photonics S.L. Afterwards, we can change and control the coupling factor (K) and the cross phase (CP) of each PUC individually. In this way, it will be possible to program and measure different structures using the same photonic processor. These experimental Ks are calibrated to implement the closest configuration to the one performed in simulation. From now on, all values of

coupling factor and cross phase, for each example, are detailed in Appendix A.2. Furthermore, you will notice that they are not exactly the same, this small variation is due to the fact that there are random phase errors in the mesh, in hardware, that have not been taken into account in the model. Moreover, in this case, it has been experimentally characterized that the insertion losses per PUC are around 0.45-0.48dB. Lastly, unless otherwise specified, all the measured spectral responses in the following sections are normalized to losses. These losses include the input and output edge couplers, the propagation losses of the mesh access paths (waveguides, bends and path through the mesh crossing the monitoring unit array (MUA)) and the loss corresponding to one PUC, resulting in a figure of around 10.5dB.

(a) (b) (c)

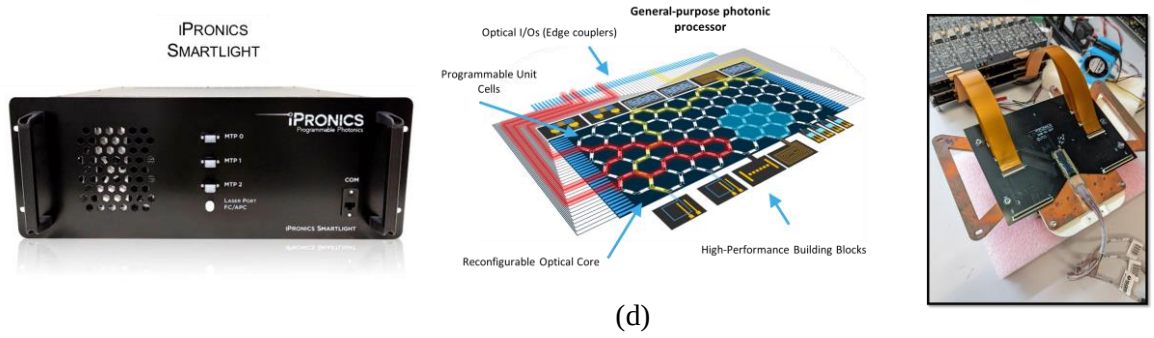

(d)

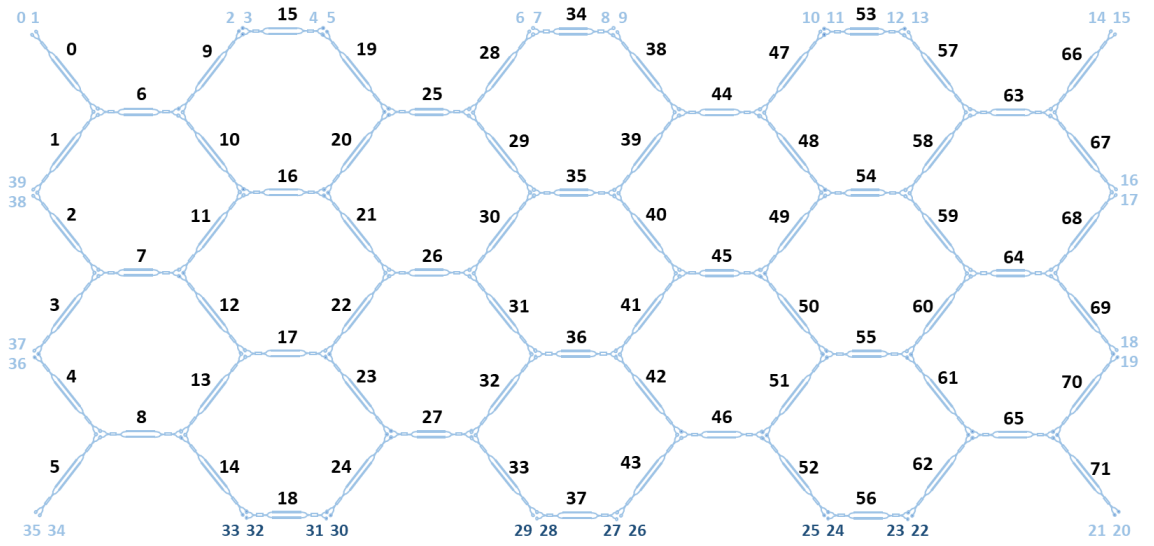

Figure 3.9. (a) Commercial Smartlight optical processor from IPronics Programmable Photonics S.L (b) Schematic of the processor system design (c) PIC and setup, contained in the reprogrammable optical processor, used to take the experimental measurements of the optical filters. (d) Hexagonal waveguide mesh arrangement of 72 PUCs.

3.3.1. Finite Impulse Response (FIR) filters

The first example will be a tuneable unbalanced Mach Zehnder Interferometers (UMZI), with a ΔL = 2 basic unit length between arms; see Figure 3.10. (a) and (b) to observe the synthesis in the mesh and its equivalent circuit, respectively. As can be seen, in the spectrum of the filter, Figure 3.10. (c), the Free spectral range (FSR), which is defined as two successive transmitted optical intensity maxima of an interferometer of the transfer function, depends on the length of the path unbalance. In this case, correspond to 0.35nm

(43.7GHz) for the 2-BUL UMZI. In addition, we are able to get a UMZI filter with an Extinction Ratio (ER) of 32dB. Also, can be seen in the comparison of spectra, Figure 3.10. (c), between the measured modulus transfer function versus simulated response that the developed tool works quite well, making a fairly accurate prediction of the response of the filter to be synthesized.

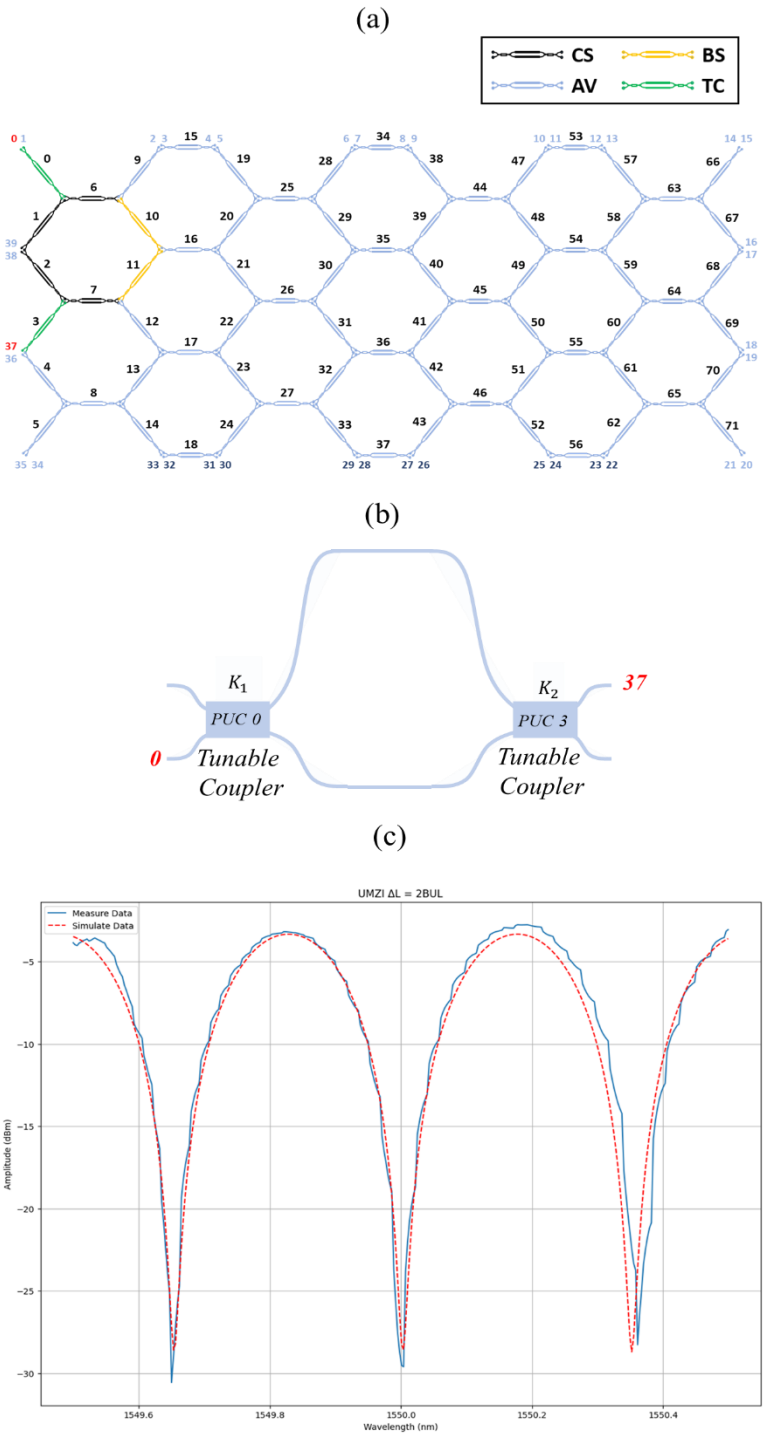

Figure 3.10. (a) Waveguide mesh arrangement of 72 programmable unit cells configured as an Unbalanced Mach-Zehnder Interferometer (UMZI) filter of ΔL = 2 BUL. CS, Cross State; BS, Bar State; AV, available; TC, Tuneable Coupler (b) UMZI equivalent circuit (c) Measured transfer function versus simulated response using the developed tool.

Next, we can tune the spectral response obtained with the previous UMZI. This is achieved by maintaining the state of the PUCs and varying the cross phase of a PUC from one of Mach Zehnder's arms, for example, PUC 10. As can we see, in Figure 3.11, the experimental measurement versus the simulated ones fits quite well.

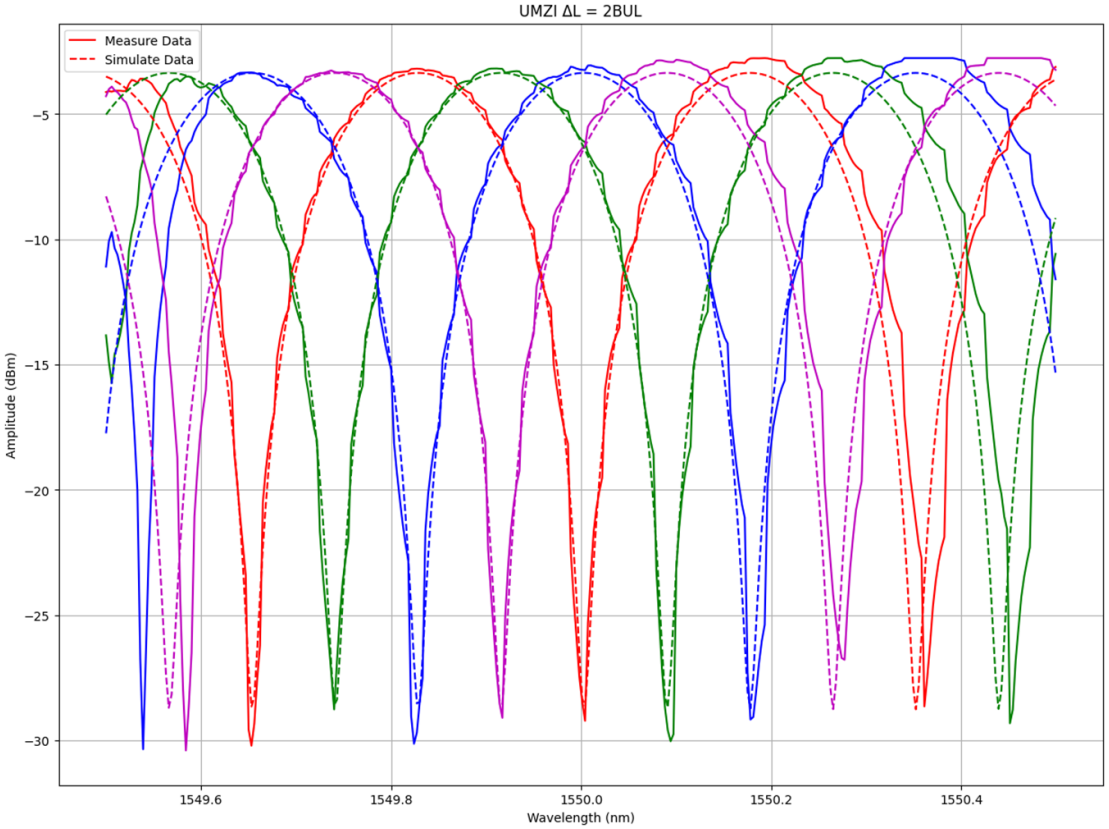

Figure 3.11. Signal tuning by shifting the cross phase of the PUC 10, experimental measurement versus simulated UMZI response.

After a UMZI finite impulse response filters, we also implemented more complex lattice filters by serially cascading UMZI units. Specifically, we synthesize an UMZI ΔL = 2 BUL lattice filter of third order, as can be seen in Figure 3.12. (a) and (b). Also, for all these filters, the tunability for fixed coupling factors and different active cross phase shifter tuning it could be simulated and measured following the same method shown in the previous example. In this case, as shown in Figure 3.12. (c), we can achieve a FSR of 0.36nm (44.95GHz) and an ER of 23dB. Again, we can affirm that the simulation tool used to observe the behaviour of the synthesized filter fits reality quite well with the experimental measure.

3.3.2. Infinite Impulse Response (IIR) filters

Now, we focused on infinite impulse response filters. By suitably tuning the PUCs in the waveguide mesh, and due to its large size, it is possible to synthesize optical ring resonators with many cavity lengths. As a proof of concept, we programmed single cavity optical ring resonators with cavity length given by 6, Figure 3.13. (a) and (b). As expected, the FSR in the transfer function changes according to ORR cavity length. In this experiment, we achieve a FSR of 0.12nm (15GHz) for a 6-BUL cavity length, observe Figure 3.13. (c). Moreover, we chose coupling factors for a maximum extinction ratio around 14dB in the transmission case.

After that, we also demonstrated tunability capability of these filters by fixing the coupling factors and changing the cross-phases. So, we tune the spectral response as can see in Figure 3.14. The wavelength shifts of 0.0582nm per π-rad cross phase were measured for this optical add-drop multiplexer (OADM) filter of 6-BUL.

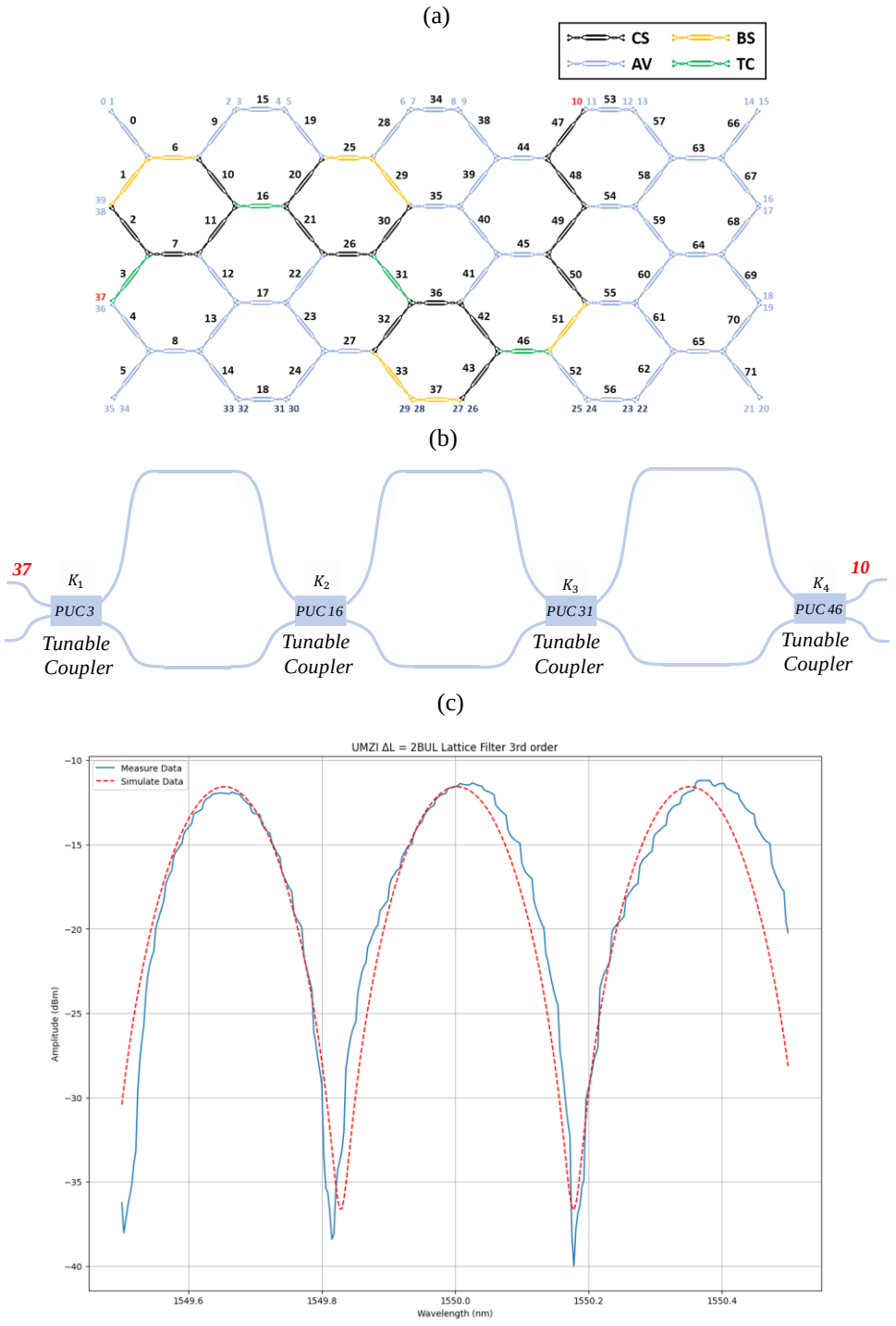

Figure 3.12. (a) Waveguide mesh arrangement of 72 programmable unit cells configured as an UMZI ΔL = 2 BUL lattice filter of third order. CS, cross state; BS, bar state; AV, available; TC, tuneable coupler (b) UMZI ΔL = 2 BUL lattice filter of third order equivalent circuit (c) Measured transfer function versus simulated response using the developed tool.

(a)

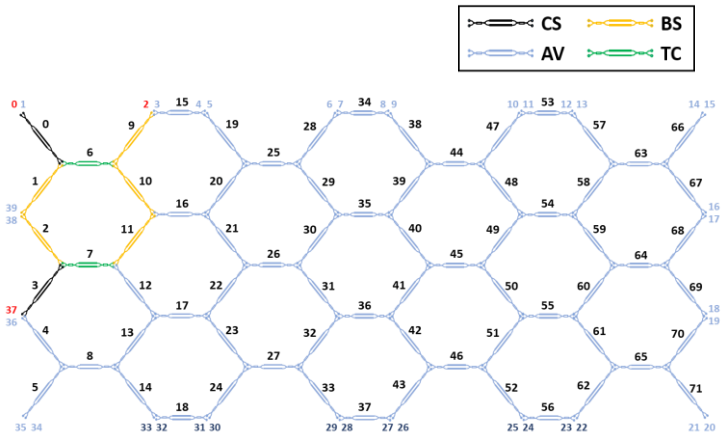

(b)

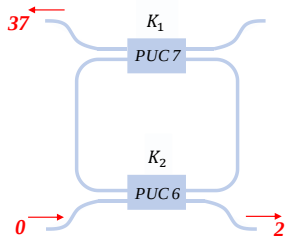

(c)

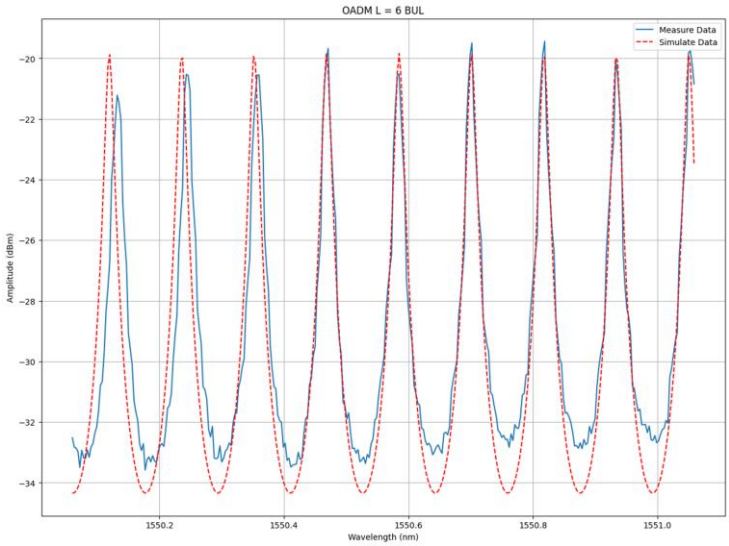

Figure 3.13. (a) Waveguide mesh arrangement of 72 programmable unit cells configured as an OADM filter of L = 6 BUL. CS, cross state; BS, bar state; AV, available; TC, tuneable coupler (b) OADM equivalent circuit (c) Measured transfer function versus simulated response using the developed tool.

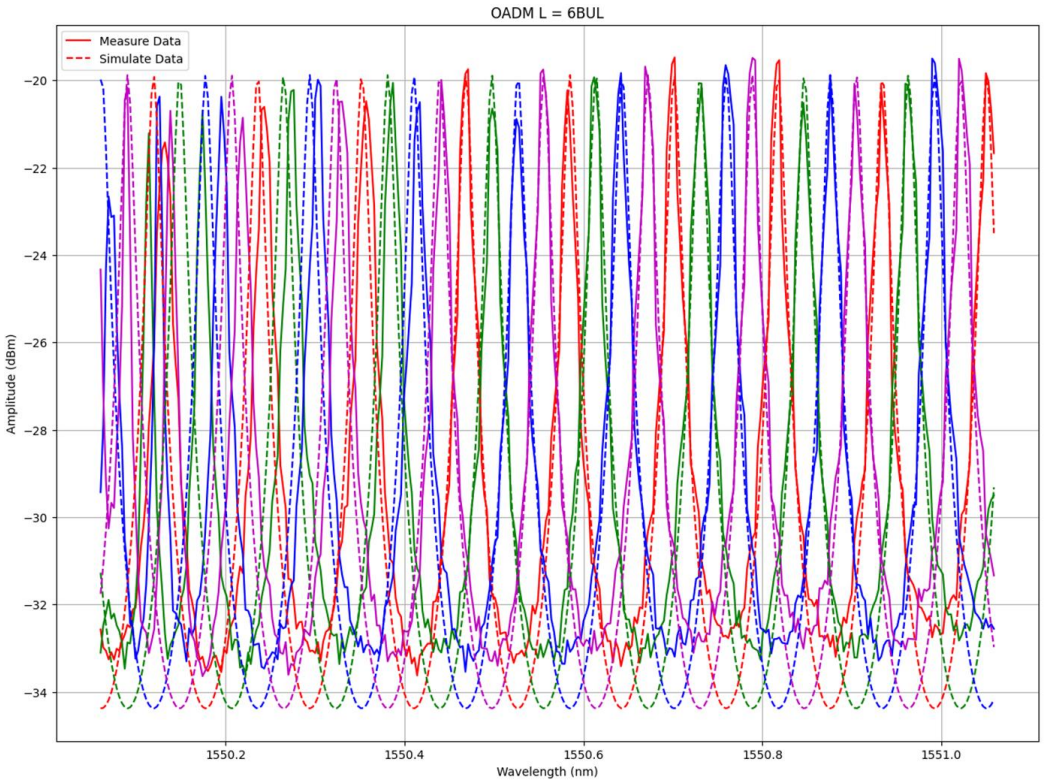

Figure 3.14. OADM response tuning by shifting the cross phase of the PUC 2, experimental measurement versus simulated response.

3.3.3. Complex filters

Then, we can build more complex multi-cavity signal processing structures as Coupled Resonator Optical Waveguide filters (CROW), SCISSORS, and Ring-Loaded MZIs using the ORR basic building blocks in the waveguide mesh and activating more PUCs to provide additional propagation paths.

Subsequently, we fix an OADM L = 6BUL second order coupled resonator optical waveguide filter and an OADM L = 6BUL third order SCISSOR, Figure 3.15 (a)-(b) and Figure 3.16 (a)-(b), respectively.

In Figure 3.15. (c), we can see the reflection spectrum of the CROW filter, which has a FSR of 0.12nm (15GHz) and allows an ER around 12dB. Whereas that in Figure 3.16. (c), it is observed that the SCISSOR FSR measured is 0.11nm (13.75GHz) and the ER is around 16dB. Hence, both parameters experimentally analyzed, match with the simulation.

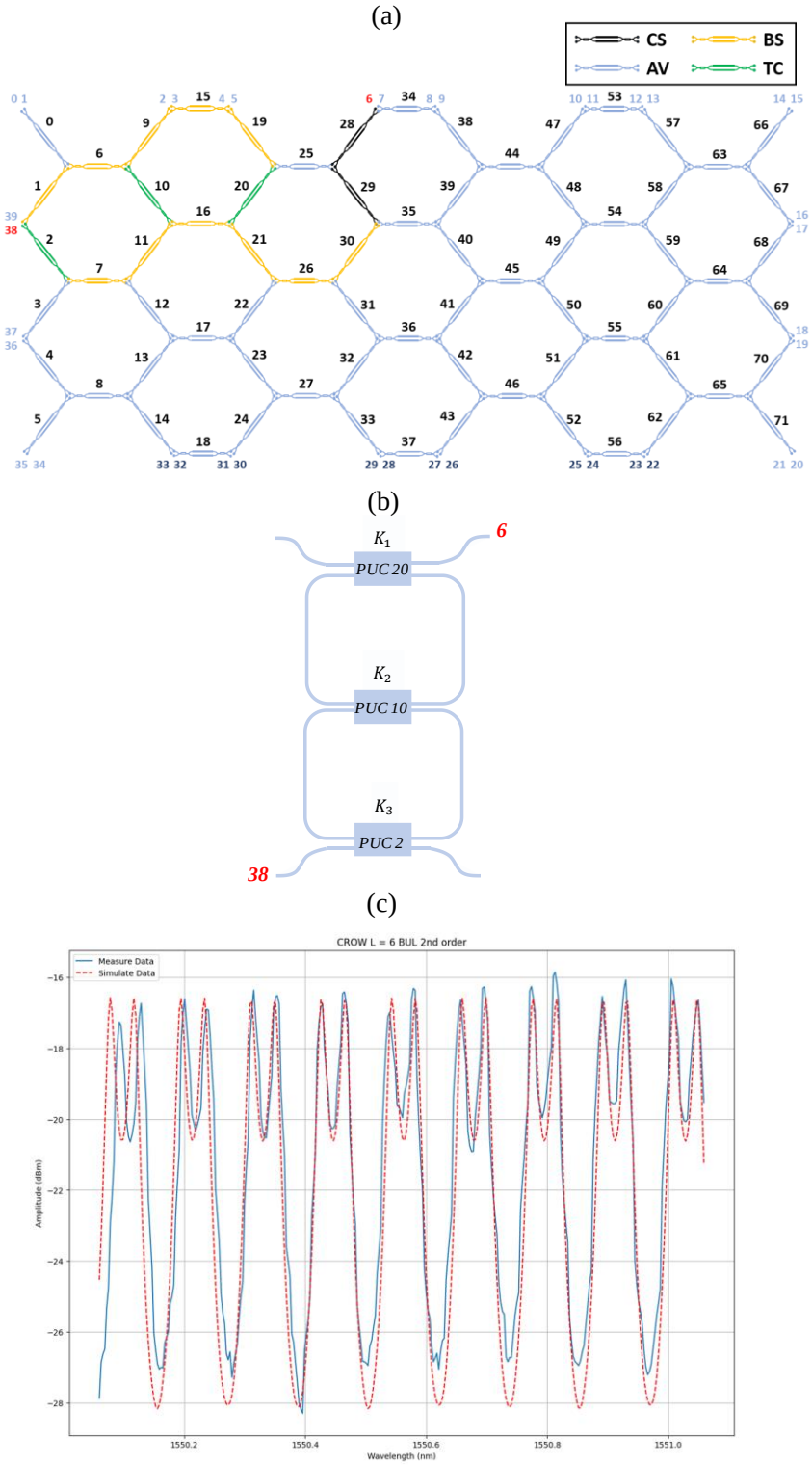

Figure 3.15. (a) Waveguide mesh arrangement of 72 programmable unit cells configured as an OADM filter of L = 6 BUL CROW 2nd order filter. CS, cross state; BS, bar state; AV, available; TC, tuneable coupler (b) Equivalent circuit (c) Measured transfer function versus simulated response using the developed tool.

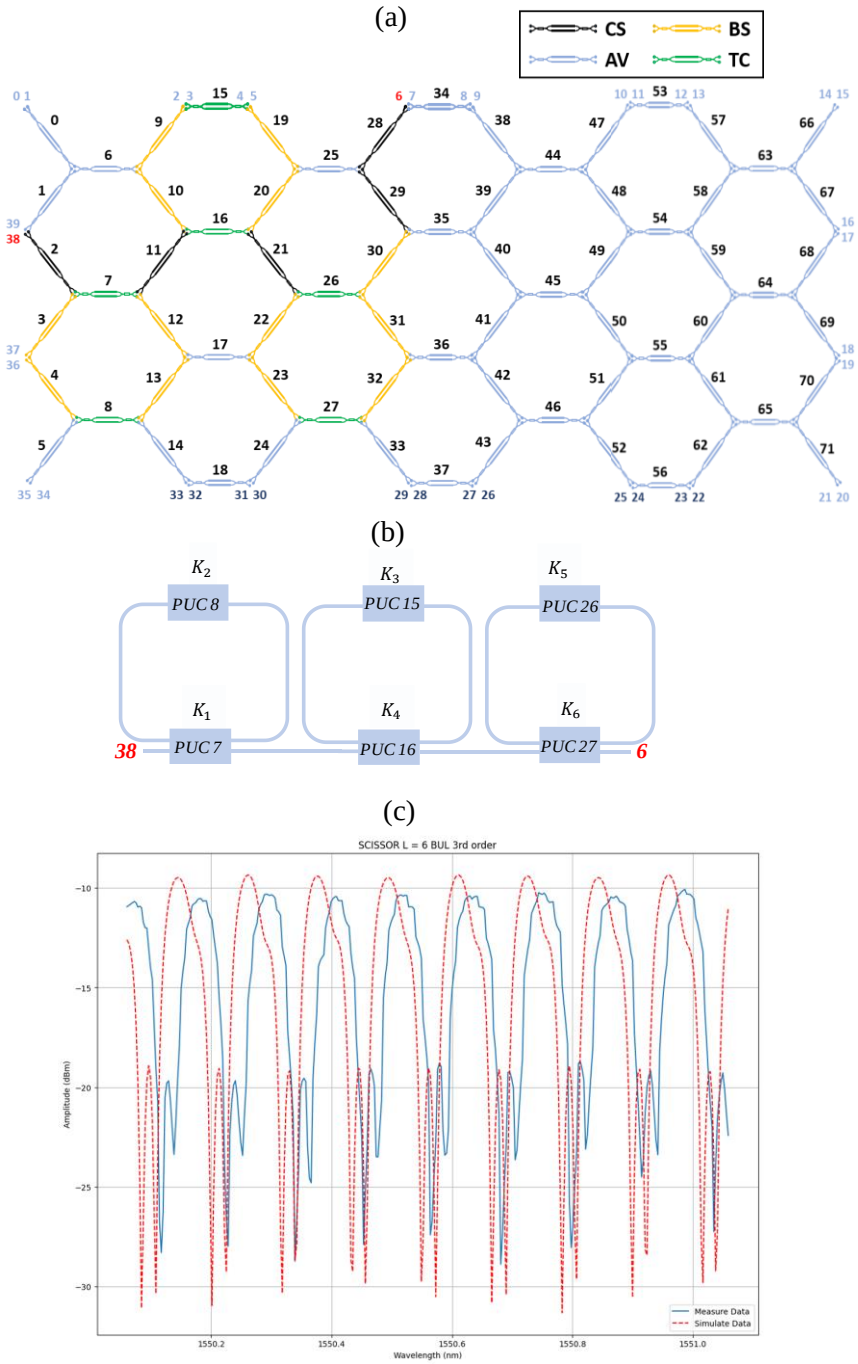

Figure 3.16. (a) Waveguide mesh arrangement of 72 programmable unit cells configured as an OADM filter of L = 6 BUL SCISSOR 3rd order filter. CS, cross state; BS, bar state; AV, available; TC, tuneable coupler (b) Equivalent circuit (c) Measured transfer function versus simulated response using the developed tool.

The last type of complex filters, which we measured and demonstrated by synthetizing the mesh, are ring loaded UMZIs. Next, we will test a single RAMZI and a single second order lattice RAMZI filter, as can be seen in Figure 3.17. (a)-(b) and Figure 3.18. (a)-(b).

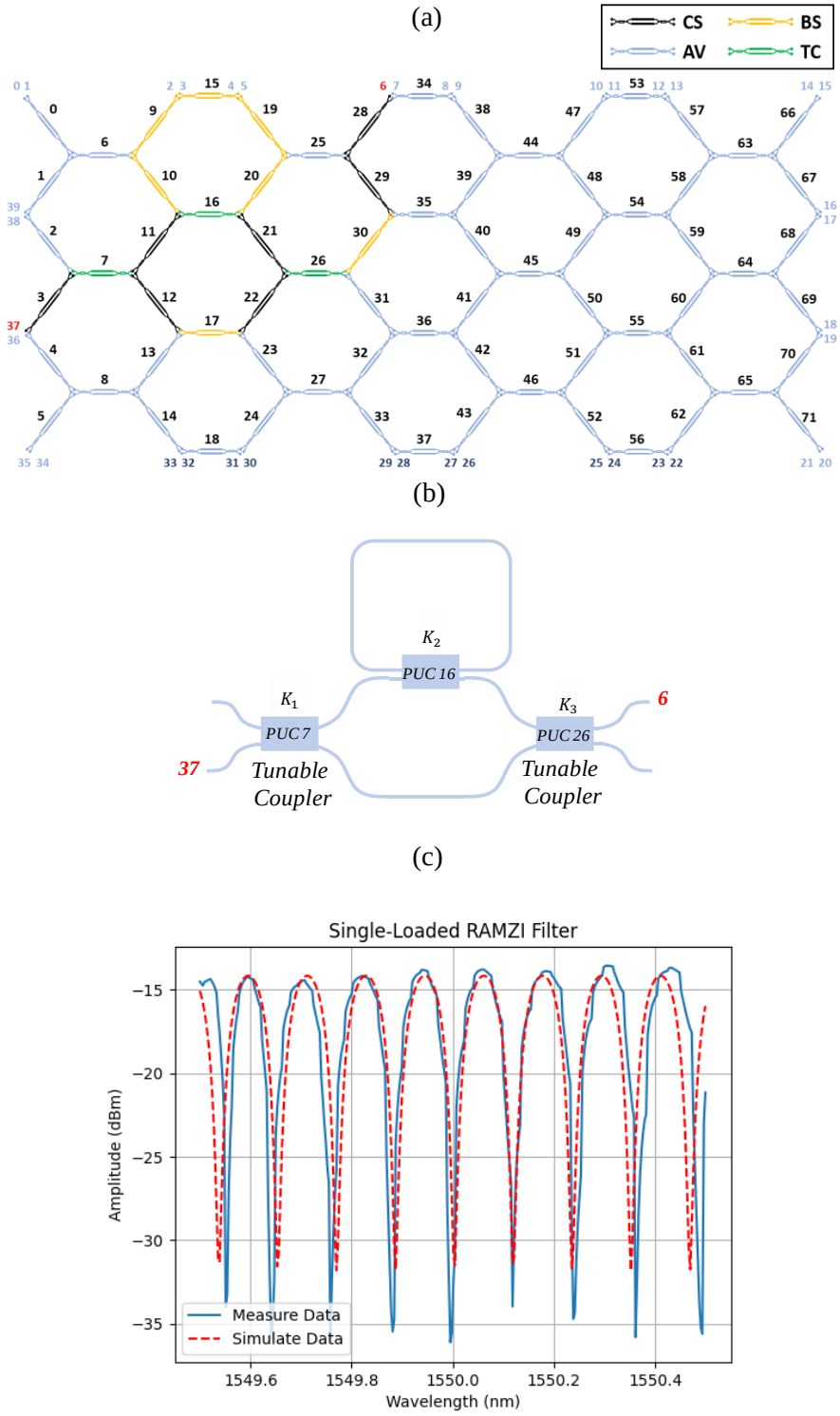

Figure 3.17. (a) Waveguide mesh arrangement of 72 programmable unit cells configured as Single Loaded RAMZI filter. CS, cross state; BS, bar state; AV, available; TC, tuneable coupler (b) Equivalent circuit (c) Measured transfer function versus simulated response using the developed tool.

As can be seen in Figure 3.17. (c) and Figure 3.18. (c), the Single Loaded RAMZI (SL-RAMZI) Filter and Single Loaded RAMZI lattice filter of 2nd order, synthesized achieve both a FSR = 0.12nm (15GHz) and an ER = 20dB.

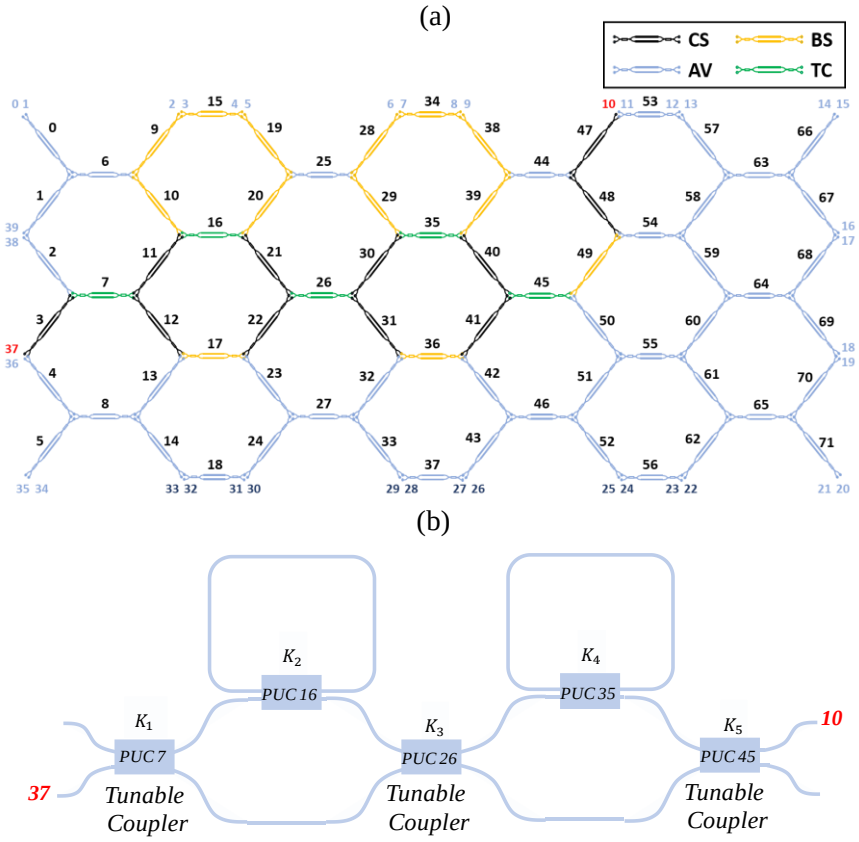

Figure 3.18. (a) Waveguide mesh arrangement of 72 programmable unit cells configured as a Single Loaded RAMZI lattice filter of 2nd order. CS, cross state; BS, bar state; AV, available; TC, tuneable coupler (b) Equivalent circuit (c) Measured transfer function versus simulated response using the developed tool.

3.3.4. Simultaneity of structure synthesis

Finally, we fully exploit the functionality of being able to set several structures simultaneously in the hexagonal mesh and monitor their outputs. In Figure 3.19. (a)-(b), we simulate an unbalanced Mach-Zehnder interferometer, a double loaded RAMZI (DL-RAMZI), and an optical ring resonator and compare their responses with the experimental measurements. Moreover, we evaluate the optical crosstalk. Using the input light at the UMZI input port (Port 0), we measured the transmission response in each output of these three filters. After, we made the same test with the input light at the DL-RAMZI input (Port 35) and with the input light at the ORR input (Port 15). The results of the optical crosstalk are shown in Figure 3.19. (c). As can be noticed from the figures, up to 60dB of optical rejection was obtained.

3.4. Conclusions

The simulation of highly coupled waveguide elements with dynamic configuration and performance is critical for the design and configuration of scalable programmable circuits. In this chapter, we have proposed a computational method based on single-cell inductive approach methodology. Next, we have reported and benchmarked the elapsed computational times and accuracy trade-off of the method, compared with other two, for a set of representative application examples and circuit sizes. We concluded that for applications with many optical paths and high number of feedback and feedforward loops, the inductive methodology performs better simulations. Moreover, the use of the inductive approach provides faster simulation times for arbitrary complex circuits requiring large number of optical ports. In addition, the method presented here can be applied to any highly coupled circuit topology (square, hexagonal, triangular, feedforward, etc.). Therefore, it unfolds as an effective and versatile tool for the study of emerging multipurpose programmable photonic processors. Likewise, the expansion of the technology will demand efficient characterization and calibration protocols [47], improved automated configuration routines [40], [45] and resource optimization libraries. This method reduces development costs, speed up the growth of new circuit designs, and are a fundamental tool for the development of programmable photonic libraries. Finally, it has been presented measurements as a proof of concept that the described simulation tool can be used to predict and study the behaviour of any structure synthesized in the programmable processor before measuring it experimentally. Thus, simplifies and accelerates the experimental characterization of these structures. The dissemination of these results have been published in Journal [J.1] and in the contribution in congress [C.1].

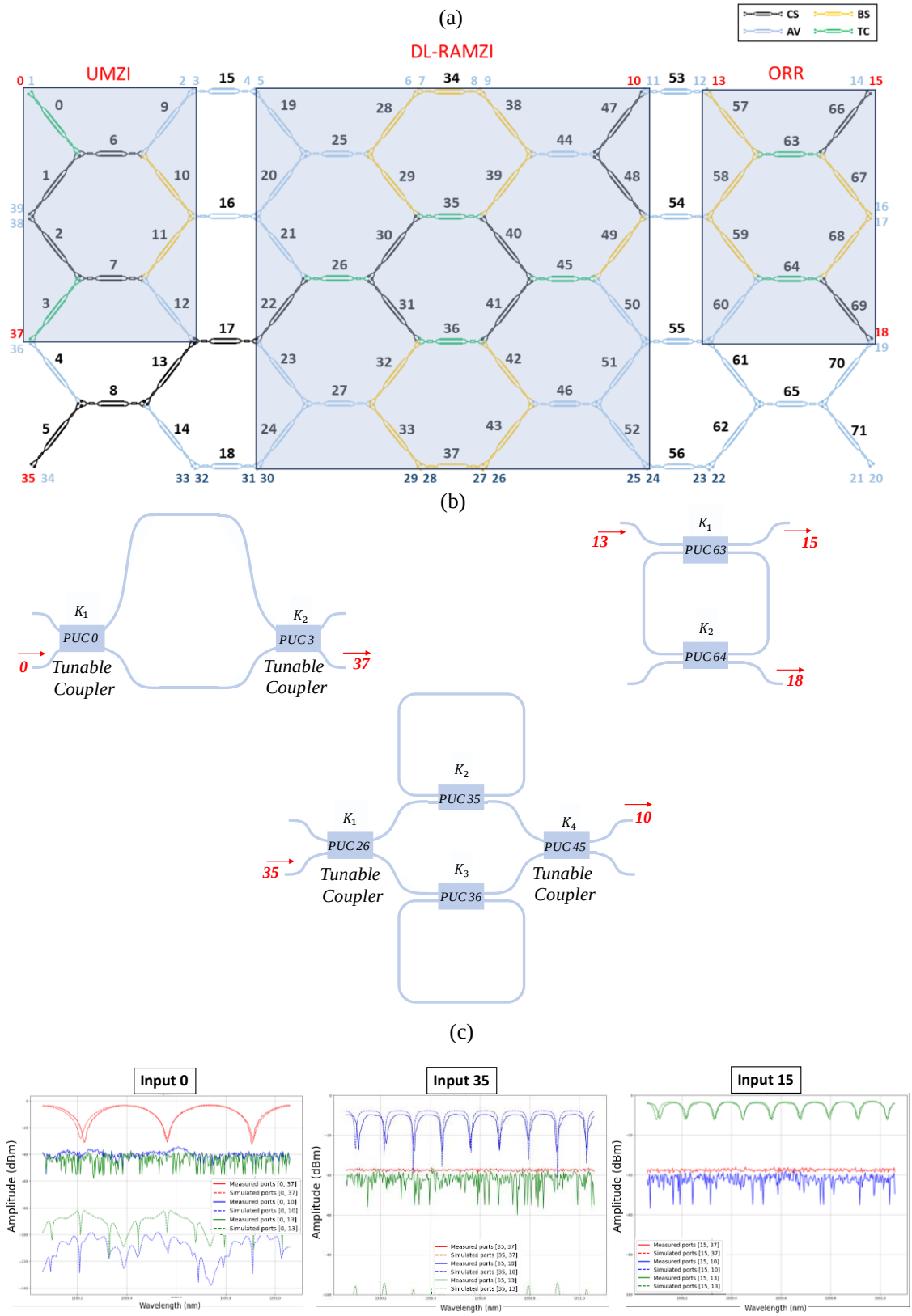

Figure 3.19. (a) Waveguide mesh arrangement of 72 programmable unit cells configured as 3 simultaneous schemes: UMZI, DL-RAMZI, and ORR. CS, cross state; BS, bar state; AV, available; TC, tuneable coupler (b) Equivalent circuits (c) Measured modulus transfer function versus simulated response using the developed tool, for each input port.

Chapter 4. End-to-end Analytical Model of Amplified Links

4.1. Introducción

For several decades Microwave Photonic systems have been described by relatively simple configurations that included a direct or external modulated optical transmitter, a dispersive optical fiber link, and a broadband linear optical receiver [48]–[50]. Their main role was to provide broadband and highly linear end-to-end links, capable of transmitting radiofrequency analog signals leveraging on the unique properties of optical fibers in terms of low loss, electromagnetic immunity, and broadband operation [51]. These configurations were well suited for the niche applications in security and defense targeted by early adopters.

However, the surge of new and emerging applications such as 5/6G mobile communications, Internet of Things (IoT), and industry 4.0 calls for MWP systems with increased complexity [17] that can guarantee a smooth interface between optical fiber based transport networks and wireless edge segments.

Adding complexity in MWP systems implies empowering their photonic cores with the capability of performing in-flight arbitrary optical signal processing tasks, such as filtering, beam-steering, long distance transmission, signal generation/conditioning, and Analog-to-Digital Converter (ADC) to cite some examples. This can be achieved by either fiber-based configurations or, most likely with photonic integrated circuits. The addition of this processing capability can be modelled by including an arbitrary passive filter transfer function $H(\omega)$ in the optical part of the link and several works [52]–[55] have reported the derivation of the fundamental figures of merit of these complex systems.

As complexity grows and/or more distance is covered by MWP, losses increase and there will be a need for incorporating optical amplification to improve the link performance [53]: Erbium Doped Fiber Amplifier (EDFA) based in fiber links and Semiconductor Optical Amplifiers based in systems including PICs. The inclusion of optical amplifiers has been considered [16] and experimentally studied [54] in simple MWP links with intensity modulation and direct detection and links with amplified self-heterodyne frequency converters. Moreover, it has attempted to model theoretically the key metrics to analyse the MWP filter links and systems [55]. However, expressions that define in a closed way the effects of these amplifiers to the FOM of the links have not been reached in the case of links with intensity modulation and direct detection. Another class of MWP systems exploits the receiver stage to provide the desired RF frequency up-conversion prior to antenna radiation [56]. This is achieved by coherent heterodyne detection, where a local laser oscillator is combined with the link signal instead of using the same input laser subject to parallel modulation by the RF and the local oscillator as proposed by Bottenfield and co-workers [57]. Moreover, in [57] full expressions for amplified heterodyne microwave photonic links have been derived although in the absence of optical filtering.

4.2. Modelling and analysis amplified arbitrary filtered microwave photonic links and systems

In this chapter, we develop an analytical model for amplified complex MWP systems. It provides the expressions for the main figures of merit (i.e. radio frequency gain, noise figure, and dynamic range) for the case of intensity modulation and contemplates the cases of power amplification (i.e. OA placed after the transmitter), intermediate amplification (i.e. amplifier inside the optical processing/distributing core), and pre amplification (i.e. OA placed before the detector).

In addition, we describe an end-to-end model expressions for the main FOMs for the case of In-phase and Quadrature (IQ) modulation with balanced detection. A distinctive feature of this model as compared to others reported before [55], [57] is that it accounts for the impact of an arbitrary large chain of amplifier plus filter sections. These sections do not need to be identical, furthermore, they can be individually different. Thus, it can be applied to systems ranging from very simple to very complex configurations by scaling the number of sections in the system.

The models enable a flexible evaluation of the position on the OA and the overall impact of the performance of each subsystem. Finally, an application example of each model is applied to specific cases.

4.2.1. Intensity modulation with direct detection derivation

A SOA is an optoelectronic device that can amplify an input light signal. The active region in the device is able to amplify the signal due to the gain generated by stimulated emission. However, the noise generated internally by spontaneous emission, which is also amplified in the device, is added to the output signal. This Amplified Spontaneous Emission (ASE) noise is produced by the amplification process itself and it cannot be avoided [22]. The effect of this noise on the MWP link/system performance is the main focus of this section.

Conventional FOMs for MWP links (gain, noise, and dynamic range) are evaluated using general expression of the RF gain, noise figure (or Relative Intensity Noise, RIN), and spurious free dynamic range, respectively. These FOMs are usually employed to analyze signal degradations due to noise sources [52]–[55], [16]]. For that, we define the RF Gain as the ratio between the input RF power ($P_{RFin}(\Omega)$) and the output RF photodetected power ($P_{RFout}(\Omega)$):

$$G_{RF}(\Omega) = \frac{P_{RFout}(\Omega)}{P_{RFin}(\Omega)} = G^2 G^I_{RF-PF} = \\ = G^2 \cdot \frac{1}{16}\left(\frac{\eta e P_{in}\alpha_{mzm}\pi}{\hbar\omega_o V_\pi}\right)^2 \sin^2(\phi_{dc}) R_{in} R_{out} \left|\frac{H_0(\omega_o)H_0^*(\omega_o-\Omega)+H_0^*(\omega_o)H_0(\omega_o+\Omega)}{2}\right|^2 \quad (4.1)$$

where G is the gain of the optical amplifier used and $H_0(\omega)$ is the arbitrary transfer function of the optical system in the MWP link [16], [51], [52], [55] that incorporates all the losses (i.e. it is given by $H_0(\omega) = L^{1/2} H(\omega)$, where $H(\omega)$ is a lossless transfer function and L represents the loss coefficient).

On the other hand, the relative intensity noise (RIN_{TOT}) is defined in Eq. (4.2) and the total output spectral density noise (N_{TOT}) is shown in Eq. (4.3).

$$RIN_{TOT} = \frac{N_{TOT}(f)}{i_{dc}^2 R_{OUT}} \quad (4.2)$$

where i_{dc} is the DC component from the signal current and R_{OUT} is the load resistance.

$$N_{TOT} = N_{sig-sp}(f) + N_{sp-sp}(f) + N_{sp-shot}(f) + N_{thermal,i}(f) + N_{thermal,o}(f) + N_{sig-shot}(f) \tag{4.3}$$

Thermal input ($N_{thermal,i}$) and thermal output ($N_{thermal,o}$) noises generated due to the modulator and the receiver electronics respectively, and signal-shot noise ($N_{s\text{-}shot}$) generated during the photodetection, are common noise sources in any MWP link. Moreover, the spontaneous emission from the optical amplifier generates three types of additional noises in the electrical domain [58]. First, the spontaneous emission beats with the signal during photodetection and produces a noise ($N_{sig\text{-}sp}$). Secondly, the spontaneous emission noise is beaten with itself ($N_{sp\text{-}sp}$) during the photodetection stage. Finally, shot noise is produced proportional to the average spontaneous emission noise power ($N_{sp\text{-}shot}$). Therefore, final noise figure of the MWP link is evaluated using the above noise expressions and using the general expression of this figure derived in Eq. (4.4).

$$NF = \frac{N_{TOT}}{G_{RF} k_B T} \tag{4.4}$$

Using Eq. (4.2), the equation of noise figure can be rewritten as a function of the relative intensity noise as:

$$NF = \frac{RIN_{TOT} i_{dc}^2 R_{out}}{G_{RF} k_B T} \tag{4.5}$$

Then, the link dynamic range can be evaluated with the second and third order SFDRs, using the second-order and third-order output intercept points respectively (OIP_2 and OIP_3) is obtained using Eq. (6) and Eq. (7) [16]:

$$SFDR_2 = \left[\frac{OIP_2}{N_{TOT}} \right]^{1/2} = \left[\frac{OIP_2}{RIN_{TOT} i_{dc}^2 R_{OUT}} \right]^{1/2} \tag{4.6}$$

$$SFDR_3 = \left[\frac{OIP_3}{N_{TOT}} \right]^{2/3} = \left[\frac{OIP_3}{RIN_{TOT} i_{dc}^2 R_{OUT}} \right]^{2/3} \tag{4.7}$$

where, N_{TOT} is the total noise power density distribution defined in Eq. (4.3) and the output intercept point (OIP) is the output power at the intersection of the extrapolated small-signal responses of the fundamental tone and the nth-order distortion. The OIPs are obtained using RF photodetected power relative to the signal contribution and relative to the intermodulation distortions (IMD_2 and IMD_3) expressions [51]. Moreover, the OIPs do not change with respect to the passive case as the output RF powers of both the fundamental and intermodulation terms scale equally with G^2.

The FOMs of an amplified filtered MWP link are reported for the case of intensity modulation and direct detection, but the same methodology can be applied to extend the model to alternative modulation and detection techniques. The aim of this model is to provide the FOMs of an arbitrary filtered MWP link system containing an optical amplifier such as SOA/EDFA at different positions of a general MWP link as shown in Fig. 1. Point A corresponds to the power-amplification case, point B is in-line-amplification and point C represents the pre-amplification case.

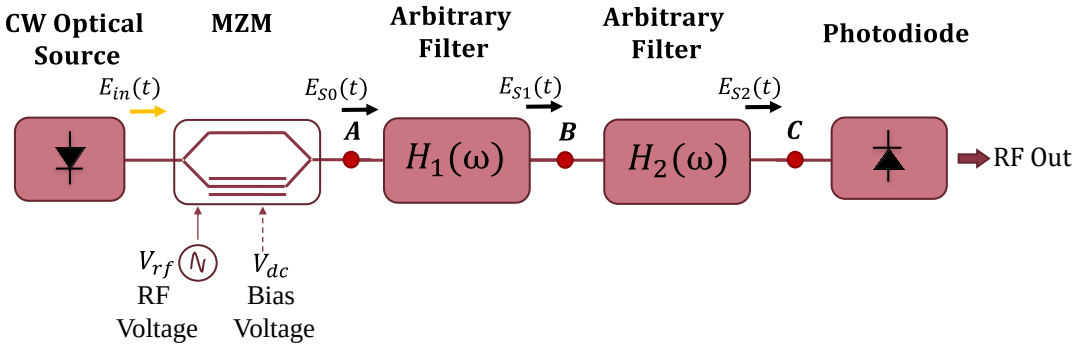

Figure 4.1. Schematic of an amplifier filtered MWP system (point A power-amplified, point B in-line amplified, and point C pre-amplified) link.

Referring to Figure 4.1, the input optical field to the link is defined as:

$$E_{in}(t) = \sqrt{P_{in}} e^{(j\omega_0 t)} \tag{4.8}$$

where the optical field $E_{in}(t)$ is the one generated by the optical source and P_{in} is optical power at frequency ω_0 [16].
Then, the Mach-Zehnder modulator modulates the RF information onto the laser intensity [16]. Hence, $E_{S0}(t)$ is the optical field at the output of the modulator, and it is expressed as:

$$E_{S0}(t) = j\sqrt{\alpha_{mzm}} E_{in}(t) \sin\left(\frac{\phi_{dc}}{2} + \frac{\phi_{rf}}{2}\sin(\Omega t)\right) \tag{4.9}$$

with,

$$B_n = (-1)^n j^{|n|+1} \sin\left(\frac{\phi_{dc}}{2} + |n|\frac{\pi}{2}\right) \tag{4.10}$$

where α_{mzm} are the losses due to the modulator, $\Phi_{dc} = (\pi V_{dc})/V_\pi$ and $\Phi_{rf} = (\pi V_{rf})/V_\pi$ for the bias voltage V_{dc} and the RF voltage V_{rf} respectively, V_π is the modulator half-way voltage and Ω is the angular frequency of the RF tone. Afterwards, the field can be simplified as:

$$E_{S0}(t) = j\sqrt{\alpha_{mzm} P_{in}} e^{j\omega_0 t} \sum_{n=-\infty}^{\infty} B_n J_n\left(\frac{\phi_{rf}}{2}\right) e^{jn\Omega t} \tag{4.11}$$

Then, in the Power-Amplified Link systems the amplifier is located in point A, previous to the arbitrary filter/optical core as can you see in Figure 4.2.

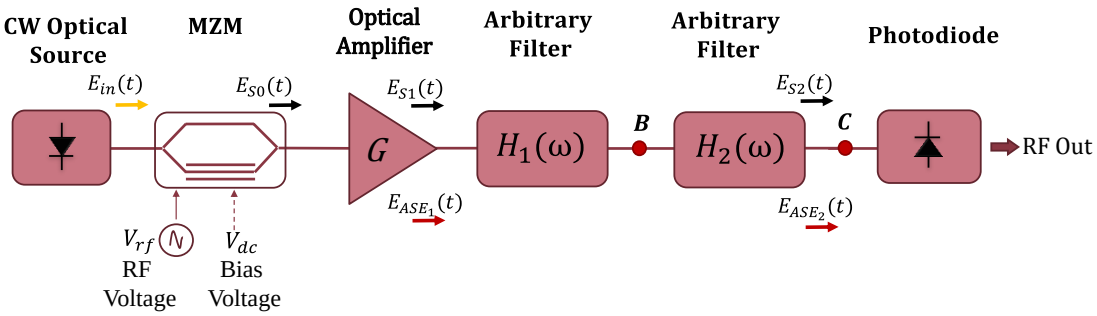

Figure 4.2. Schematic of power-amplified filtered MWP link/system for the analysis.

Here, $E_{S1}(t)$ is the optical field at the output of the amplifier given by:

$$E_{S1}(t) = \sqrt{G}E_{S0}(t) \tag{4.12}$$

where G is the optical amplifier gain and $E_{S0}(t)$ is the optical field at the output of the modulator, previously defined in Eq. (4.11).

Finally, $E_{S2}(t)$ is the field at the output of the filter. This means that this field will go through the photodetector following the expression:

$$E_{S2}(t) = E_{S1}(t) * h_0(t) \tag{4.13}$$

where $h_0(t)$ is the impulse response corresponding to the arbitrary filter frequency response $H_0(\omega_0)$. In this case, it should be considered that the response $h_0(t)$ is the combination of two transfer functions of the two arbitrary filters employed in the MWP link:

$$h_0(t) = h_1(t) * h_2(t) \tag{4.14}$$

Thus, the field described in Eq. (4.13) can be defined as:

$$E_{S2}(t) = j\sqrt{G\alpha_{mzm}P_{in}}\sum_{n=-\infty}^{\infty} B_n J_n\left(\frac{\phi_{rf}}{2}\right) H_0(\omega_0 + n\Omega)e^{j(\omega_0+n\Omega)t} \tag{4.15}$$

On the other hand, $E_{ASE1}(t)$ is the ASE field generated due to an active element like the OA and it is defined as:

$$E_{ASE1}(t) = \sqrt{N\hbar\omega_0\partial\omega}\sum_{k=-M}^{M} e^{j[(\omega_0+k\partial\omega)t+\varphi_k]} \tag{4.16}$$

where N, which is the ASE photon number output from the amplifier that is added to the signal, is given by $N = n_{sp}(G-1)$ (it is derived from quantum theory [58]) and n_{sp} is the population inversion factor, $\hbar$ is the Planck constant divided by 2π, ω_0 is the central frequency, $\delta\omega$ is the frequency discretization interval for the ASE spectrum ($B_{ASE} = 2M\delta\omega$), M is the number of ASE modes and φ_k is a random phase corresponding to the frequency discretize k. The total ASE noise field is assumed to be composed by the superimposition of 2M independent radiation modes at the optical frequency $\omega_0+k\delta\omega$ with a random phase φ_k.

Assuming that the ASE field from Eq.(4.16) propagates through the optical filter, the $E_{ASE2}(t)$ is calculated as:

$$E_{ASE2}(t) = E_{ASE1}(t) * h_0(t) \tag{4.17}$$

Replacing Eq. (4.14) and Eq. (4.16) in Eq. (4.17), we can obtain:

$$E_{ASE2}(t) = \sqrt{N\hbar\omega_0\partial\omega}\sum_{k=-M}^{M} H_0(\omega_0 + k\partial\omega)e^{j[(\omega_0+k\partial\omega)t+\varphi_k]} \tag{4.18}$$

Afterward, photodetectors transfer intensity variations in the optical power to amplitude variations in the output photocurrent. So, then the instantaneous photocurrent i(t) at the output of the photodetector is given by:

$$i(t) = \Re[E_{S2}(t) + E_{ASE2}(t)]^2 \tag{4.19}$$

where the photodetector responsivity is defined like $\Re = \eta e/h\omega_0$, η is the photodiode quantum efficiency and e is the electron charge constant. Developing Eq. (4.19), we can obtain:

$$i(t) = \underbrace{\Re\left|E_{S2}(t)\right|^2}_{i_{S2}(t)} + \underbrace{\Re\left|E_{ASE2}(t)\right|^2}_{i_{sp-sp}(t)} + \underbrace{\Re\left|E^*_{ASE2}(t)E_{S2}(t) + E^*_{S2}(t)E_{ASE2}(t)\right|}_{i_{sig-sp}(t)} \tag{4.20}$$

The first term is the detected signal ($i_{S2}(t)$), the second and the third terms are the spontaneous-spontaneous and the signal-spontaneous beating noise currents generated respectively. From these definitions, the noise formulas will be developed.

From the third term of Eq. (4.20), we can obtain the signal-spontaneous photocurrent as:

$$i_{sig-sp}(t) = \Re[E^*_{ASE2}(t)E_{S2}(t) + E^*_{S2}(t)E_{ASE2}(t)] \tag{4.21}$$

Developing Eq. (4.21), the time average of the squared photocurrent is given by:

$$\left\langle i^2_{sig-sp}(t)\right\rangle = 2\Re^2\alpha_{mzm}GP_{in}N\hbar\omega_0\left|H_0(\omega_0)\right|^2 B_{0,eq}\sum_{n=-\infty}^{\infty}\left|B_n\right|^2 J_n^2\left(\frac{\phi_{rf}}{2}\right)\left|H_0(\omega_0+n\Omega)\right|^2 \tag{4.22}$$

The dominant term is for n=0. Then, neglecting the rest of the contribution, we obtain:

$$\left\langle i^2_{sig-sp}(t)\right\rangle = 2\Re^2\alpha_{mzm}GP_{in}N\hbar\omega_0\left|H_0(\omega_0)\right|^4 B_{0,eq}\sin^2\left(\frac{\phi_{dc}}{2}\right) \tag{4.23}$$

Using the time average of the squared photocurrent calculated in Eq. (4.23) and the mean squared of the photocurrent ($\langle i_{sig\text{-}sp}(t)\rangle^2$), which is zero in this case, we can compute the variance as:

$$\left\langle \sigma^2_{sig-sp}\right\rangle = \left\langle i^2_{sig-sp}(t)\right\rangle - \left\langle i_{sig-sp}(t)\right\rangle^2 = \eta^2\alpha_{mzm}GI_N I_S(1-\cos(\phi_{dc}))\left|H_0(\omega_0)\right|^2 \tag{4.24}$$

Then, the noise current (I_N) and the signal current (I_S) are given by Eq. (4.25) and Eq. (4.26) respectively.

$$I_N = eN \int_{-\infty}^{\infty} \left|H_0(\omega_0)\right|^2 \partial\omega \tag{4.25}$$

$$I_S = \frac{eP_{in}}{\hbar\omega_0} \tag{4.26}$$

where I_N will be limited by the equivalent bandwidth of the optical filter used.

Subsequently, the noise power density distribution (in watts) is calculated integrating the spectral distribution derived in Eq. (4.24), along a uniform equivalent arbitrary filter with a single-side bandwidth given by $B_{o,eq}/2$. Moreover, it is multiplied by R_{OUT} obtaining [58]:

$$N_{sig-sp}(f) = \frac{2\left\langle \sigma^2_{sig-sp} \right\rangle R_{OUT}}{B_{o,eq}} = \frac{2\eta^2 \alpha_{mzm} G I_N I_S (1-\cos(\phi_{dc}))R_{OUT}}{B_{o,eq}} \left|H_0(\omega_0)\right|^2 \tag{4.27}$$

A similar derivation can be performed for the spontaneous-spontaneous current.

$$i_{sp-sp}(t) = \Re\left|E_{ASE2}(t)\right|^2 \tag{4.28}$$

From Eq. (4.28), the variance can be computed as:

$$\left\langle \sigma^2_{sp-sp} \right\rangle = \eta^2 I_N^2 \left|H_0(\omega_o)\right|^2 \tag{4.29}$$

Finally, the noise power density distribution is defined as:

$$N_{sp-sp}(f) = \frac{2\eta^2 I_N^2 R_{OUT} M_{sp}}{B_{eq,o}} \left|H_0(\omega_o)\right|^2 \tag{4.30}$$

where, M_{sp} accounts for the number of spontaneous emission modes (M_{sp} is either 1 or 2 depending on whether one or the two polarization states of spontaneous emission are considered) [58].

For spontaneous-shot noise, we can use the second term of Eq. (4.20) to calculate its variance which is given by:

$$\left\langle \sigma^2_{sp,shot} \right\rangle = 2e\left\langle i_{sp-sp}(t) \right\rangle \tag{4.31}$$

Using Eq. (4.31) and Eq. (4.28), the noise power density distribution of shot noise due to amplified spontaneous emission power is calculated as:

$$N_{sp-shot}(f) = \left\langle \sigma^2_{sp,shot} \right\rangle R_{OUT} = 2e\eta I_N M_{sp} R_{OUT} \tag{4.32}$$

Following Eq. (4.20) and Eq. (4.15), the detected signal is given by:

$$i_{S2}(t) = \Re\left|E_{S2}(t)\right|^2 = \tag{4.33}$$
$$= \Re G\alpha_{mzm} P_{in} \sum_{n=-\infty}^{\infty} \sum_{m=-\infty}^{\infty} B_n B_m^* J_n\left(\frac{\phi_{rf}}{2}\right) J_m\left(\frac{\phi_{rf}}{2}\right) H_0(\omega_0 + n\Omega) H_0^*(\omega_0 + m\Omega) e^{j(n-m)\Omega t}$$

From Eq. (4.33), the DC component can be computed in the case of m = n and assuming that the dominant term is for n = 0.

$$i_{dc} = \eta G I_S \alpha_{mzm} \sin^2\left(\frac{\phi_{dc}}{2}\right)\left|H(\omega_o)\right|^2 \tag{4.34}$$

Then, using Eq. (4.34), signal-shot noise spectral power density will be:

$$N_{sig-shot}(f) = 2e\left\langle i_{dc}(t)\right\rangle R_{OUT} = e\eta G\alpha_{mzm} I_S (1-\cos(\phi_{dc}))R_{OUT}\left|H_0(\omega_o)\right|^2 \tag{4.35}$$

The output thermal noise is originated from the RF and electronic driving circuitry after the photodiode. The output noise spectral power density is:

$$N_{thermal,o}(f) = k_B T \tag{4.36}$$

where k_B is the Boltzmann constant, and T is the temperature in Kelvin degrees.

In the same way, the input thermal noise originated from RF and electronic driving circuitry of the modulator. So, the input noise spectral power density is given by:

$$N_{thermal,i-phd}(f) = G_{RF} N_{thermal,i}(f) \tag{4.37}$$

where G_{RF} is the RF gain of the link defined in Eq. (4.1).

Once we know all the noise spectral power densities generated in the link, we can use Eq. (4.2) to calculate the total relative intensity noise.

Then, from Eq. (4.2) the signal-spontaneous RIN can be derived using Eq. (4.27) and Eq. (4.34):

$$RIN_{sig-sp} = \frac{8I_N}{I_S G\alpha_{mzm}(1-\cos(\phi_{dc}))\left|H_0(\omega_0)\right|^2 B_{o,eq}} \tag{4.38}$$

In the same way, spontaneous-spontaneous RIN can be derived using Eq. (4.30) and Eq. (4.34):

$$RIN_{sp-sp} = \frac{8I_N^2 M_{sp}}{I_S^2 G^2 \alpha_{mzm}^2 (1-\cos(\phi_{dc}))^2\left|H_0(\omega_0)\right|^2 B_{eq,0}} \tag{4.39}$$

Also, the spontaneous-shot RIN is calculated from Eq. (4.32) and Eq. (4.34):

$$RIN_{sp-shot} = \frac{8eI_N M_{sp}}{\eta G^2 I_s^2 \alpha_{mzm}^2 (1-\cos(\phi_{dc}))^2\left|H_0(\omega_0)\right|^4} \tag{4.40}$$

Therefore, the signal-shot RIN can be expressed using Eq. (4.35) and Eq. (4.34).

$$RIN_{sig-shot} = \frac{4e}{\eta G I_S \alpha_{mzm}\left[1-\cos(\phi_{dc})\right]\left|H_0(\omega_0)\right|^2} \tag{4.41}$$

Lastly, the thermal output and input relative intensity noises are calculated using Eqs. (4.36) and (4.37) respectively and the DC the intensity component calculated in Eq. (4.34).

$$RIN_{th,o} = \frac{4k_B T}{\eta^2 G^2 \alpha_{mzm}^2 I_S^2 (1-\cos(\phi_{dc}))^2\left|H_0(\omega_0)\right|^4 R_{OUT}} \tag{4.42}$$

$$RIN_{th,i} = \frac{k_B T \pi^2 \sin^2(\phi_{dc}) R_{in} \left|H_0(\Omega)\right|^4}{16(1-\cos(\phi_{dc}))^2 V_\pi^2 \left|H_0(\omega_0)\right|^4} \tag{4.43}$$

where $|H_0(\Omega)|^2 = [H_0(\omega_0)\, H_0^*(\omega_0+\Omega) + H_0(\omega_0+\Omega)\, H_0^*(\omega_0)]$.

Finally, RIN_{TOT} is calculated in Eq. (4.44) as the addition of the six relative intensity noises Eqs. (4.38), (4.39), (4.40), (4.41), (4.42) and (4.43) obtained previously.

$$RIN_{TOT} = RIN_{sig-sp}(f) + RIN_{sp-sp}(f) + RIN_{sp-shot}(f) + RIN_{thermal,i}(f) + RIN_{thermal,o}(f) + RIN_{sig-shot}(f) \tag{4.44}$$

So, the noise figure of the link can be expressed as:

$$NF_{TOT} = NF_{sig-sp}(f) + NF_{sp-sp}(f) + NF_{sp-shot}(f) + NF_{thermal,i}(f) + NF_{thermal,o}(f) + NF_{sig-shot}(f) \tag{4.45}$$

where, using Eq. (4.4) each NF source can be expressed as:

$$NF_{sig-sp} = \frac{128 V_\pi^2 I_N (1-\cos(\phi_{dc})) \left|H_0(\omega_0)\right|^2}{\pi^2 R_{in} G \alpha_{mzm} I_S \sin^2(\phi_{dc}) \left|H_0(\Omega)\right|^4 B_{eq,o} k_B T} \tag{4.46}$$

$$NF_{sp-sp} = \frac{128 V_\pi^2 I_N M_{sp} \left|H_0(\omega_0)\right|^2}{\pi^2 R_{in} G^2 \alpha_{mzm} {I_S}^2 \sin^2(\phi_{dc}) \left|H_0(\Omega)\right|^4 B_{eq,o} k_B T} \tag{4.47}$$

$$NF_{sp-shot} = \frac{128 V_\pi^2 I_N e M_{sp}}{\pi^2 R_{in} G^2 \alpha_{mzm}^2 \eta I_S^2 \sin^2(\phi_{dc}) \left|H_0(\Omega)\right|^4 k_B T} \tag{4.48}$$

$$NF_{th,o} = \frac{1}{G_{RF}} \tag{4.49}$$

$$NF_{th,i} = 1 \tag{4.50}$$

$$NF_{sig-shot} = \frac{64 V_\pi^2 e (1-\cos(\phi_{dc})) \left|H_0(\omega_0)\right|^2}{\pi^2 R_{in} G \alpha_{mzm} \eta I_S \sin^2(\phi_{dc}) \left|H_0(\Omega)\right|^4 k_B T} \tag{4.51}$$

For the dynamic range calculation, we need the RF power at the output of the link. It can be obtained from the detected photocurrent (Eq. (4.33)), which delivers an electrical power to the output impedance R_{OUT} as:

$$P_{RF_{OUT}}(\Omega) = \frac{\left\langle \left|i_{S2}(\Omega,t)\right|^2 \right\rangle R_{OUT}}{2} = \frac{I_{dc}^2 \sin^2(\phi_{dc}) \phi_{rf}^2 \left|H_0(\omega_0) \cdot H_0^*(\Omega)\right|^4 R_{OUT}}{8} \tag{4.52}$$

The expression for the photodetected RF power relative to the IMD_2 term at the angular frequency $\Omega_1 \pm \Omega_2$ and relative to IMD_3 term at $2\Omega_1 \pm \Omega_2$ are obtained as Eqs. (4.53) and (4.54) respectively.

$$P_{RF_{OUT}}(\Omega_1 \pm \Omega_2) = \frac{I_{dc}^2 \left|IMD_2\right|^2 \phi_{rf}^4 R_{OUT}}{128} \tag{4.53}$$

$$P_{RF_{OUT}}(2\Omega_1 \pm \Omega_2) = \frac{I_{dc}^2 \left|IMD_3\right|^2 \phi_{rf}^6 \sin^2(\phi_{rf}) R_{OUT}}{8192} \tag{4.54}$$

where $IMD_2 = [IMD_{21}\text{-}IMD_{22}+\cos(\Phi_{dc})\,(IMD_{21}+IMD_{22})]$ and IMD_{21} and IMD_{22} are given by Eq. (4.55) and Eq. (4.56) respectively and IMD3 is given by Eq. (4.57):

$$IMD_{21}(\omega_0,\Omega_1,\Omega_2) = \left[H_0(\omega_0+\Omega_1)H_0^*(\omega_0+\Omega_2) + H_0(\omega_0-\Omega_2)H_0^*(\omega_0-\Omega_1) \right] \tag{4.55}$$

$$IMD_{22}(\omega_0,\Omega_1,\Omega_2) = \left[H_0(\omega_0)H_0^*(\omega_0-\Omega_1+\Omega_2) + H_0(\omega_0+\Omega_1-\Omega_2)H_0^*(\omega_0) \right] \tag{4.56}$$

$$IMD_3(\omega_0,\Omega_1,\Omega_2) = \begin{bmatrix} H_0(\omega_0)H^*(\omega_0-2\Omega_1+\Omega_2) + H_0^*(\omega_0)H(\omega_0+2\Omega_1-\Omega_2) + \\ +H_0(\omega_0+2\Omega_1)H^*(\omega_0+\Omega_2) + H_0(\omega_0-\Omega_2)H^*(\omega_0-2\Omega_1) \end{bmatrix} \tag{4.57}$$

Using Eqs. (4.52) and (4.53) we can calculate the OIP_2. Then, OIP_3 is obtained from Eqs. (4.52) and (4.54) respectively. It should be noted that these values of OIP_2 and OIP_3 defined in Eqs. (4.58) and (4.59) respectively remain unaltered for all the amplified link configurations.

$$OIP_2 = \frac{2R_{OUT}I_{dc}^2 \sin^4(\phi_{dc})\left|H_0(\Omega)\right|^8}{\left|IMD_2\right|^2} \tag{4.58}$$

$$OIP_3 = \frac{4R_{OUT}I_{dc}^2 \sin^2(\phi_{dc})\left|H_0(\Omega)\right|^6}{\left|IMD_3\right|} \tag{4.59}$$

After all, using Eqs. (4.6) and (4.7) the SFDR can be calculated with the OIPs and N_{TOT} expressions derived above.

$$SFDR_2 = \left[\frac{OIP_2}{N_{TOT}}\right]^{1/2} = \sqrt{\frac{2R_{OUT}I_{dc}^2 \sin^4(\phi_{dc})\left|H_0(\Omega)\right|^8}{\left|IMD_2\right|^2 N_{TOT}}} \tag{4.60}$$

$$SFDR_3 = \left[\frac{OIP_3}{N_{TOT}}\right]^{2/3} = \sqrt[3]{\left(\frac{4R_{OUT}I_{dc}^2 \sin^2(\phi_{dc})\left|H_0(\Omega)\right|^6}{\left|IMD_3\right| N_{TOT}}\right)^2} \tag{4.61}$$

It should be pointed out that the model Eqs. (4.12) - (4.61) converge exactly to those derived in [52] for the case of passive arbitrary MWP links, i.e. when G = 1 (no amplification).

In contrast with the power amplifier case, if the amplifier is placed in-line, see Figure 4.3, the noise is only filtered by the second filter. Therefore, the theoretical derivations for these MWP links/systems are similar to those of power amplification except that the optical filter transfer function used in Eq. (4.25) is given now by $H_0(\omega_0) = H_2(\omega_0)$. It means that is only in relation to amplifier noise where $H_1(\omega_0)$ has no effect.

The FOMs for this case can be calculated using the same generic expressions derived above, taking into account the prescription given in the former paragraph.

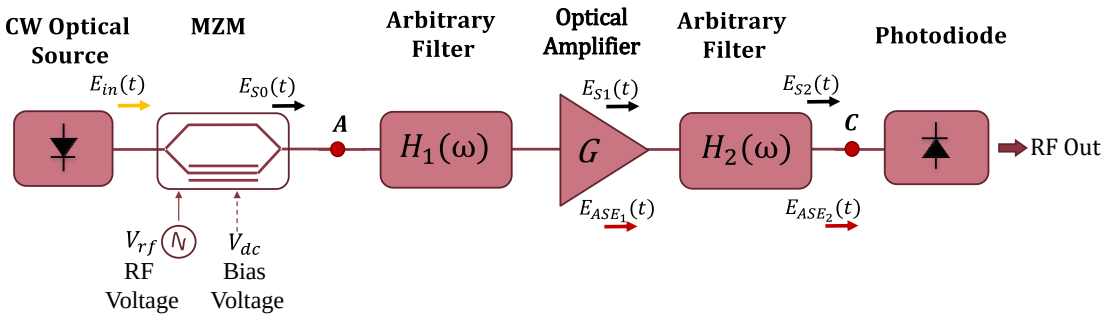

Figure 4.3. In-line-amplified filtered MWP link/system for the analysis.

In a similar way, when the amplifier is after the filter, as shown in Figure 4.4, the noise generated due to the amplifier is not filtered.

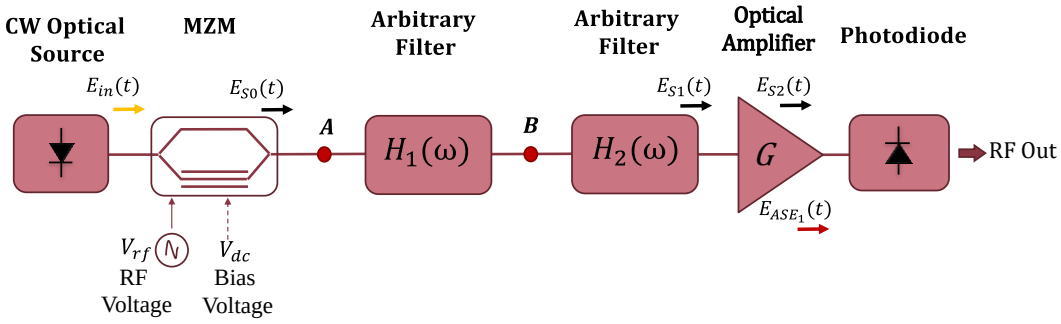

Figure 4.4. Pre-amplified filtered MWP link/system for this analysis.

Hence, applying an equivalent flat-top optical filter response to the arbitrary filter, we can redefine noise current from Eq. (4.25) as:

$$I_N = eNB_{o,eq} \tag{4.62}$$

where $B_{o,eq}$ is the equivalent optical filter bandwidth defined in [58]. Finally, the signal current is defined following Eq. (4.26) and the FOM can be analyzed using the generic expressions derived before.

4.2.1.1. Discrete and integrated MWP links simulation with intensity modulation and direct detection

At this point, as a proof of concept, we have applied the analytical model to evaluate interesting but quite different applications. We employed Python programming language to analyze both amplified arbitrary filtered microwave photonic links and integrated MWP systems. The model achieves complete flexibility and versatility to obtain the impact of the components on the overall system/link performance.

The first example corresponds to a MWP optical fiber link, implemented by two sections of dispersive Single Mode Fibers (SMF) with a total length of 35Km shown in Figure 4.5. For this example, we set the optical amplifier gain and the noise figure to 13dB and 6dB respectively. These values are based on typical specifications of a commercial EDFA.

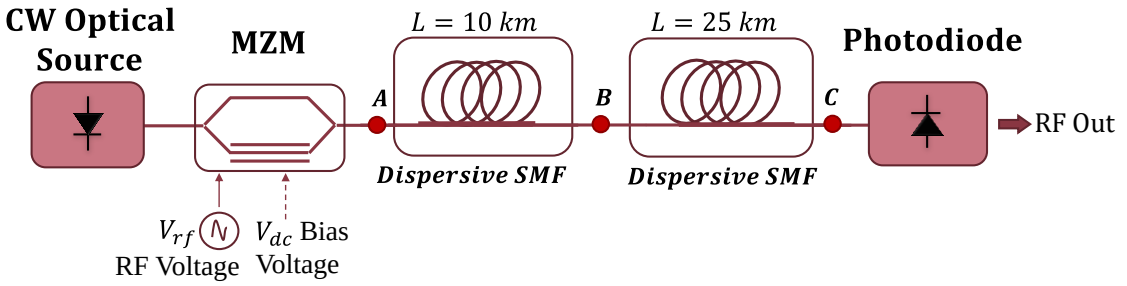

Figure 4.5. Schematic of an amplifier filtered MWP system (point A power-amplified, point B in-line amplified, and point C pre-amplified) optical link of 35km.

We set two tones at microwave frequencies of f_1 = 4.1GHz and f_2 = 4.2GHz, at the input of the intensity modulator, to carry out the dynamic range evaluation. The transfer functions of the two dispersive SMF fibers elements are given by $H_1(\omega_0) = H_2(\omega_0) = e^{-\alpha L/2} e^{-j\beta L}$, observe Figure 4.6, where α is the fiber optical loss (0.2 dB/km), L is the length of each fiber spool and β is the propagation constant. Here, the fiber is divided in two spools with lengths L = 10km and L = 25km (the total length of the dispersive stage is 35km) and the equivalent optical filter bandwidth is 200GHz [16], [58]. Finally, a photodetector is placed at the end of the link. The following parameters have fixed values: the modulator half-way voltage V_π = 5V, quadrature MZM bias point $\Phi_{dc} = \pi/2$, optical input power P_{in} = 7dBm, responsivity of photodetector $\Re$ = 0.6 A/W, modulator insertion losses α_{mzm} = 8dB, photodiode quantum efficiency η = 1 and input and output loads $R_{in} = R_{out}$ = 50Ω.

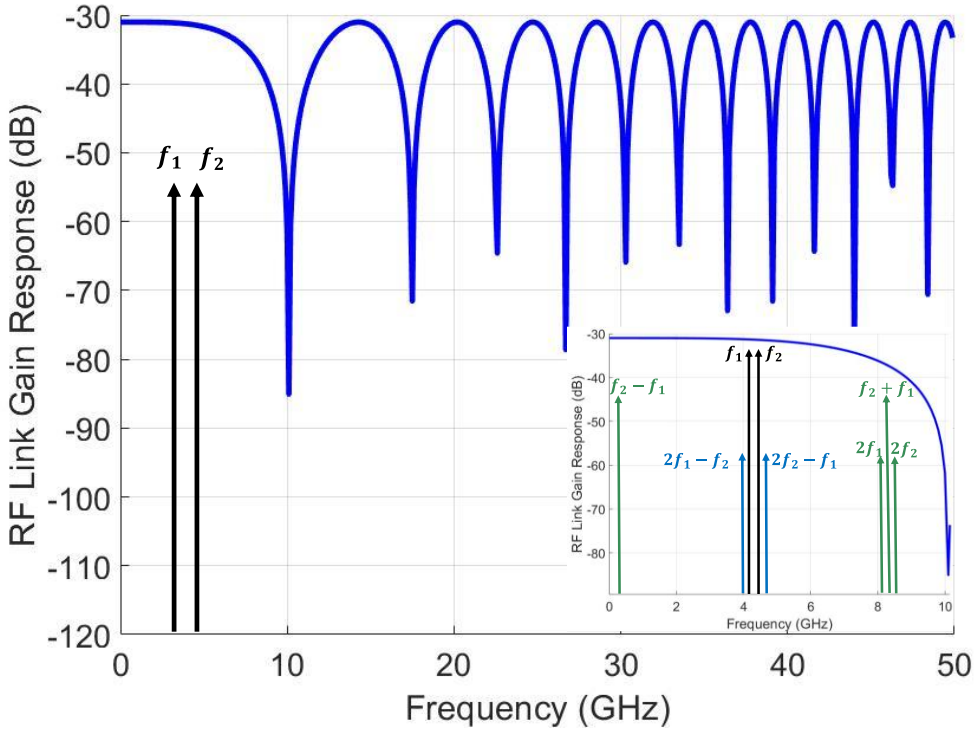

Figure 4.6. Analytical simulation of G_{RF} response in the dispersive link for intensity modulation with 10km and 25km SMF elements. The optical amplifier gain and the noise figure is set to 13dB and 6dB respectively. The inset shows the G_{RF} response with the location of f_1, f_2, and the distortion terms (blue: 3rd order and green: 2nd order).

Table 4.1 shows a comparison of the FOMs values obtained from the model of the optical fiber MWP link in each case of amplification.

Table 4.1. Simulation results from power, pre, and in-line amplifier link.

Link Scheme	**$SFDR_2$ ($dBm \cdot Hz^{1/2}$)**	**$SFDR_3$ ($dBm \cdot Hz^{2/3}$)**	**N_{TOT} (dBm/Hz)**	**RIN_{TOT} (dB/Hz)**	**Gain (dB)**
Power Amplifier	83.04	99.1	-153.59	-139.05	-31.31
In-line Amplifier	82.07	97.81	-151.66	-137.13	-31.31
Pre-Amplifier	79.59	94.5	-146.70	-132.18	-31.31

As can be extracted from Table 4.1, the total noise spectral power density, the relative intensity noise, and the distortion terms improve when the amplifier is set before the filter (power amplification scheme) compared to the other schemes.

Moreover, although adding an amplifier to the link always increases the spectral noise density and the RIN, if it is positioned before the optical filter, some of the amplification related noises are mitigated by the filtering stage as we can see in Figure 4.7.

This fact contrasts with the pre-amplified link, where the spontaneous contributions of the amplifier are not filtered. Hence, if we are considering that the amplifier is working on linear gain regime (i.e., unsaturated, and amplifying signals with time variations shorter than the dynamic gain time constant) a lower signal degradation will be obtained if the amplifier is placed before the filter. Finally, it is shown that if power amplification cannot be provided, the in-line amplifier configuration provides a significantly good performance, since it offers an improvement of the signal with partial noise filtering, compared with the post amplification scheme.

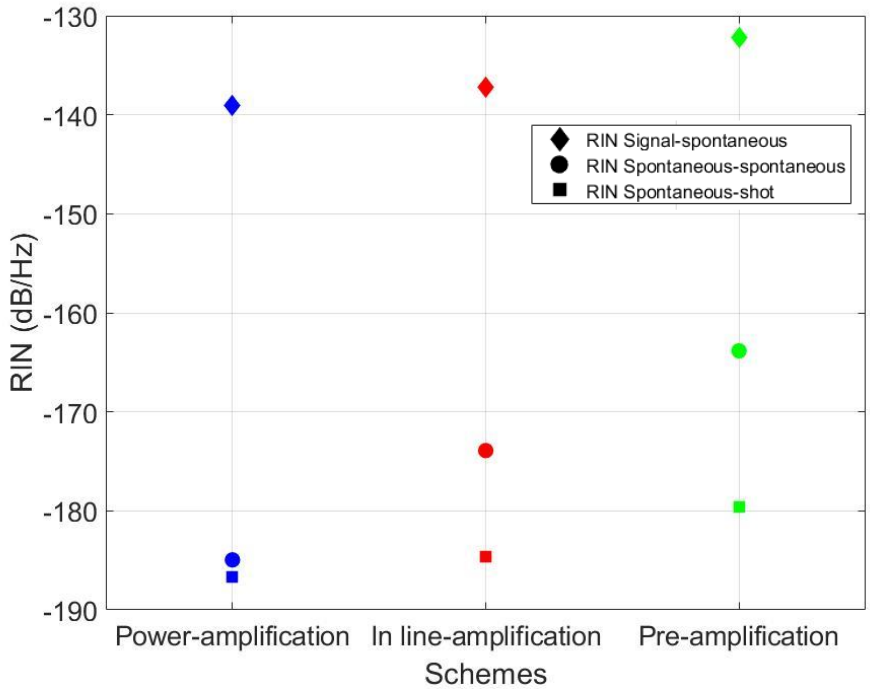

Figure 4.7. Comparison of RIN levels for each link scheme (power-amplification, inline-amplification, and pre-amplification) obtained after applying the analytical model derived in this work.

The versatility of the analytical model derived here also allows for a deep analysis of the link/system parameters on the overall system performance. As a demonstration, we have run a parametric simulation study to evaluate the evolution of the link FOMs for the power-amplified case as a function of the amplifier's gain (and therefore its noise figure) and of the input power of the optical source. Results are shown in Figure 4.8.

In the ranges considered, increasing the amplifier gain and the optical input power, a direct improvement of the link performance is obtained in terms of gain, noise figure, and distortion.
However, N_{TOT} gets slightly worse due to spontaneous emission created by the amplifier. It should be highlighted here that the optical input power of the laser should not saturate the amplifier. In this example, we have neglected gain saturation, although it can be added to the model by loading a typical saturation curve. Specifically, in terms of gain, we can see that by increasing the amplifier gain, an improvement of the MWP link gain is obtained, following a squared relation.

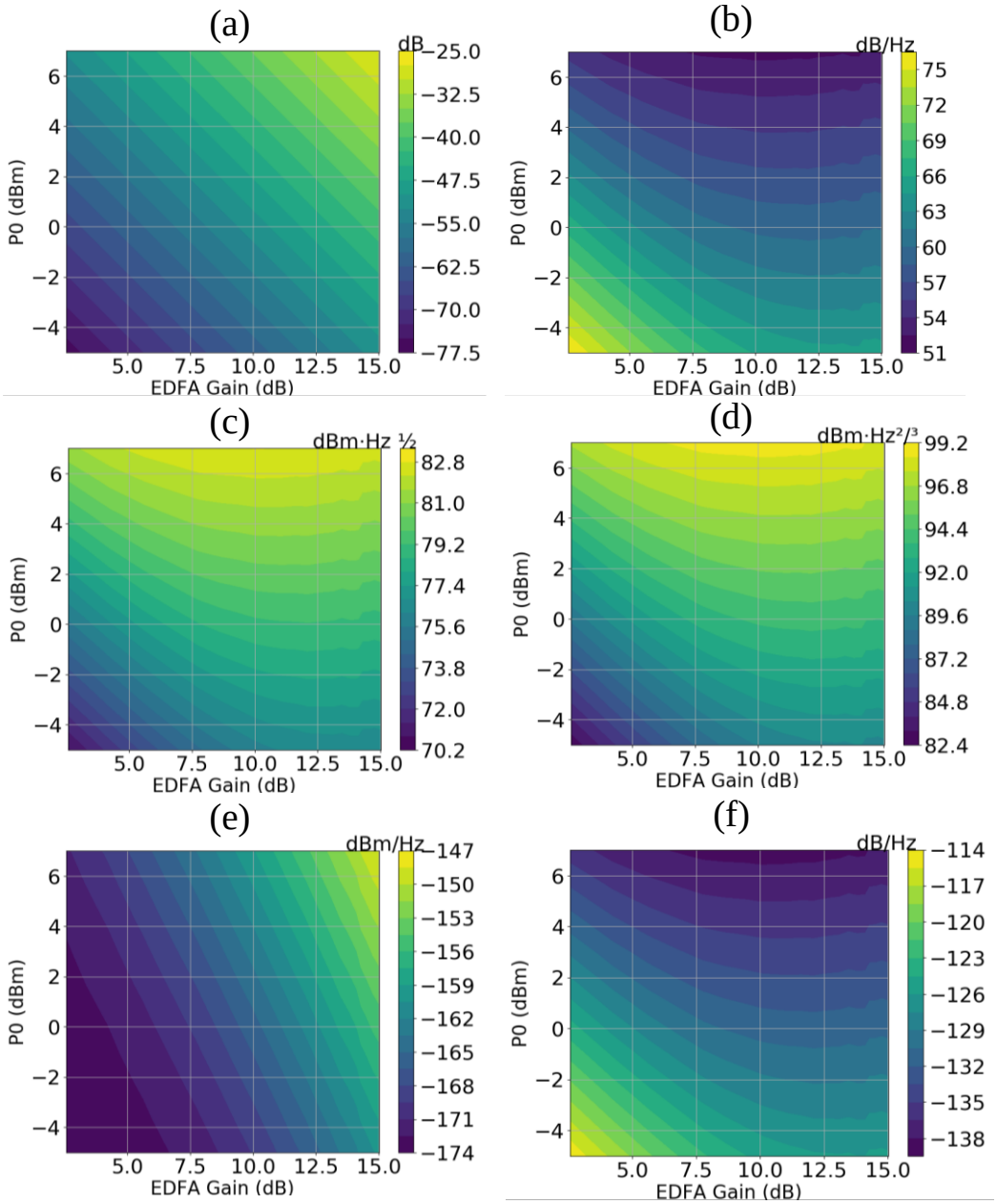

Figure 4.8. Scheme MWP power-amplification long optical fiber link (a) Gain, (b) Noise figure, (c) $SFDR_2$, (d) $SFDR_3$, (e) Total noise spectral power density, and (f) Relative intensity noise analysis.

Again, the adaptability of the model makes it applicable to flexible and reconfigurable MWP systems. As a representative example, we consider a MWP system where a reconfigurable integrated filter is inserted between the source and the detector, see Figure 4.9.

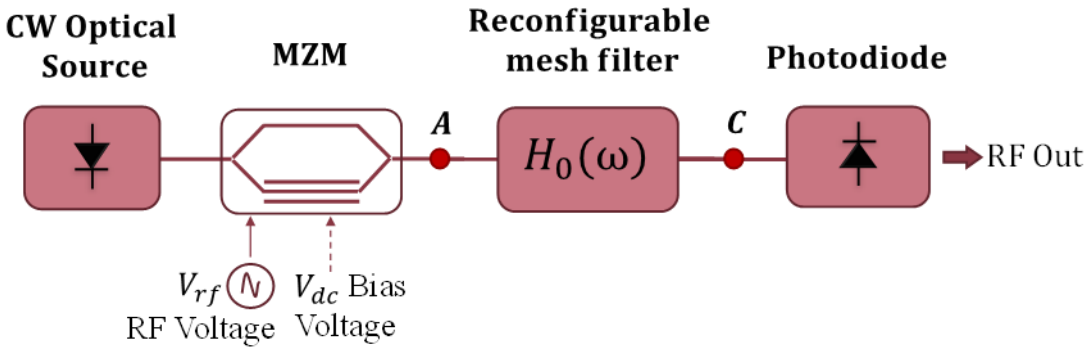

Figure 4.9. Schematic of a MWP system with a reconfigurable photonic waveguide mesh filter (point A power-amplified, and point C pre-amplified).

In this case, the optical subsystem implements a cascade MZI lattice filter of third order (Figure 4.10. (a)), which is synthesized with a programmable hexagonal optical processor (Figure 4.10. (b)) [26], [42]. Such processor is based on a two-dimensional photonic waveguide mesh created by the interconnection of programmable unit cells. Employing this type of reconfigurable optical core, we can synthetize a wide variety of photonic circuits and MWP applications [26].

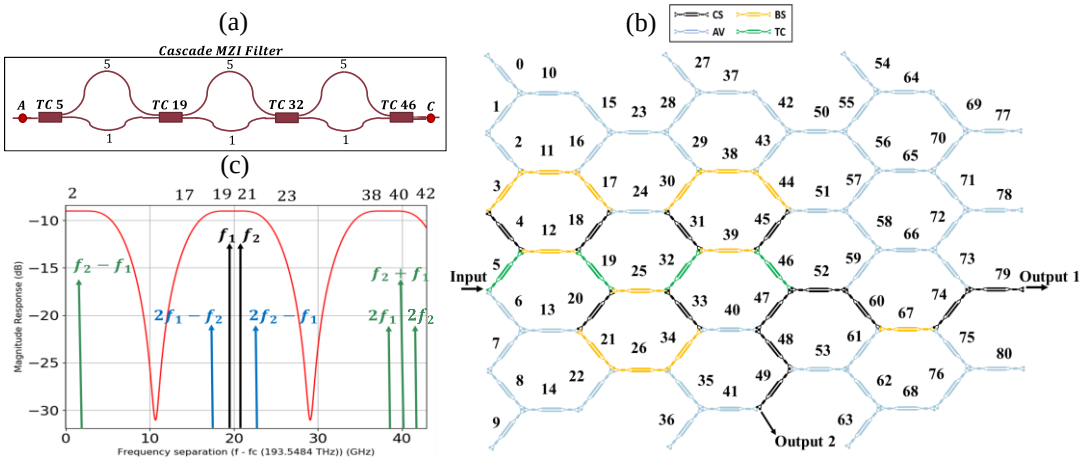

Figure 4.10. (a) Schematic of the equivalent circuit that has been synthesized with the mesh (b) Filter synthesized with the reconfigurable mesh core (c) Filter response vs. normalized frequency with the location of f1 = 19GHz, f2 = 21GHz and the distortion terms (blue: 3rd order and green: 2nd order).

We have computed the lattice filter frequency response (Figure 4.10. (c)) of the waveguide mesh arrangement by employing the analytical model derived in [42]. In the simulation, we have considered that the insertion loss of each unit cell is 0.3dB, and the insertion loss of the chip ports is 1.5dB each. After feeding the optical response to our model, we have considered two locations (point A power-amplified and point C pre-amplified (Figure 4.10. (a)) to place a semiconductor optical amplifier (Gain = 13dB and noise figure = 6dB [59]) and evaluated the behavior of the link performance.

The FOMs of a MWP system including this lattice filter and applying our model are show in Table 4.2. It is observed that the power-amplification case gives a much better noise

figure than the pre-amplification case. This is because the effect of the loss introduced by the filter is directly proportional to the variation produced in the noise of the link. We can see that, in both cases, the optical amplifier compensates the optical loss, but the overall RF Gain remains below -30dB. The analysis motivates the insertion of SOAs as high-performance building blocks in field-programmable photonic gate arrays [14] and in application specific microwave photonic integrated circuits.

Table 4.2. Analytical results from power and pre amplifier system.

Link Scheme	**$SFDR_2$ ($dBm \cdot Hz^{1/2}$)**	**$SFDR_3$ ($dBm \cdot Hz^{2/3}$)**	**N_{TOT} (dBm/Hz)**	**RIN_{TOT} (dB/Hz)**	**NF Link (dB)**	**Gain (dB)**
Power Amplifier	85.64	100.50	-159.50	-140.96	49.45	-35.01
Pre-Amplifier	80.23	93.28	-148.68	-130.19	60.27	-35.01

Finally, we ran a parametric analysis of the power-amplification scheme, Figure 4.11, where we can observe a similar trend to the one shown for the optical fiber link.

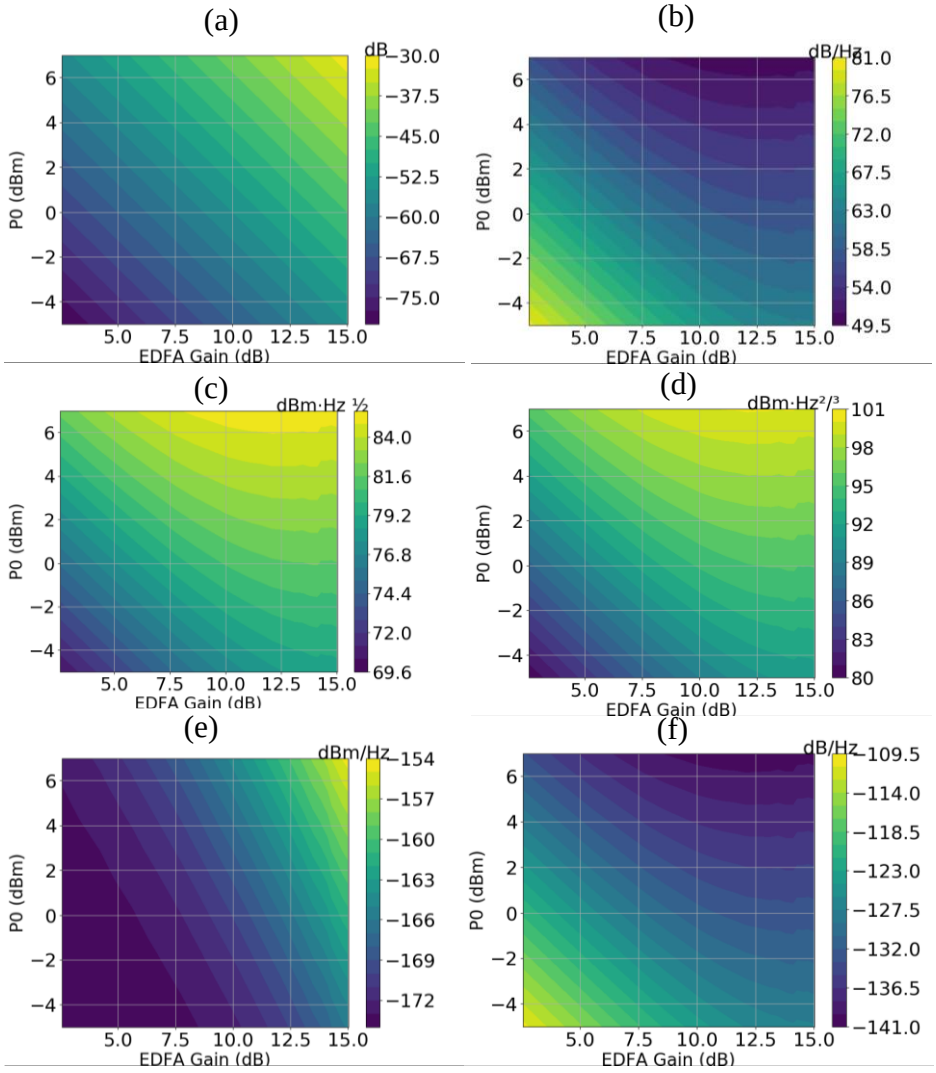

Figure 4.11. Power-amplification scheme MWP system with a reconfigurable photonic waveguide mesh filter (a) Gain, (b) Noise figure, (c)$SFDR_2$, (d) $SFDR_3$, (e) Total noise spectral power density and (f) Relative intensity noise analysis.

Now we can show another representative example, where we consider a MWP integrated system with a reconfigurable filter inserted between the source and the PD. In this case, the optical subsystem implements a coupled resonator optical waveguide filter in transmission, which is synthesized with a programmable hexagonal optical processor (Figure 4.12. (a), (b)) [14], [17]. Such processor is based on a two-dimensional photonic waveguide mesh created by the interconnection of PUCs. Employing this type of reconfigurable optical core, we can synthesize a wide variety of photonic circuits and MWP applications [14].

We have computed the CROW filter frequency response (Figure 4.12. (c)) by employing the analytical model derived in [42]. After feeding the optical response to our model, we have considered two locations (A power-amplified and C pre-amplified, following the scheme of Figure 4.9) to place a semiconductor optical amplifier (Gain = 13dB and Noise Figure = 6dB [59]) and evaluated the behavior of the link performance.

The results of the FOM of a MWP system including this CROW filter and applying our model are shown in Table 4.3. It is observed that the power-amplification case gives a much better noise figure than the pre-amplification case. This is because the effect of the loss introduced by the filter is directly proportional to the variation produced in the noise of the link. Thus, it motivates again the insertion of SOAs as high-performance building blocks (BB) to enable system amplification [14].

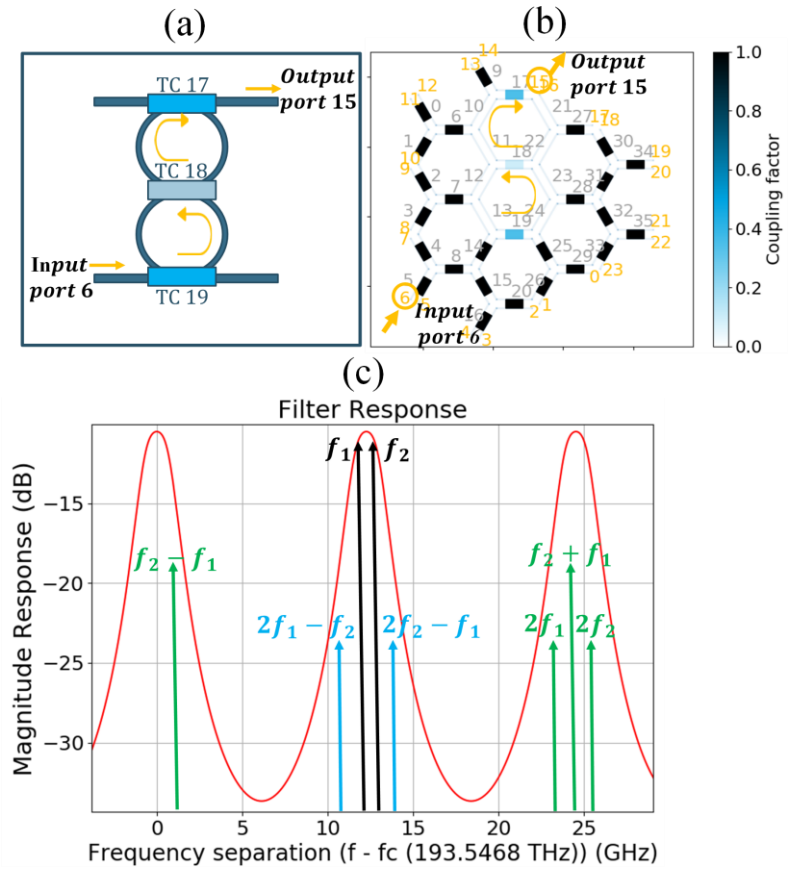

Figure 4.12. (a) Schematic of the equivalent circuit that has been synthesized with the mesh (b) Filter synthesized with the reconfigurable mesh core (c) Filter response vs. normalized frequency with the location of f1, f2 and the distortion terms (blue: 3rd order and green: 2nd order).

Then, we ran a parametric analysis (Figure 4.13), where one can observe a similar trend to the one shown before.

Table 4.3. Simulation results from passive link and power and pre amplifier link with a real (lossy) filter.

	MWP Passive Link	**MWP Power-Amplified Link**	**MWP Pre-Amplified Link**
Link Gain (dB)	-46.73	-20.73	-20.73
NF Link (dB)	49.5	37.28	53.02
RIN_{TOT} (dB/Hz)	-145.15	-157.37	-141.63
N_{TOT} (dBm/Hz)	-171.21	-157.43	-141.68
$SFDR_2$ (dBm·$Hz^{1/2}$)	83.41	89.51	81.64
$SFDR_3$ (dBm·$Hz^{2/3}$)	103.69	111.84	101.34

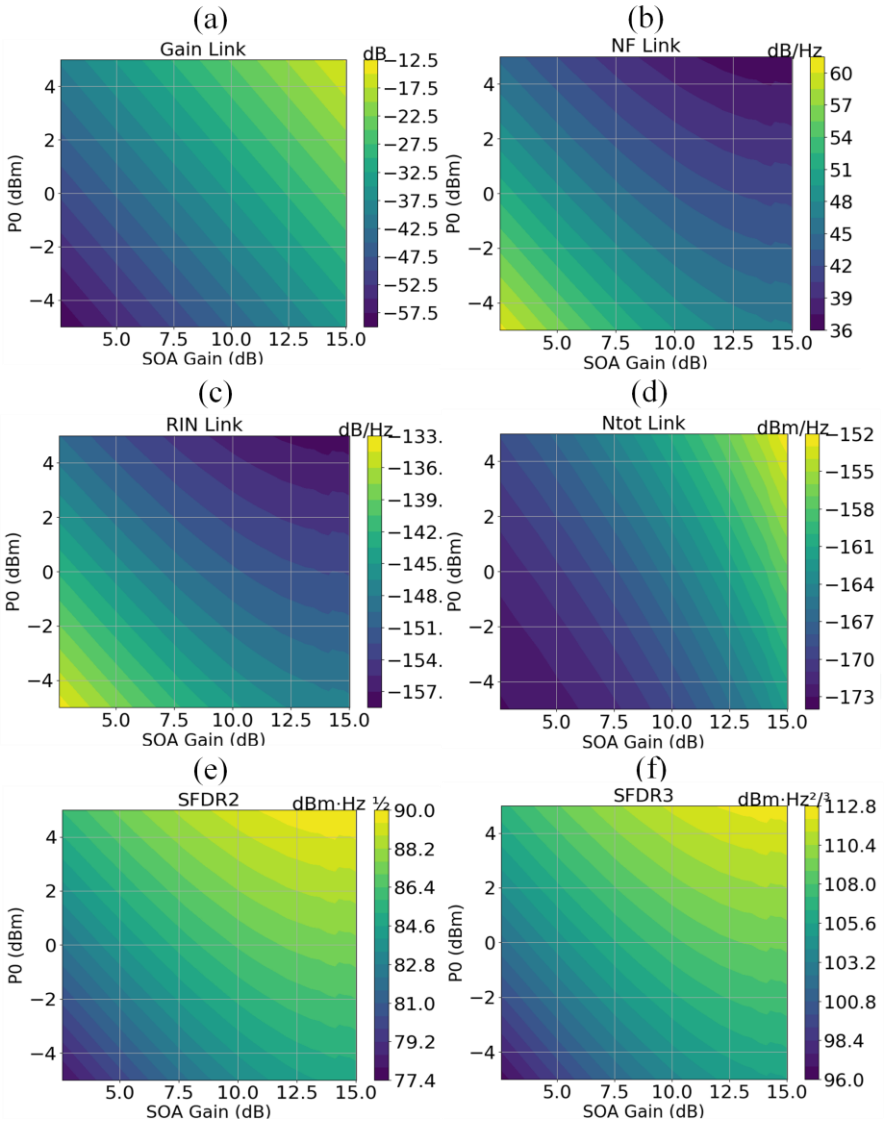

Figure 4.13. MWP Power-amplification link gain, NF, RIN, N_{tot}, $SFDR_2$, and $SFDR_3$ analysis.

4.2.2. I-Q Modulation with heterodyne coherent detection derivation

In this section, we are going to develop the MWP link model for a I-Q modulation and balanced detection. As can be appreciated in Figure 4.14, the coherent heterodyne MWP system with arbitrary filtering and amplifying stages is composed of five main blocks: An input Continuous Wavelength (CW) laser, the I-Q modulator, the arbitrary filtered and amplified chain, the local oscillator and the balanced detection stage. We briefly describe each one of them in the following paragraphs.

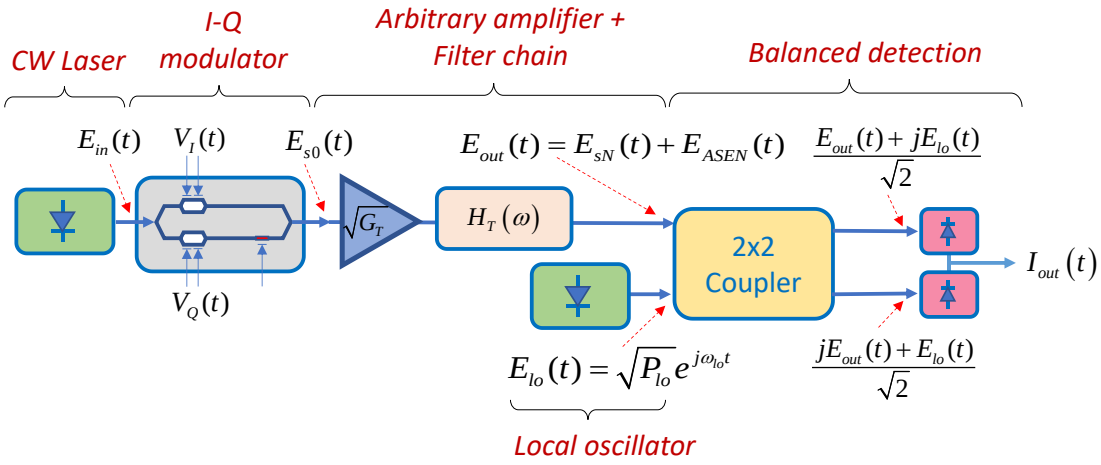

Figure 4.14. Coherent heterodyne MWP system with arbitrary filtering and amplifying stages layout under consideration.

The first stage is the continuous wavelength laser which provides the input optical field to the system, defined as Eq. (4.8). Since we are dealing with a coherent detection system, we choose an I-Q modulator as an external device to modulate the RF information onto the laser intensity provided by the CW laser. By doing so, we can independently model the FOMs for each signal component. Note that we can always obtain particular FOM expressions for the single-drive Mach-Zehnder modulator case. The I-Q modulator electric field model corresponds to a dual parallel Mach-Zehnder modulator (DPMZM) shown in Figure 4.15. and it can be derived by suitable extension of the dual-drive MZM device presented in [52]:

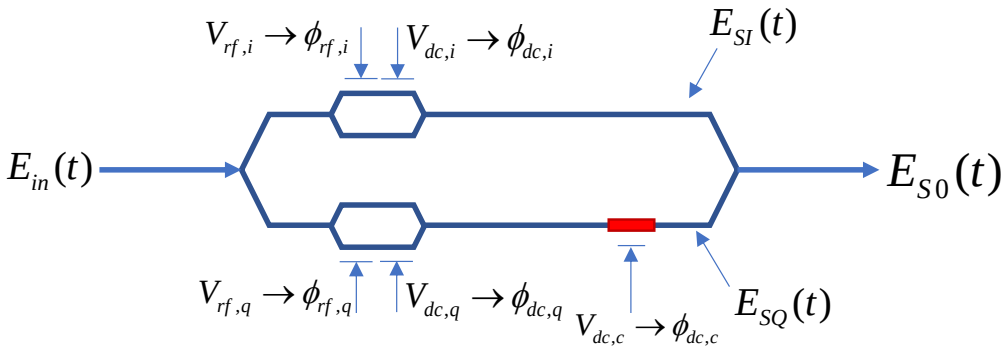

Figure 4.15. Internal layout and signals (voltage and associated phase shift) in the Dual Parallel Mach-Zehnder Modulator considered in this work for I-Q modulation. Each arm contains an independent Mach Zehnder modulator and the lower arm includes an additional phase shift stage to provide the required π/2 delay between the in-phase and quadrature components.

Referring to Figure 4.15, we consider the practical case where in-phase and quadrature dc bias values are equal $\Phi_{dc,i} = \Phi_{dc,q} = \Phi_{dc} = \pi V_{dc}/V_\pi$ and $\Phi_{dc,c} = \pi V_{dc,c}/V_\pi = \pi/2$. In these

expressions, V_{dc} is the DC voltage applied to the modulator ports and V_π is the voltage required to achieve a half wave phase shift. The input in-phase RF signal is composed of two voltage tones with equal amplitudes $V_{rf,i}$ ($\Phi_{rf,i} = \pi V_{rf,i}/V\pi$ placed at angular frequencies Ω_1 and Ω_2, while the quadrature RF signal is also composed of two tones with equal amplitudes $V_{rf,q}$ ($\Phi_{rf,q} = \pi V_{rf,q}/V_\pi$) again placed at angular frequencies Ω_1 and Ω_2. After a lengthy but straightforward process, we arrive at the following expression for the output field from the I-Q modulator.

$$E_{s0}(t) = \frac{j}{2}\sqrt{P_{in}\alpha_{DPMZM}}\, e^{j\omega_0 t}\left[\sum_{n=-\infty}^{\infty}\sum_{m=-\infty}^{\infty} B_{n,m}\left\{J_n\left(\frac{\phi_{rf,i}}{2}\right)J_m\left(\frac{\phi_{rf,i}}{2}\right) + jJ_n\left(\frac{\phi_{rf,q}}{2}\right)J_m\left(\frac{\phi_{rf,q}}{2}\right)\right\} e^{j(n\Omega_1 + m\Omega_2)t}\right] \tag{4.63}$$

where α_{DPMZM} represents the insertion losses of the modulator, $J_n(x)$ the nth order Bessel function of the first kind, $j = \sqrt{-1}$ and the Fourier coefficients $B_{n,m}$ are given by:

$$B_{n,m,i(q)} = \left\{\frac{e^{j\frac{\phi_{dc}}{2}} - (-1)^{m+n} e^{-j\frac{\phi_{dc}}{2}}}{2j}\right\} = \begin{cases} \sin\left(\frac{\phi_{dc}}{2}\right) & m+n \ \text{ even} \\ -j\cos\left(\frac{\phi_{dc}}{2}\right) & m+n \ \text{ odd} \end{cases} \tag{4.64}$$

Then, the arbitrary amplifier-filter chain internal configuration is shown in Figure 4.16. Each stage "i" is composed of an optical amplifier given by a power gain G_i and an amplified spontaneous emission noise photon number $N_i = n_{spi}(G_i\text{-}1)$, where n_{spi} represents the population inversion of the amplifier. The second element of the block is an arbitrary filter given by its complex-valued optical field transfer function $H_i(\omega)$.

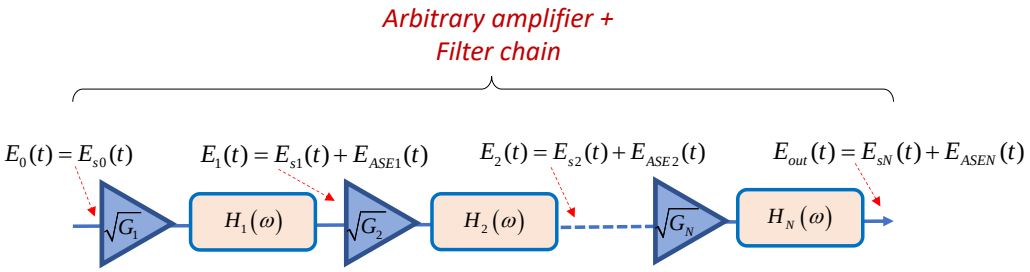

Figure 4.16. Internal configuration of the arbitrary amplifier plus filter chain. It is composed of N amplifier plus filter stages, which can be individually different.

Note that the input signal to each stage "i" is the field $E_{i-1}(t)$, which is composed of a signal part, that is the result of the input signal amplified and filtered by the i-1 previous stages and a noise component that is due to the ASE noise generated and filtered by stage "i-1" and the amplified and filtered cumulative ASE noise generated by stages "1", "2"…"i-2". The only exception is $E_0(t)$ that contains no ASE noise component. The output field from the amplifier filtered chain is labeled as $E_{out}(t)$.

Next, the local CW oscillator is placed at one of the 2 inputs of the balanced detection stage. Its purpose is to beat with $E_{out}(t)$ providing an RF up-converted signal at the overall system output. The local oscillator provides an input optical field to the balanced detector given by:

$$E_{lo}(t) = \sqrt{P_{lo}}\, e^{(j\omega_{lo}t)} \tag{4.65}$$

where P_{lo} is optical power and ω_{lo} the emitted optical frequency. We define the difference between both optical carrier frequency as intermediate optical frequency ($|\omega_o - \omega_{lo}| = \omega_{if}$), which represent the value by which the detected RF signal is up-scaled or down-scaled.

Finally, the balanced detection stage is composed by a 3dB (i.e., k = 1/2) 2x2 coupler that mixes $E_{out}(t)$ and $E_{lo}(t)$ yielding their sum and difference at its outputs. A pair of identical and equal responsivity photodetectors detect them respectively and their photocurrents subtracted. In this way, all common mode currents are suppressed to produce the output beating current $I_{out}(t)$:

$$I_{out}(t) = j\Re\left\{\left[E_{lo}E_{sN}^{*} - E_{lo}^{*}E_{sN}\right] + \left[E_{lo}E_{ASEN}^{*} - E_{lo}^{*}E_{ASEN}\right]\right\} \tag{4.66}$$

where $\Re$ represents the photodetector responsivity and * denotes the complex conjugate.

Now, using the models described in the section above for the different system blocks, assuming small-signal approximation and following a similar procedure to that reported in [60] we obtain the following values for the in-phase and quadrature photocurrents corresponding to the linear output produced in response to an input sinusoidal current at Ω_1.

$$I_{out,i(q)}(\Omega_1, t) \approx \Re\sqrt{P_{in}P_{lo}G\alpha_{DPMZM}}\left(\frac{\phi_{rf,i(q)}}{4}\right)\cos\left(\frac{\phi_{dc}}{2}\right)\left|H\left(\omega_o + \Omega_1\right)\right|\sin\left[\left(\omega_{if} + \Omega_1\right)t + \vartheta_H\right] \tag{4.67}$$

where:

$$G = \prod_{k=1}^{N} G_k \tag{4.68}$$

$$H(\omega) = \prod_{k=1}^{N} H_k(\omega) \tag{4.69}$$

H(ω) represents the overall system transfer function (including losses) and θ_H is a phase factor. From Eqs. (4.67), (4.68), and (4.69) it is straightforward to compute the corresponding RF power offered to a load resistor R_{out}:

$$P_{RF(out),i(q)}(\Omega_1) = \frac{1}{T}\int_0^T I_{out,i(q)}^2(\Omega_1)R_{out}dt = \frac{\Re^2 R_{out}P_{in}P_{lo}G\alpha_{DPMZM}\phi_{rf,i}^2\left|H\left(\omega_o + \Omega_1\right)\right|^2}{32}\cos^2\left(\frac{\phi_{dc}}{2}\right) \tag{4.70}$$

Using the same procedure, we can obtain the in-phase and quadrature components of nonlinear second and third-order beating photocurrents in response to an input sinusoidal current composed of one tone at Ω_1 and another at Ω_2.

$$\begin{aligned} &I_{out,i(q)}(\Omega_1 - \Omega_2, t) \approx \\ &\approx -\Re\sqrt{P_{in}P_{lo}\alpha_{DPMZM}G}\left(\frac{\phi_{rf,i(q)}}{4}\right)^2\sin\left(\frac{\phi_{dc}}{2}\right)\left|H\left(\omega_o + \Omega_1 - \Omega_2\right)\right|\cos\left[\left(\omega_{if} + \Omega_1 - \Omega_2\right)t + \vartheta_H\right] \end{aligned} \tag{4.71}$$

$$\begin{aligned} &I_{out,i(q)}(2\Omega_1 - \Omega_2, t) \approx \\ &\approx -\Re\frac{\sqrt{P_{in}P_{lo}\alpha_{DPMZM}G}}{2}\left(\frac{\phi_{rf,i(q)}}{4}\right)^3\cos\left(\frac{\phi_{dc}}{2}\right)\left|H\left(\omega_o + 2\Omega_1 - \Omega_2\right)\right|\sin\left[\left(\omega_{if} + 2\Omega_1 - \Omega_2\right)t + \vartheta_H\right] \end{aligned} \tag{4.72}$$

It is also convenient to compute the corresponding RF powers offered to a load resistor R_{out}:

$$P_{RF_{2,i(q)}}(\Omega_1-\Omega_2)=\frac{1}{T}\int_0^T I^2_{out,i(q)}(\Omega_1-\Omega_2,t)R_{out}dt=\frac{\Re^2 P_{in}P_{lo}\alpha_{DPMZM}GR_{out}}{2}\left(\frac{\phi_{rf,i(q)}}{4}\right)^4\sin^2\left(\frac{\phi_{dc}}{2}\right)\left|H(\omega_o+\Omega_1-\Omega_2)\right|^2 \quad (4.73)$$

$$P_{RF_{3,i(q)}}(2\Omega_1-\Omega_2)=\frac{1}{T}\int_0^T I^2_{out,i(q)}(2\Omega_1-\Omega_2,t)R_{out}dt=\Re^2\frac{P_{in}P_{lo}\alpha_{DPMZM}GR_{out}}{8}\left(\frac{\phi_{rf,i(q)}}{4}\right)^6\cos^2\left(\frac{\phi_{dc}}{2}\right)\left|H(\omega_o+2\Omega_1-\Omega_2)\right|^2 \quad (4.74)$$

Focus on the ASE noise, it is a fundamental source of degradation in amplified systems. To model the electric field corresponding to a given amplifier we employ the spectral-bin technique proposed by Desurvire [58]. The noise spectrum is then given by the sum of contributions corresponding to 2M+1 adjacent spectral bands of width $\delta\omega$. For amplifier 1 this model gives:

$$E_{ASE1}(t)=\sqrt{\hbar\omega_o\delta\omega}\sum_{k=-M}^{M}\sqrt{N_1}H_1(\omega_o+k\delta\omega)e^{j\left[(\omega_o+k\delta\omega)t+\varphi_{1,k}\right]} \quad (4.75)$$

where $\hbar$ is the Planck angular constant and $\varphi_{1,k}$ represent independent random phases. For amplifier 2, the overall ASE noise field is composed of its own generated and filtered spontaneous amplified emission plus the amplified and filtered incoming ASE from the first amplifier. Thus:

$$E_{ASE2}(t)=\sqrt{\hbar\omega_o\delta\omega}\sum_{k=-M}^{M}\left[\sqrt{N_1G_2}H_1(\omega_o+k\delta\omega)H_2(\omega_o+k\delta\omega)e^{j\varphi_{1,k}}+\sqrt{N_2}H_2(\omega_o+k\delta\omega)e^{j\varphi_{2,k}}\right]e^{j\left[(\omega_o+k\delta\omega)t\right]} \quad (4.76)$$

A similar argument runs for subsequent stages so for amplifier N, the overall ASE noise field is given by:

$$E_{ASEN}(t)=\sqrt{\hbar\omega_o\delta\omega}\sum_{k=-M}^{M}H_{FANC}(\omega_o+k\delta\omega)e^{j\left[(\omega_o+k\delta\omega)t\right]} \quad (4.77)$$

$$H_{FANC}(\omega_o+k\delta\omega)=H(\omega_o+k\delta\omega)H_{ASE}(\omega_o+k\delta\omega) \quad (4.78)$$

$$H_{ASE}(\omega_o+k\delta\omega)=\sqrt{G}\left[\begin{array}{l}\dfrac{\sqrt{N_1}e^{j\varphi_{1,k}}}{\sqrt{G_1}}+\dfrac{\sqrt{N_2}e^{j\varphi_{2,k}}}{\sqrt{G_1G_2}H_1(\omega_o+k\delta\omega)}+\\ +\dfrac{\sqrt{N_3}e^{j\varphi_{3,k}}}{\sqrt{G_1G_2G_3}H_1(\omega_o+k\delta\omega)H_2(\omega_o+k\delta\omega)}+\cdots+\dfrac{\sqrt{N_N}e^{j\varphi_{N,k}}}{\sqrt{G}\prod_{k=1}^{N-1}H_k(\omega_o+k\delta\omega)}\end{array}\right] \quad (4.79)$$

ASE leads to several noise contributions after detection. In direct detection system both the signal-ASE and the ASE-ASE beat noise sources are dominant, but for balanced heterodyne detection these are, in fact, cancelled leaving the ASE-local oscillator beat noise as the relevant contribution. The ASE-lo noise field is given by:

$$I_{ASE-lo}(t)=j\Re\left[E_{lo}E^*_{ASEN}-E^*_{lo}E_{ASEN}\right]=2\Re\sqrt{\hbar\omega_o\delta\omega P_{lo}}\sum_{k=-M}^{M}\left|H_{FANC}(\omega_o+k\delta\omega)\right|\sin\left[(\omega_{if}+k\delta\omega)t+\vartheta_{H_{FANC},k}\right] \quad (4.80)$$

It is straightforward to verify that:

$$\begin{aligned}\left\langle I_{ASE-lo}(t)\right\rangle &= 0\\ \left\langle I^2_{ASE-lo}(t)\right\rangle &= 2\Re^2 R_{out}\hbar\omega_o P_{lo}\left|H\left(\omega_o\right)\right|^2 N_{eq}\left(\omega_o\right)B_{o,eq}\end{aligned} \tag{4.81}$$

where $B_{o,eq}$ is the equivalent optical bandwidth of the arbitrary filter and amplifier chain, and $N_{eq}(\omega)$ is equivalent ASE photon number parameter:

$$N_{eq}\left(\omega\right)=G\left[\frac{N_1}{G_1}+\frac{N_2}{G_1G_2\left|H_1\left(\omega_o+k\delta\omega\right)\right|^2}+\frac{N_3}{G_1G_2G_3\left|H_1\left(\omega_o+k\delta\omega\right)H_2\left(\omega_o+k\delta\omega\right)\right|^2}+\cdots\frac{N_N}{G\prod_{k=1}^{N-1}\left|H_k\left(\omega_o+k\delta\omega\right)\right|^2}\right] \tag{4.82}$$

Using Eqs. (4.80)-(4.82), one gets:

$$\sigma^2_{ASE-lo}=\left\langle I^2_{ASE-lo}(t)\right\rangle-\left\langle I_{ASE-lo}(t)\right\rangle=2\eta^2 I_N I_{lo}R_{out}\left|H\left(\omega_o\right)\right|^2 \tag{4.83}$$

where:

$$I_N=eN_{eq}\left(\omega_o\right)B_{o,eq} \tag{4.84}$$

$$I_{lo}=eP_{lo}/\hbar\omega_o \tag{4.85}$$

And η is the detector quantum efficiency and e is the electron charge. From Eqs. (4.83)-(4.85) we finally obtain the noise spectral density and its corresponding power over an electric bandwidth B_e.

$$\begin{aligned}N_{ASE-lo}\left(f\right)&=\frac{4\eta^2 I_N I_{lo}R_{out}\left|H\left(\omega_o\right)\right|^2}{B_{o,eq}}\\ N_{ASE-lo}&=\frac{4\eta^2 I_N I_{lo}R_{out}\left|H\left(\omega_o\right)\right|^2 B_e}{B_{o,eq}}\end{aligned} \tag{4.86}$$

There are three main shot noise sources due to the signal, local oscillator, and ASE. For the shot-signal noise, we have:

$$N_{shot-signal}\left(f\right)=2e\left(I_{DCs,up}+I_{DCs,down}\right)R_{out} \tag{4.87}$$

where $I_{DC,up(down)}$ represent the direct currents due to the signal in the upper and lower branches of the balanced detector. The optical field DC component at the output of the optical system is given by:

$$E_{sN,DC}(t)=\frac{j}{2}\sqrt{P_{in}\alpha_{DPMZM}G}e^{j\omega_0 t}\sin\left(\frac{\phi_{dc}}{2}\right)(1+j)H\left(\omega_o\right) \tag{4.88}$$

From Eq. (4.88):

$$I_{DCs,up} = I_{DCs,down} = \Re\left\langle \frac{\left|E_{sN,DC}(t)\right|^2}{2} \right\rangle = \frac{\Re P_{in}\alpha_{DPMZM} G}{4} \sin^2\left(\frac{\phi_{dc}}{2}\right)\left|H(\omega_o)\right|^2 \tag{4.89}$$

So, the noise spectral density and its corresponding power over an electric bandwidth Be for the shot-signal noise are given by:

$$\begin{aligned} N_{shot-signal}(f) &= e\eta I_S G\alpha_{DPMZM} \sin^2\left(\frac{\phi_{dc}}{2}\right)\left|H(\omega_o)\right|^2 R_{out} \\ N_{shot-signal} &= e\eta I_S G\alpha_{DPMZM} \sin^2\left(\frac{\phi_{dc}}{2}\right)\left|H(\omega_o)\right|^2 R_{out} B_e \end{aligned} \tag{4.90}$$

Where Intensity signal is defined as:

$$I_S = eP_{in}/\hbar\omega_o \tag{4.91}$$

Using similar arguments and recalling the lo field given by Eq. (4.65) we get the noise spectral density and its corresponding power over an electric bandwidth Be for the local oscillator shot noise:

$$\begin{aligned} N_{shot-lo}(f) &= 2e\eta I_{lo} R_{out} \\ N_{shot-lo} &= 2e\eta I_{lo} R_{out} B_e \end{aligned} \tag{4.92}$$

Finally, using Eqs. (4.77)-(4.79) we get the noise spectral density and its corresponding power over an electric bandwidth Be for the ASE shot noise:

$$\begin{aligned} N_{ASE-shot}(f) &= 2e\eta I_N M_{sp}\left|H(\omega_o)\right|^2 R_{out} \\ N_{ASE-shot} &= 2e\eta I_N M_{sp}\left|H(\omega_o)\right|^2 R_{out} B_e \end{aligned} \tag{4.93}$$

where M_{sp} is a phenomenological parameter that accounts for the number of states of polarization in the ASE noise. M_{sp} = 1 for semiconductor amplifiers and M_{sp} = 2 for fiber amplifiers in general.

Due to the use of a balanced detection configuration, all common mode noise sources usually present in direct detection systems are cancelled or greatly suppressed here. This accounts for the input thermal noise, the RIN noise, and, as mentioned before, the signal-ASE and ASE-ASE beating noises. Therefore, the overall noise is given by the contributions discussed above and together with the output thermal noise:

$$\begin{aligned} N_T(f) &= \frac{4\eta^2 I_N I_{lo} R_{out}\left|H(\omega_o)\right|^2}{B_{eq,o}} + e\eta I_S G\alpha_{DPMZM}\sin^2\left(\frac{\phi_{dc}}{2}\right)\left|H(\omega_o)\right|^2 R_{out} + 2e\eta I_{lo} R_{out} + 2e\eta I_N M_{sp}\left|H(\omega_o)\right|^2 R_{out} + k_B T \\ N_T &= \left[\frac{4\eta^2 I_N I_{lo} R_{out}\left|H(\omega_o)\right|^2}{B_{eq,o}} + e\eta I_S G\alpha_{DPMZM}\sin^2\left(\frac{\phi_{dc}}{2}\right)\left|H(\omega_o)\right|^2 R_{out} + 2e\eta I_{lo} R_{out} + 2e\eta I_N M_{sp}\left|H(\omega_o)\right|^2 R_{out} + k_B T\right] B_e \end{aligned} \tag{4.94}$$

Now, using the results derived here to find the expressions for the typical FOMs of a microwave photonics system. The RF Gain is defined as the ratio between the input RF

power ($P_{RFin}(\Omega)$) and the output RF photodetected power ($P_{RFout}(\Omega)$). Using Eq. (4.70) and taking $P_{RFin,i(q)}(\Omega) = V_{rf,i(q)}^2/(2R_{in})$:

$$G_{RF,i(q)}\left(\Omega_1\right) = \frac{\eta^2 R_{out} R_{in} I_s I_{lo} \pi^2 G \alpha_{DPMZM} \left|H\left(\omega_o + \Omega_1\right)\right|^2}{8V_\pi^2} \cos^2\left(\frac{\phi_{dc}}{2}\right) \tag{4.95}$$

Note that the RF gain is identical for both the in-phase and quadrature components.

Then, the noise figure of the MWP link is [51]:

$$NF = \frac{N_T}{G_{RF} k_B T} \tag{4.96}$$

And is given by substituting (4.94) and (4.95) into (4.96).

Finally, the link dynamic range can be evaluated through the second and third order Spurious Free Dynamic Ranges. These are given in terms of the second and third-order output intercept points respectively (OIP_2 and OIP_3) [51]:

$$SFDR_2 = \left[\frac{OIP_2}{N_T}\right]^{1/2} \tag{4.97}$$

$$SFDR_3 = \left[\frac{OIP_3}{N_T}\right]^{2/3} \tag{4.98}$$

To compute OIP2 and OIP3 we equal Eq. (4.70) to those on Eqs. (4.73) and (4.74):

$$OIP2\big|_{\Omega_1-\Omega_2,i(q)} = \frac{\Re^2 R_{out} P_{in} P_{lo} G \alpha_{DPMZM} \left|H\left(\omega_o + \Omega_1\right)\right|^4}{4\left|H\left(\omega_o + \Omega_1 - \Omega_2\right)\right|^2} \cdot \frac{\left[1+\cos\phi_{dc}\right]^2}{\left[1-\cos\phi_{dc}\right]} \tag{4.99}$$

$$OIP3\big|_{2\Omega_1-\Omega_2,i(q)} = \frac{\Re^2 R_{out} P_{in} P_{lo} G \alpha_{DPMZM} \left|H\left(\omega_o + \Omega_1\right)\right|^3 \left[1+\cos\phi_{dc}\right]}{2\left|H\left(\omega_o + 2\Omega_1 - \Omega_2\right)\right|} \tag{4.100}$$

4.2.2.1. MWP links simulation with I-Q modulation and heterodyne coherent detection

The model can be applied to MWP systems featuring considerable complexity regardless of whether the final application is focused on transmission (radio over fiber systems, 5G front-haul links…etc.) or signal processing (i.e., filtering, true-time delaying, up-conversion, beamforming…etc.). Afterward, we consider an example that is representative of a Central Office (CO) to Base-Station (BS) front-haul link in a 5G communications system as shown in Figure 4.17.

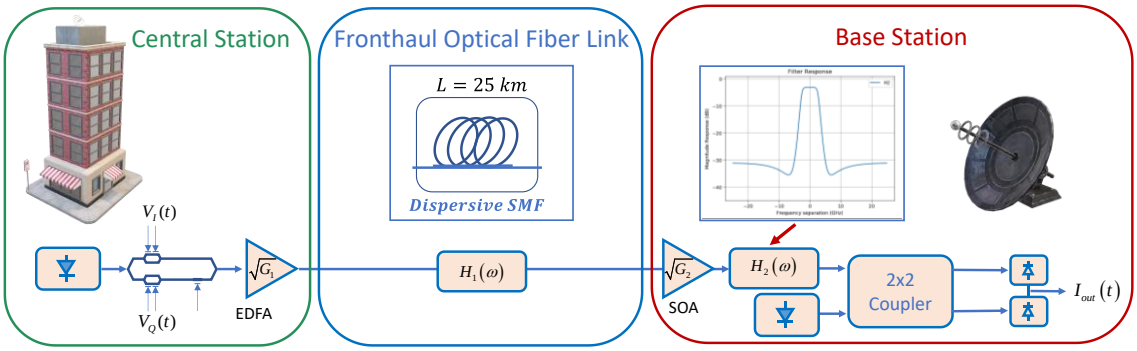

Figure 4.17. Coherent heterodyne MWP system representing a Central Office to Base Station 5G front-haul link with up-conversion.

In this case, the I-Q modulator and an Erbium-Doped Fiber Amplifier are assumed as part of the CS equipment. The front-haul connection is implemented by means of a 25km optical fiber link and the BS equipment includes an online signal processing stage implemented by a photonic chip composed of a semiconductor optical amplifier and an optical elliptic filter, followed by the heterodyne balanced detection stage. Overall, the link is composed of two amplifier and filter stages.

The model can be employed to analyze the end-to-end system performance and to investigate the effect that the variation of one or more parameters can have on the overall figures of merit. To this aim, we have considered three examples that represent different design options for the system in Figure 4.17. Example 1 represents a design where amplifiers are employed to compensate losses and low power lasers are employed both for the CS source and the local oscillator. Example 2 illustrates the case where the local oscillator laser power is increased to boost the detected RF signal, and example 3 corresponds to the case where the detected RF signal power is increased by the combined effect of a higher EDFA gain and moderate local oscillator power. The values of the main system parameters in each example are shown in Table 4.4.

Table 4.4. Main system parameters of three representative design alternatives for the front-haul link of Figure 4.17**.**

Parameters set to perform the simulation	**Example 1**	**Example 2**	**Example 3**
$\mathbf{f_1}$	1GHz	1GHz	1GHz
$\mathbf{f_2}$	1.2GHz	1.2GHz	1.2GHz
$\mathbf{P_{in}}$	0dBm	0dBm	0dBm
$\mathbf{P_{LO}}$	0dBm	13dBm	5dBm
$\mathbf{G_{EDFA}}$	13dB	13dB	25dB
$\mathbf{NF_{EDFA}}$	4dB	4dB	4dB
$\mathbf{G_{SOA}}$	9dB	9dB	9dB
$\mathbf{NF_{SOA}}$	6dB	6dB	6dB
$\boldsymbol{\alpha_{mzm}}$	4dB	4dB	4dB

The model renders the values for the main figures of merit of each example according to equations (4.95)-(4.100) with the proper parameter value substitution. It also provides useful information that can be visually represented in Figure 4.18.

Then, Table 4.5. shows the results corresponding to the noise sources for each of the three examples.

Table 4.5. Numeric values of noise densities of different sources for the three examples considered in Table 4.4

Noise densities	Example 1	Example 2	Example 3
Nshot-signal	-163.40dBm/Hz	-163.40dBm/Hz	-151.40dBm/Hz
Nase-lo	-166.11dBm/Hz	-153.11dBm/Hz	-149.75dBm/Hz
Nshot-lo	-166.98dBm/Hz	-153.98dBm/Hz	-161.99dBm/Hz
Nth-out	-173.98dBm/Hz	-173.98dBm/Hz	-173.98dBm/Hz
Nase-shot	-218.04dBm/Hz	-218.04dBm/Hz	-206.68dBm/Hz
Ntot	-160.26dBm/Hz	-150.28dBm/Hz	-147.32dBm/Hz

This allows, for example, to identify if there is a dominant noise source or if on the contrary, two or more sources need to be taken into account. For instance, and in the considered application scenario, we can observe that shot-signal noise dominates in example 1, while LO driven noise is the predominant noise in the other two cases.

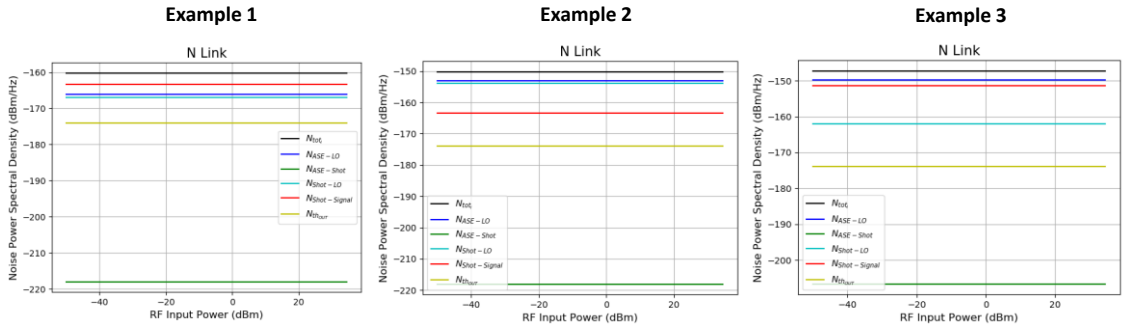

Figure 4.18. Noise densities of different sources for the three examples considered in Table 4.3.

Indeed, the fact that the end-to-end model provides an estimation of the rest of the FOMs, allows us to dispose of the complete information upon which to decide which is the best design option.

Table 4.6 shows, in form of a comparative table, the results obtained for the main figures of merit in each of the three design examples. Overall, as it can be appreciated, example 3 provides the best alternative as far as RF Gain is concerned (17dB increase) providing also a 2.7dB improvement in dynamic range ($SFDR_3$).

Table 4.6. Overall Figures of merit for the application examples described in Table 4.4.

	MWP Power-Amplified Link Example 1	MWP Power-Amplified Link Example 2	MWP Power-Amplified Link Example 3
Gain Link	-29.96dB	-16.96 dB	-12.96 dB
NF Link	43.67dB	40.65 dB	39.61 dB
Noise Spectral Density	-160.26dBm/Hz	-150.28 dBm/Hz	-147.32 dBm/Hz
$SFDR_2$	75.05dBm/$Hz^{1/2}$	76.56 dBm/$Hz^{1/2}$	77.08 dBm/$Hz^{1/2}$
$SFDR_3$	101.67 dBm/$Hz^{2/3}$	103.69 dBm/$Hz^{2/3}$	104.38 dBm/$Hz^{2/3}$

4.3. Experimental validation

Straightaway, we used the simulation tool, based on the model developed in Section 4.2.1., to predict the FOM of a MWP filtered amplifier link with intensity modulation and

direct detection. Then, we measure experimentally the link in the laboratory and compare the results.

4.3.1. MWP Links discrete measurements

Firstly, we start with the simplest example in which we used discrete components. The MWP link is shown in Figure 4.19. (a), where we used a continuous wavelength optical laser, an intensity modulator (Avanex), a discrete Multiport optical Processor (Waveshaper 4000s, Finisar), with an optical spectrum response shown in Figure 4.19. (b) and an external Photodetector (Optical Detector bandwidth 50 GHz, Finisar). Then, we compensate the losses of the link using an EDFA (23-B-FA, Amonics) in the positions A or C of Figure 4.19 (a). Later, we measure the perform of the FoM of the amplifier filtered link in the different cases (power or pre-amplifier).

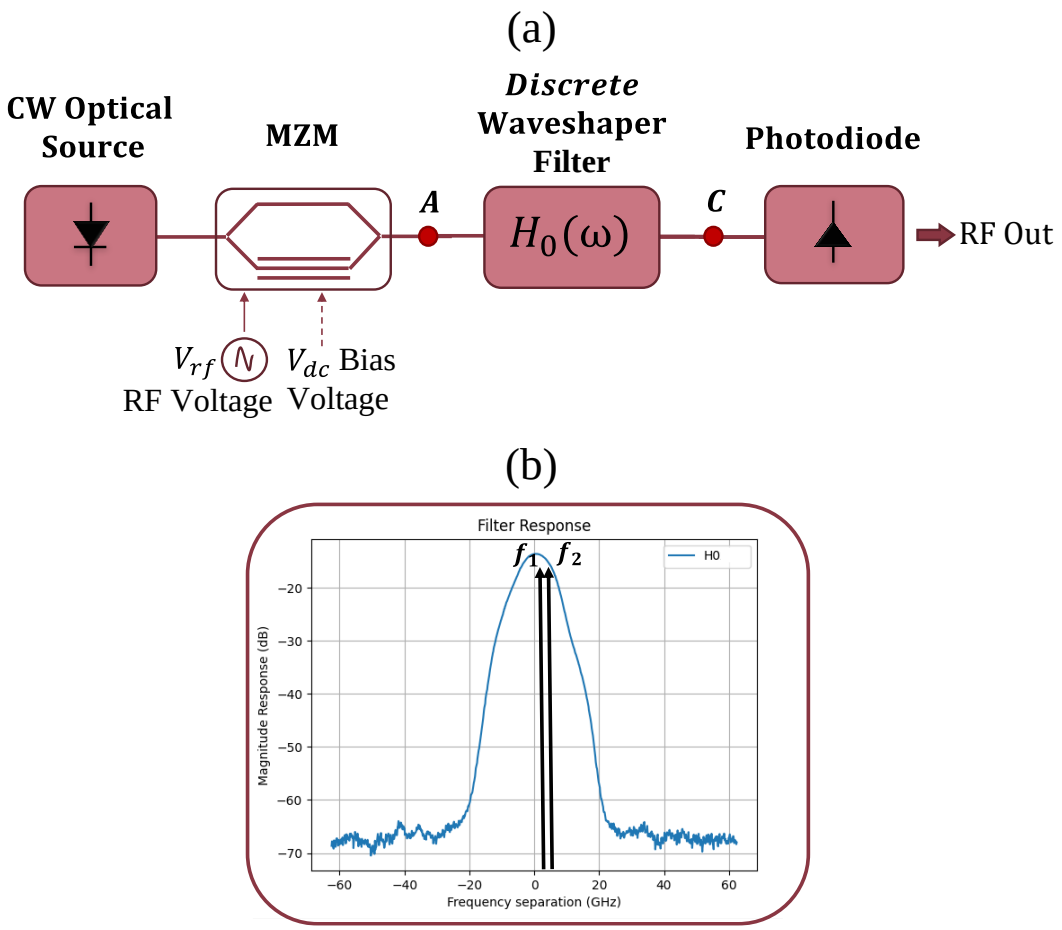

Figure 4.19. (a) MWP Link setup used to perform the discrete measurement (b) Baseband optical response $H_0(\omega)$ measured and used to set the experiment.

Thus, the measure was taken by fixing the power of the input laser to 8dBm and we set two tones at microwave frequencies of 1.5 and 1.6GHz, making sure that they are in the pass band of the filter in Figure 4.19. (b), at the input of the intensity modulator to perform the dynamic range evaluation. Moreover, the transfer function of the filter shown in Figure 4.19. (b) can we see that the insertion losses of the filter are around 12dB. The photodetector is placed at the end of the link. The following parameters have fixed values: the modulator half-way voltage V_π = 6V, quadrature MZM bias point V_{DC} = 3V, responsivity of photodetector $\Re$ = 0.6A/W, modulator insertion losses α_{mzmz} = 4.5dB and input and

output loads R_{in} = R_{OUT} = 50Ω. Finally, we adjust the optical amplifier gain and the noise figure to 14dB and 4dB respectively.

To carry out the measurement, a Vector Signal Generator (VSG) (SMW200A, Rhode & Schwarz) and a Signal and Spectrum Analyzer (FSW43, Rhode & Schwarz) were used. Then, sweeping the input power of the RF optical tones with the VSG between -8dBm and 10dBm and interpolating them, we measure the fundamental and the intermodulation distortion terms from the RF photo-detected output power using the signal spectrum analyzer. Finally, we turn off the RF signal and measure the noise floor of the link.

At the same time, we perform the simulation with the link parameters. Following the equations in Section 4.2.1 [52], [60]. The comparative results of each case, simulated vs. measured, can be observed in Figure 4.20 and Figure 4.22.

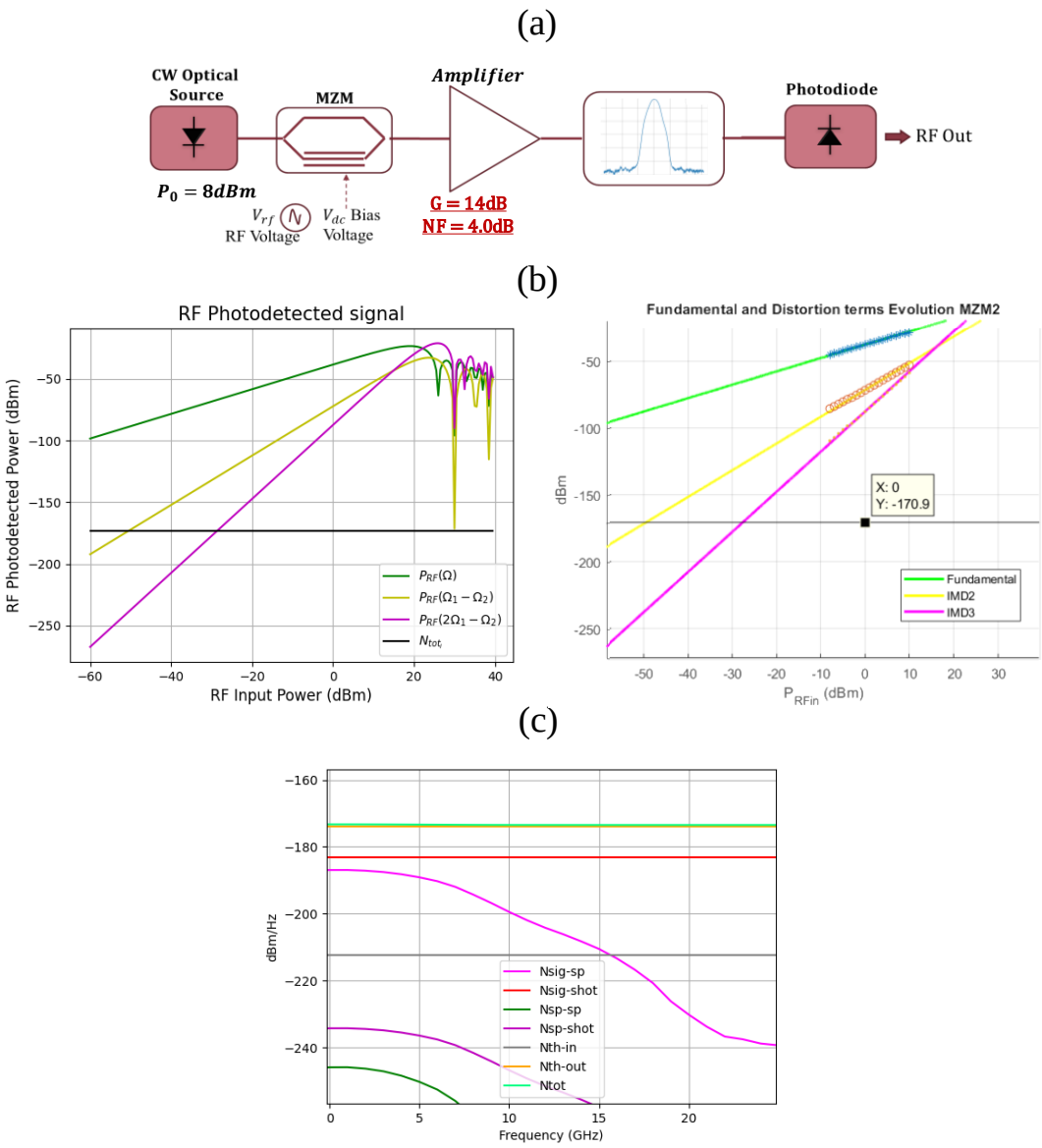

Figure 4.20. (a) MWP Link Power Amplified Filtered measurement scheme, (b) Fundamental and distortion terms simulated (left) and measured and fitted (right) obtained (c) Simulation of the evolution of each isolated noise.

Figure 4.20. (a) represents the Microwave Power-Amplifier Filtered scheme. As can be seen, in Figure 4.20. (b) the photo-detected RF fundamental, second, and third order simulation power match perfectly with ones measured. Same happens with the total noise

power spectral density simulated equal to -173.44 dBm/Hz and experimental -170.9 dBm/Hz. Note that we extract the noise spectral density generated by the optical source (equivalent to a RIN around -130dB/Hz, these values are based on typical specifications of a commercial laser) of the total noise spectral density experimentally measured. This is because, in the theoretical equations developed in the last sections, we do not model and add the relative intensity noise of the laser. In addition, we observe in Figure 4.20. (b) left, which is the simulated FoM of the link, that at high RF input power the small signal approximation cannot be used. So, the $SFDR_2$ and $SFDR_3$ get a value of 83.4616 $dB \cdot Hz^{1/2}$ and 105.3452 $dB \cdot Hz^{2/3}$ respectively.
Finally, in Figure 4.20. (c), we analyze the link noises by the simulator. It is observed that the predominant noises in the system are those that do not suffer filtering, thermal-out, and the beating of the signal field with the shot noise. Then, the third dominant noise is one generated by the beat between the signal and the amplifier ASE field and it is observed that is filtered due to the position that the amplifier is located in the link.

After all, as can we see in Figure 4.21, we obtain a RF link gain equal to -37.80dB in the simulation and experiment.

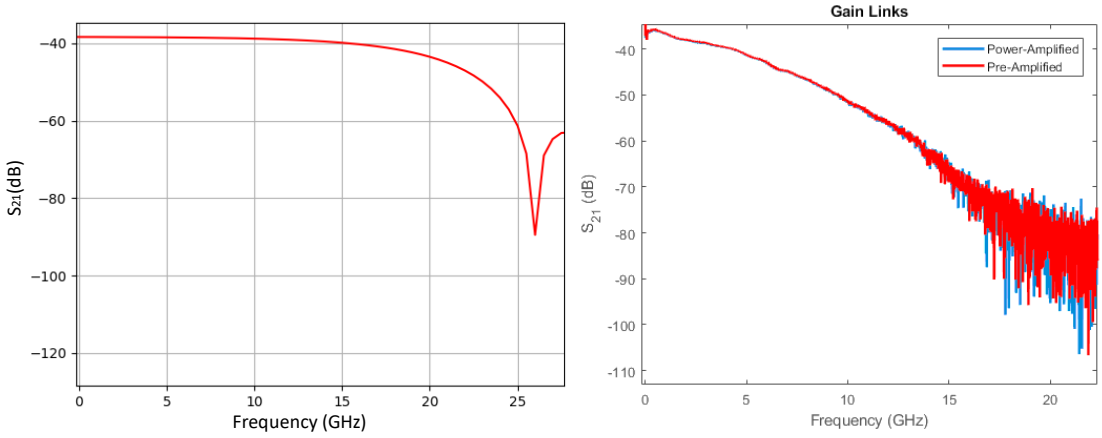

Figure 4.21. Simulated (left) and experimentally measured (right) MWP RF link gain.

Now, Figure 4.22 (a) represents the Microwave Pre-Amplifier Filtered scheme, where the amplifier is placed at the end of the MWP Link. As in the power amplifier case, here, the simulated total noise power spectral density is equal to -173.11dBm/Hz, which also, matches which ones measured in the laboratory equal to -171.40dBm/Hz. As well, as the output powers of the RF tones. Thus, obtaining an $SFDR_2$ and $SFDR_3$ of 83.4029$dB \cdot Hz^{1/2}$ and 106.0271$dB \cdot Hz^{2/3}$ respectively.

Then, analyzing all simulated link noises separately, in Figure 4.22(c), It is observed that the predominant noises in the system are thermal-out and the beating of the signal field with the shot noise again. However, the noise generated by the beat between the signal and the amplifier ASE field has increased because it is not being filtered.

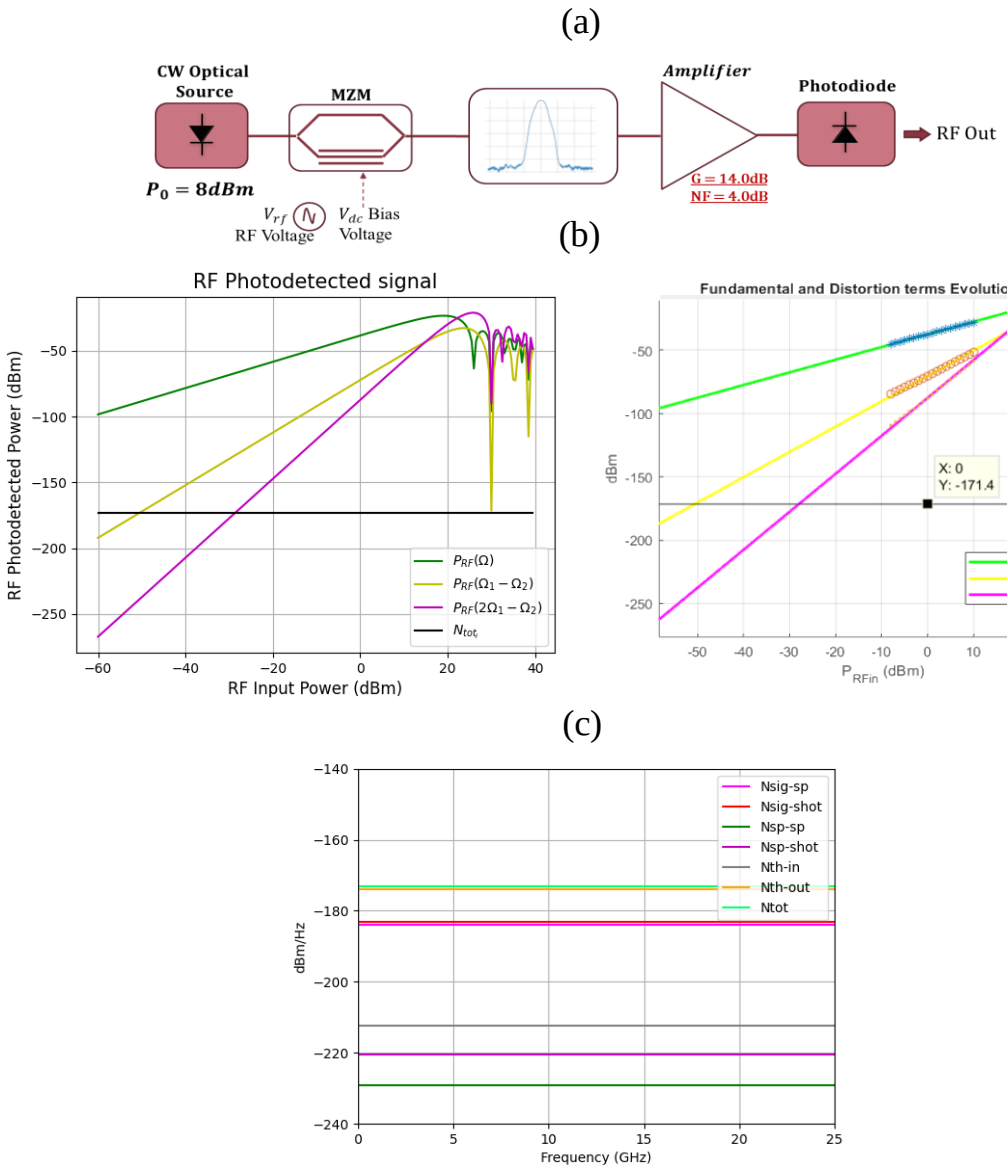

Figure 4.22. (a) MWP Link Pre Amplified Filtered measurement scheme, (b) Fundamental and distortion terms simulated (left) and measured (right) obtained, and (c) Simulation of the evolution of each isolated noise.

In conclusion, it may be remarkable that the total noise density and the MWP link FoM do not vary, as expected, depending on the position of the amplifier. It has been observed simulated and experimentally that in the example used the predominant noises do not suffer the filtering stage that the link has. Therefore, in this case, the position of the amplifier within the system could be decided without distinction.

4.3.2. MWP Integrated links mask designs on-chip

Trying to go a little further, we designed and sent to fabricate an integrated microwave photonic link for its subsequent characterization. To do this, we design the mask, with OptoDesigner, joining a Multi-Project Wafer (MPW13) run by Jeppix. Specifically, we work with Fraunhofer Heinrich-Hertz-Institut HHI foundry.

The first design of Graphic Data System (GDS) is shown in Figure 4.23 (a). It includes the building blocks, isolated, of the components that we will use to perform the MWP link. In

this way, we are going to carry out the initial characterization of its performance. Also, we can observe that the layout disposal is assigned in a cell. Then, each cell is cleaved and generates 2 chips of 4x6mm². As we have two copies of each wafer, eight chips have been delivered.

As can be seen in Figure 4.23. (b), most of the inputs and outputs optical ports have Spot Size Converters (SSCs), which change the waveguide width from a mode field diameter (MFD) of 10.4μm to 2μm (width of E200 shallow waveguide). All the devices with SSCs will be measured with a standard single mode fiber with MFD = 10.4μm. On the other hand, some devices do not have SSCs in their input/output. They will be characterized with a lensed fiber of MFD = 2.5μm. Moreover, we included in the chip a semiconductor optical amplifiers, Distributed-FeedBack (DFB) laser, Distributed Bragg Reflector (DBR) laser, photodetectors, Electro Absorption Modulators (EAM), Current-Injection Phase Modulators (PMCI), an offset of bends to characterize their losses and straight waveguide to evaluate the propagation losses. In this way, after characterizing each BB we will form an MWP link with them.

Since the isolated characterization of the BBs was not the main objective of this work. If not, it was a necessary step to know the characteristics of the devices that we later wanted to use for the integrated link. Then, in Appendix B it can be seen, in detail, all the experimental measurements that, together with the laboratory team, we carry out to characterize the isolated BBs and compare them with the design manual specifications. In general, we expected better performance in all the measured devices coming from a foundry and being standard devices from the foundry Process Design Kit (PDK) and it is not custom. Then, in Table 4.7, summarizes the conclusion particularized for each device.

Table 4.7. Conclusions extracted after characterizing the devices separately.

Devices HHI MPW13	**Performance**
Straight waveguides and SSC	High variability → Not trivial to give a value for the waveguide SSC insertion losses → Not possible to estimate the propagation losses and coupling losses accurately.
SOAs	Right performance and good amplification. Although, high variability → Not possible to obtain an accurate value of gain per length.
DFBs	Good performance, not high variability → Parameters are like expected but output power is lower.
DBRs	Don't work (only one worked from 6 measured) → The one measured has good parameters although the output power is lower.
PDs	All the available photodetectors were measured (16) and none worked as expected.
EAMs	All the EAM available in the chips have been measured (8) and none worked.
PCMIs	The measured PCMIs (we measured 4 PUCs with PCMIs in each arm) didn't work.

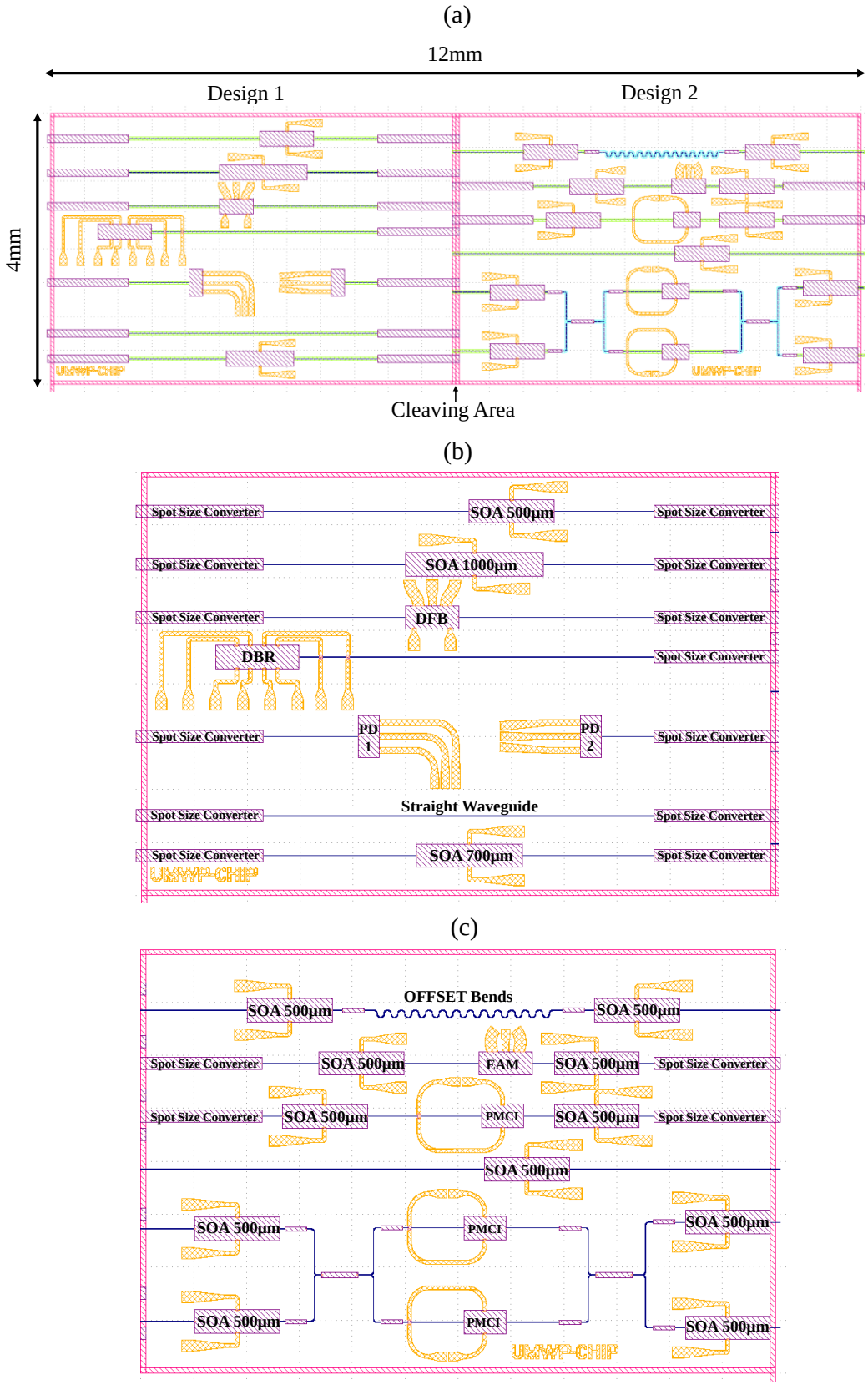

Figure 4.23. Building blocks mask layout disposal: Waveguides (dark blue layer), Metal layer (ochre), E200 and E1700 window layer (green and light blue layer), HHI BB (purple layer), BB exclusion region (red layer) (a) HHI MPW13 chip layout area, (b) Design 1 details and (c) Design 2 details.

In parallel, during the fabrication of the HHI MPW13 round, the design shown in Figure 4.24 was made. It included amplified microwave photonic links join the HHI MPW14 run. Specifically, the design has an MWP power amplifier filtered link, an MWP in-line amplifier filtered link, an MWP post amplifier filtered links, and an MWP link with two amplifiers, one before the filter and the other after. After the isolated characterization of the BBs, the objective was to measure a completely integrated MWP link.

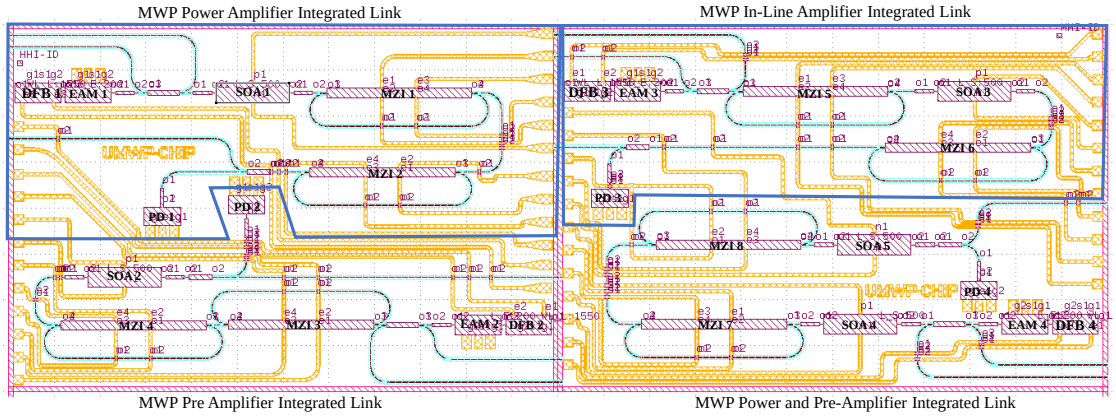

Figure 4.24. MWP Amplifier Links Mask layout for MPW HHI14.

However, the foundry told us that there was a problem with the fabrication of the devices. For example, the spot size converters experience an excess loss of around 15 dB on HHI MPW14 run. For this reason, all customer designs were re-fabricated free of charge on HHI MPW16 run. Afterward, some designs of the chips of HHI Fraunhofer MPW run 16 are shown in Figure 4.25. Again, a manufacturing problem appeared, as can be seen in Figure 4.25, and among other things, the metal deposition was not carried out correctly. Therefore, once again, a refabrication of the designs was carried out. However, this time foundry allowed us to change the layout slightly to another that seemed more optimal for the future characterization of the chip. The new layout design for HHI MPW22 run can be seen in Figure 4.26. As can you observed, we added test devices to characterize better the performance of the MZIs and the MZIs ring filter.

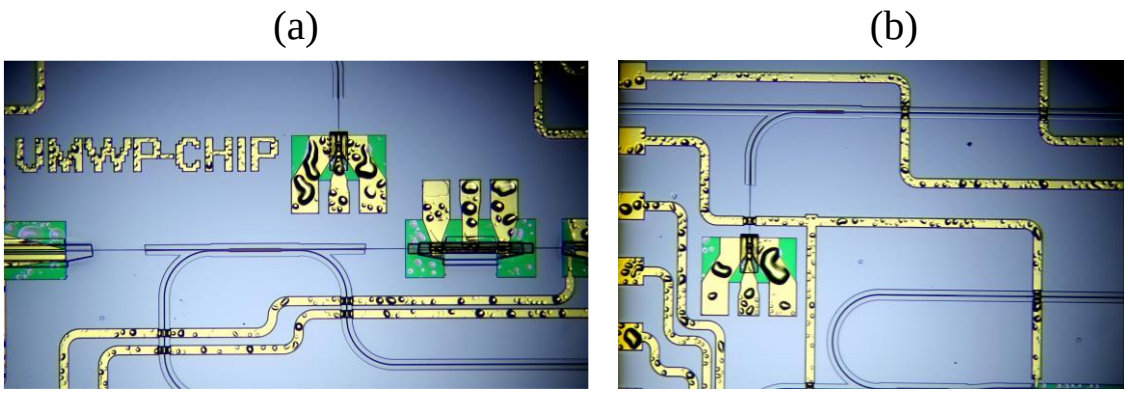

Figure 4.25. Examples of some devices, with deposition problems, fabricated in the MPW HHI16 run (a) PD4 and EAM4 (b) PD3 and DC Pads.

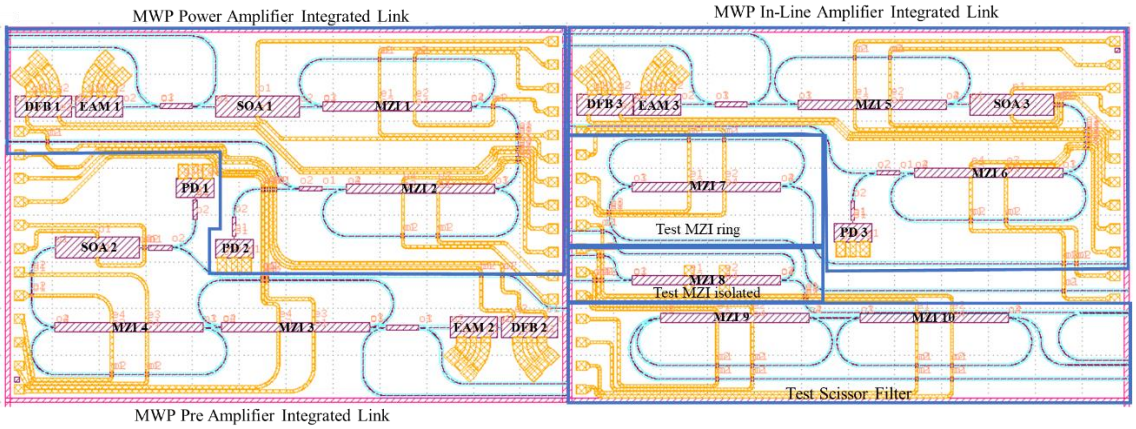

Figure 4.26. Design mask layout of HHI22 MPW run.

Finally, the foundry informs us that due to manufacturing problems the HHI MPW22 run, which was to end in March 2022, would end in September 2022. Lastly, we received the chips, but the validation report said that waveguide sidewall roughness related issues had an impact on the performance of various building blocks. As a consequence, some specifications could not have been met (e.g., DFB lasers might not operate, MZM and Electro-Optic Phase Modulator (EOPM) functionality limited (low modulation…, etc.). In addition, the waveguides (E1700) have an 8dB/cm loss and the PD responsivity was 0.1A/W. They offer us slots on HHI29 (expected delivery July 2023) to re-run their designs for half the current price of the corresponding cell size. We declined the offer. Therefore, unfortunately, the tests of the integrated link could not be carried out.

4.4. Conclusions

Microwave photonics systems have proven remarkable performance. However, their application in real-world scenarios is limited by reduced RF gains, noise figures, and system linearity. Improving RF Gain through the insertion of optical amplifiers is straightforward but impacts on the noise of the overall system. The model developed in sections 4.2.1 and 4.2.2, and applied to different examples enables the parametric study during the design and control of microwave photonic systems/links. It provides analytical expressions for a generic and simple evaluation of the main figures of merit characterizing amplified arbitrary filtered MWP links and systems and can be employed as a powerful analytical tool for prediction, optimization, evaluation, and redesign tasks.

Note as well that several noise sources are not present in the model developed in 4.2.2, which are relevant in direct detection systems. For instance, the laser relative intensity noise (RIN), the spontaneous-spontaneous and signal-spontaneous beat noises are cancelled by the balanced detector. The model is very general and accounts for MWP systems with arbitrary complexity, provided that the optical segment filtering and amplification is linear. This is the common situation in practice, where optical amplifiers are employed for signal loss mitigation and therefore no gain saturation is expected. Note that this is the case of both, integrated MWP links and discrete components-based links. It is probable that for MWP complex systems may include up to two or three filtering stages and perhaps two to three amplifiers. For these cases, our model can be readily specialised. In addition, the analytic nature of our results allows for very fast simulation and its multi-parameter nature tolerates for the fast evaluation of 2-dimensional performance maps leaving the rest of the parameters in equal conditions.

Moreover, the surge of flexible and reconfigurable MWP circuits calls for a modelling tool that can cope with the system flexibility. The model reported here enables a versatile evaluation of the position of the amplifier and its application to arbitrary systems, as long as they can be defined as a chain of passive and linear spectral subsystems.

In conclusion, we developed a model of amplified complex microwave photonic systems, which is adaptive to arbitrary system configurations. In addition, it enables the analysis and impact of each link/system parameters and the optical amplifier position. This versatile model can be employed to evaluate the performance of arbitrary MWP links and systems. In addition, we have reported an end-to-end analytic model for the computation of the FOMs of arbitrarily filtered and amplified heterodyne coherent MWP links. It is useful for evaluating the performance of complex systems where the final stage is employed for up/down converting the RF signal. We have applied the model to a specific case of a complex system representing the front-haul segment in a 5G link between the central office and the base station. The model can be applied to a wider range of cases combining fiber and photonic chip elements and thus is expected to provide a useful and fast tool to analyze them in the design stage. All this work has been disseminated in the journals publications and the contribution to congress [J.2], [J.3], and [C.2], respectively.

Chapter 5. Conclusions and future work

5.1. Conclusions

Chapter 2, titled "Fundamentals of Microwave Photonics," presents a complete overview of photonics and its applications in microwave photonic systems. Initially, we define the crucial parameters for assessing discrete microwave photonic systems performance while acknowledging their limitations, including cost, size, and power consumption. Consequently, we highlight the advantages of integrated microwave photonics as an effective means of overcoming these constraints.

The section then looks into the advantages offered by integrated photonics and provides a concise overview of various integration platforms. Furthermore, this chapter explores the potential of integrated programmable photonics, emphasizing its enhanced flexibility compared to application-specific photonic integrated circuits.

A substantial part of the chapter is dedicated to tackling a key challenge in integrated photonics: high losses. To mitigate this issue, the chapter proposes a practical solution involving the incorporation of optical amplifiers. These amplifiers are examined in detail, evaluating their impact on the overall system behaviour.

In summary, the chapter not only outlines the fundamentals of microwave photonics but also underscores the importance of integrated solutions, exploring their benefits and providing innovative approaches to enhance their performance, making it a valuable resource for readers interested in this field.

Chapter 3, titled "Scattering Matrix Generator of Complex Photonic Integrated Circuits," provides a pioneering contribution to the field by introducing a novel computational method based on the single-cell inductive approach methodology. This innovative technique has played a pivotal role in advancing our understanding of complex photonic integrated circuits.

The chapter systematically compares the newly developed computational method with two existing approaches, evaluating computational times and accuracy trade-offs across various typical application examples and circuit sizes. Through methodical analysis, it becomes evident that the inductive methodology excels, particularly in scenarios involving numerous optical paths and a high volume of feedback and feedforward loops. In such situations, the inductive methodology not only ensures superior simulation quality but also significantly reduces simulation times. This speed advantage becomes particularly crucial when dealing with complex circuits featuring a large number of optical ports.

The magnitude of this research lies in its capacity to increase our comprehension of complex systems at the single-cell level. The innovative approach not only exceeds existing methods but also opens the door to deeper scalability analysis. As a result, this chapter not only contributes to the scientific knowledge in the field but also provides a valuable framework for researchers and practitioners seeking to explore the complexities of photonic integrated circuits.

Chapter 4, titled "End-to-End Analytical Model of Amplified Links," makes a substantial contribution to the field by creating two complete models. The first model implies the development of an intensity modulation with direct detection simulator, designed to assess

the figure of merits for filtered microwave photonic link systems incorporating optical amplifiers. This mathematical derivation is then translated into a Python program and applied to both discrete and integrated realistic scenarios. These scenarios encompass a microwave photonics optical fiber link and MWP integrated systems with reconfigurable integrated filters. The analysis center on determining the optimal placement of optical amplifier gain in these setups. Unexpectedly, both simulations and experimental observations reveal that the noise components and figure of merit of the MWP link remain largely unaffected by the amplifier placement, contrary to initial beliefs. The study emphasizes that the filtering stage within the link does not significantly impact the predominant noise components, yielding unexpected results.

In parallel, following a similar methodology, the chapter also introduces a model for MWP links employing I-Q modulation and balanced detection. This configuration offers an advantage by cancelling out or suppressing common-mode noise sources typically encountered in direct detection systems. The model is applied to a specific case representing the front-haul segment in a 5G link between the central office and the base station. Three examples with varying optical input powers and amplifier gain values are evaluated, demonstrating the versatility of the model.

In summary, the developed models provide a versatile and efficient tool for analyzing a wide range of cases that incorporate both fiber and photonic chip elements. These models not only calculate optical properties but also evaluate the performance metrics of selected architectural configurations. Notable in the field, this MWP model integrates optical amplification and takes into account additional noise sources, implying a significant advancement. This enhanced model deepens our understanding and predictive capabilities in the realm of MWP systems, with far-reaching implications for applications in telecommunications, sensing, and optical signal processing.

5.2. Future work

Despite the significant progress made during the development of this project, a few opened challenges could lead to future research lines:

Regarding Chapter 3. Scattering matrix generator of complex photonic integrated circuits, could be:

- Optimize the scalability and computational time that the model requires to calculate the scattering matrix.

Improve the computational time that the model demands to calculate the scattering matrix. The time it takes to perform complex calculations or simulations impacts on the size of the problem to be solved as the user can process a larger amount of data or handle more complex tasks in the same amount of time. Systems often need to scale up to manage more complex scenarios and circuits. If computational times are not optimized, scaling can become impractical as the time required for computations grows exponentially with the size or complexity of the system. Finally, further exploration of iterative reconfiguration routines calls for ultra-efficient simulation models allowing the user to evaluate hundreds and thousands of configurations in, ideally, real time.

- Use the model for other mesh topologies than hexagonal ones (square, triangular...etc.).

The choice of mesh topology depends on the specific goals of the photonic system. For example, a square meshes might be suitable for certain types of optical filters with reduced cavity lengths. Moreover, its neighbour distances are uniform, which can be

advantageous for certain types of photonic devices. Then, triangular mesh could be preferred for reconfigurable photonic circuits with high-density waveguides, and it can potentially reduce the footprint of the photonic circuit. In addition, it could be possible to design the size of each basic unit length combining several mesh shapes. To demonstrate the suitability and comparison of different mesh topologies to specific application cases, it would be interesting to apply the inductive mathematical method that has been developed here to other types of mesh topologies.

- To consider additional non-idealities in the modeling of PUCs.

To ensure the practicality of programmable photonics circuits using waveguide mesh configurations, it is imperative to create a tool that enables us to assess their feasibility when have photonic components with fabrication deviations and non-ideal performance. Although the tool we have developed is quite complete, it could be improved by adding imperfections such as back-scattering or reflections. In this work we neglected them as are typically 30-40 dB under main signal contribution.

Then, regarding chapter 4. Ent-to-end Analytical Model of Amplified Links, could be:

- Measure amplified microwave photonic link integrated into a chip.

One of the original goals of the work was to develop and characterize an active integrated MWP link. However, the maturity of integration platforms limited the execution of this task. Despite this, technology is evolving to more robust monolithic III/V and hybrid platforms to be able to use an integrated MWP link [61]. In this way, by having the whole link on-chip we would reduce losses and greatly improve the efficiency and performance of the system.

Appendix A

A.1. Pseudocode Programming of the inductive method presented in this work.

After the definition of each scenario and the presentation of the equations that must be used for each case, we expose the following methodology to do this process sequentially (see Pseudocode A1). First, we have to define the mesh shape (variable PUC_per_col), to be able to develop a pattern and identify which scenario will be the next in each step. Moreover, we already know that this will depend on the number of ports that are interconnected with each other. In addition, for each interconnection, we must identify the ports to be connected in the n-1 order structure and the new lattice. Next, we define the number of wavelength resolution points we want (variable N_wvl_points). This variable will cause variations in the computational time of the inductive method as we have seen in the results section. Therefore, we should find a trade-off between resolution and time depending on the application that we are synthesizing. Then, we load the technology parameters of each PUC as group index, basic unit length, etc. because the method is greatly flexible, and we can calculate the value of the scattering function in different technologies. Subsequently, we define the parameters that will model each PUC, these variables can be insertion losses (variable IL), internal coupling factors (variable kappas), passive phases (variable passive_PUCs_phases), mesh configuration, whether arbitrary or not, etc. Finally, the matrix of each S_{PUCs} is calculated independently. After initializing all variables, the inductive method is performed to compute the scattering matrix of the given mesh. Assuming that the calculation is straightforward since the new scattering matrix is evaluated as a function of the matrix from the previous step and that of the new lattice. Moreover, we know that the pattern followed by the hexagonal meshes consists of five independent columns, and then the rest of the mesh can be created as a combination of these columns.

```
# variable initialization
Require: PUCs_per_column                #Mesh definition (Total NPUCs and columns)
Require: N_wvl_points                   #Wavelength resolution
load technology_parameters
Require: IL                             #Insertion losses of each PUC
Require: passive_PUCs_phases            #Passive Phases of each PUC
Require: kappas                         #Coupling factor of each PUC
Require: SPUC = compute_Scattering_PUC  #Scattering matrix of each PUC

pattern = generate_pattern_of_mesh_distribution
for column in range(pattern):
   S(n) = SPUC(1)
   S(n-1) = S(0)
   for N in range(PUCs_per_column):
    if column == 0:
        p_c0 = pattern_col_0
        for scenario in p_c0:
            if scenario == S0:
                S(n) = f(S(n-1), S(n))
            end if
            if scenario == S1:
                (n) = f(S(n-1), S(n))
            end if
            if scenario == S2:
                S(n) = f(S(n-1), S(n))
            end if
            S(n-1) = S(n)
            S(n) = SPUC(N)
        end for
    if column == 1:
        p_c1 = pattern_col_1
        for scenario in p_c1:
            if scenario == S0:
                S(n) = f(S(n-1), S(n))
            end if
            if scenario == S1:
                (n) = f(S(n-1), S(n))
            end if
            if scenario == S2:
                S(n) = f(S(n-1), S(n))
            end if
            S(n-1) = S(n)
            S(n) = SPUC(N)
        end for
    if column == 2:
        p_c2 = pattern_col_2
        for scenario in p_c2:
            if scenario == S0:
                S(n) = f(S(n-1), S(n))
            end if
            if scenario == S1:
                (n) = f(S(n-1), S(n))
            end if
            if scenario == S2:
                S(n) = f(S(n-1), S(n))
            end if
            S(n-1) = S(n)
            S(n) = SPUC(N)
        end for
    if column == 3:
        p_c3 = pattern_col_3
        for scenario in p_c3:
            if scenario == S0:
                S(n) = f(S(n-1), S(n))
            end if
            if scenario == S1:
                (n) = f(S(n-1), S(n))
            end if
            if scenario == S2:
                S(n) = f(S(n-1), S(n))
            end if
            S(n-1) = S(n)
            S(n) = SPUC(N)
        end for
    if column == 4:
        p_c4 = pattern_col_4
        for scenario in p_c4:
            if scenario == S0:
                S(n) = f(S(n-1), S(n))
            end if
            if scenario == S1:
                (n) = f(S(n-1), S(n))
            end if
            if scenario == S2:
                S(n) = f(S(n-1), S(n))
            end if
            S(n-1) = S(n)
            S(n) = SPUC(N)
        end for
   end for
end for
S = S(n)
```

Figure A.1. Programming of the inductive method presented in this work.

A.2. Non-ideal effects in mesh-based

In Chapter 3, section 3.3., we compare the experimental measurements of some structures with the responses generated by the simulation tool. Due to the hexagonal interconnection topology of the mesh, it is assumed that the ideal behaviour of the PUCs leads to the perfect performance of the programmable processor. However, in practice, there are random phase errors in the hardware mesh that have not been taken into account in the model. This causes that initially we have an extra phase shift that can be compensated for by introducing a corresponding corrective phase adjustment in any of the PUCs utilized within the synthesized circuit.

The following table shows the couplings factors and the cross phases that have been set to carry out the simulation and experimental measurement of each of the examples presented in the section.

Table A. 1. Values of couplings factors and cross phases that have been set to carry out the simulation and experimental measurement of each of the example

Structure	Simulation Coupling Factor	Simulation Cross-Phases	Experimental Coupling Factor	Experimental Cross-Phases
Finite Impulse Response (FIR) filters				
Unbalanced Mach-Zehnder Interferometer (UMZI) filter of ΔL = 2 BUL	K_1 = 0.5 (PUC 0) K_2 = 0.5 (PUC 3)	All Passives CPs = 0	K_1 = 0.6 (PUC 0) K_2 = 0.5 (PUC 3)	Passive CP = 0.25π (PUC 10) Rest of Passives CPs = 0
Unbalanced Mach-Zehnder Interferometer (UMZI) filter of ΔL = 2 BUL Tuning	K_1 = 0.5 (PUC 0) K_2 = 0.5 (PUC 3)	All Passives CPs = 0 Tuning due to 0-2π ΔCPs of PUC 10	K_1 = 0.6 (PUC 0) K_2 = 0.5 (PUC 3)	Passive CP = 0.25π (PUC 10) Rest of Passives CPs = 0 Tuning due to 0-2π ΔCPs of PUC 10
Unbalanced Mach-Zehnder Interferometer UMZI ΔL = 2 BUL lattice filter of third order	K_1 = 0.2 (PUC 3) K_2 = 0.7 (PUC 16) K_3 = 0.05 (PUC 31) K_4 = 0.9 (PUC 46)	All Passives CPs = 0	K_1 = 0.7 (PUC 3) K_2 = 0.7 (PUC 16) K_3 = 0.05 (PUC 31) K_4 = 0.9 (PUC 46)	Passive CP = -0.1π (PUC 6) Rest of Passives CPs = 0
Infinite Impulse Response (IIR) filters				
OADM filter of L = 6 BUL	K_1 = 0.15 (PUC 7) K_2 = 0.15 (PUC 6)	All Passives CPs = 0	K_1 = 0.06 (PUC 7) K_2 = 0.06 (PUC 6)	Passive CP = 1.2π (PUC 10) Rest of Passives CPs = 0
OADM filter of L = 6 BUL Tuning	K_1 = 0.15 (PUC 7) K_2 = 0.15 (PUC 6)	All Passives CPs = 0 Tuning due to 0-2π ΔCPs of PUC 10	K_1 = 0.06 (PUC 7) K_2 = 0.06 (PUC 6)	Passive CP = 1.2π (PUC 10) Rest of Passives CP = 0 Tuning due to 0-2π ΔCPs of PUC 10
Complex Filter				
OADM filter of L = 6 BUL CROW 2nd order filter	K_1 = 0.2 (PUC 20) K_2 = 0.8 (PUC 10) K_3 = 0.2 (PUC 2)	All Passives CPs = 0	K_1 = 0.29 (PUC 20) K_2 = 0.8 (PUC 10) K_3 = 0.29 (PUC 2)	Passive CP = 0.55π (PUC 11) Passive CP = 0.55π (PUC 15) Rest of Passives CPs = 0
OADM filter of L = 6 BUL SCISSOR 3rd order filter	K_1 = 0.7 (PUC 7) K_2 = 0.3 (PUC 8) K_3 = 0.3 (PUC 15) K_4 = 0.7 (PUC 16) K_5 = 0.3 (PUC 26) K_6 = 0.7 (PUC 27)	Passive CP = 0.40π (PUC 3) Passive CP = 0.80π (PUC 9) Passive CP = 1π (PUC 12) Passive CP = 1π (PUC 20) Passive CP = 0.9π (PUC 22) Passive CP = 1π (PUC 30) Rest of Passives CPs = 0	K_1 = 0.7 (PUC 7) K_2 = 0.2 (PUC 8) K_3 = 0.2 (PUC 15) K_4 = 0.7 (PUC 16) K_5 = 0.2 (PUC 26) K_6 = 0.7 (PUC 27)	Passive CP = 1.10π (PUC 3) Passive CP = 0.9π (PUC 9) Passive CP = 1.1π (PUC 22) Rest of Passives CPs = 0
Single Loaded RAMZI filter	K_1 = 0.9 (PUC 7) K_2 = 0.95 (PUC 16) K_3 = 0.7 (PUC 26)	All Passives CPs = 0	K_1 = 0.9 (PUC 7) K_2 = 0.95 (PUC 16) K_3 = 0.8 (PUC 26)	Passive CP = -0.4π (PUC 19) Rest of Passives CPs = 0
Single Loaded RAMZI lattice filter of 2nd order	K_1 = 0.9 (PUC 7) K_2 = 0.85 (PUC 16) K_3 = 0.65 (PUC 26) K_4 = 0.95 (PUC 35) K_5 = 0.7 (PUC 45)	All Passives CPs = 0	K_1 = 0.05 (PUC 7) K_2 = 0.95 (PUC 16) K_3 = 0.20 (PUC 26) K_4 = 0.85 (PUC 35) K_5 = 0.3 (PUC 45)	Passive CP = +0.15π (PUC 19) Rest of Passives CPs = 0
Simultaneity of structure synthesis				
Unbalanced Mach-Zehnder Interferometer	K_1 = 0.5 (PUC 0) K_2 = 0.5 (PUC 3)	All Passives CPs = 0	K_1 = 0.6 (PUC 0) K_2 = 0.5 (PUC 3)	Passive CP = -0.11π (PUC 11) Rest of Passives CPs = 0
Double Loaded RAMZI	K_1 = 0.5 (PUC 26) K_2 = 0.5 (PUC 35) K_3 = 0.5 (PUC 36) K_4 = 0.5 (PUC 45)	All Passives CPs = 0	K_1 = 0.8 (PUC 26) K_2 = 0.6 (PUC 35) K_3 = 0.5 (PUC 36) K_4 = 0.5 (PUC 45)	All Passives CPs = 0
Optical Ring Resonator	K_1 = 0.5 (PUC 63) K_2 = 0.5 (PUC 64)	All Passives CPs = 0	K_1 = 0.4 (PUC 63) K_2 = 0.5 (PUC 64)	Passive CP = 0.45π (PUC 67) Rest of Passives CPs = 0

Appendix B

B.1. MWP Integrated buildings blocks on-chip characterization.

Straight waveguides, spot size converters, and setup characterization

First, we started by characterizing the setup losses and the straight waveguides with SSC. The basic passive setup used for all the measurements is shown in Figure B.1. A CW tunable laser (Tunics T100R or Ando AQ4321D depending on the experiment) is used to generate the light provided to the input optical fiber after passing through a polarization controller (PC). In the setup output part, the light is collected by the output optical fiber and divided by a 50/50 optical splitter to a power meter (Greenlee 560XL) and to an Optical Spectrum Analyzer (Yokogawa AQ6370C). Both, laser and Optical Spectrum Analyzer (OSA) are connected via General Purpose Interface Bus (GPIB) to a computer and controlled by Python scripts. Afterward, we tested the losses corresponding only to the setup, not fiber-to-fiber coupling, with the power meter. The setup losses, including the section between the laser and the input optical fiber and the section between the output optical fiber and the OSA/power meter, are around 5dB at 1550nm. Then, fiber-to-fiber measurements were carried out. For that, we used cleaved standard single mode fibers (MFD@1550nm = 10.4μm) which are used for most devices (all the devices with SSCs in their input and output), and lensed standard single mode fibers (MFD@1550nm = 2.5μm) which will be used for the rest of devices without SSC. Fiber-to-fiber results are shown in Figure B.2. As it can be obtained by subtracting the setup losses (≈5dB), the fiber-to-fiber coupling losses for cleaved fibers are 1.94dB @1550nm and 3.49dB @1550nm for the lensed ones.

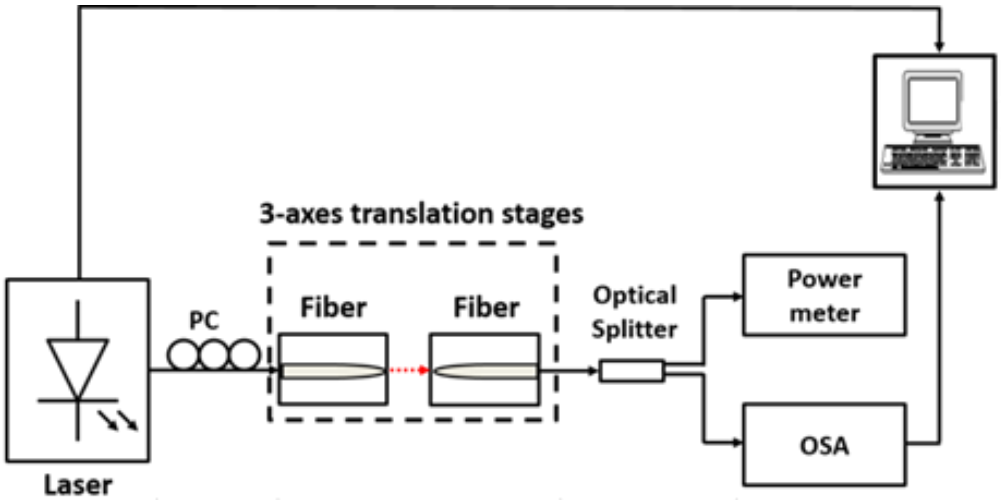

Figure B.1. The setup used for fiber-to-fiber measurement and measured setup losses.

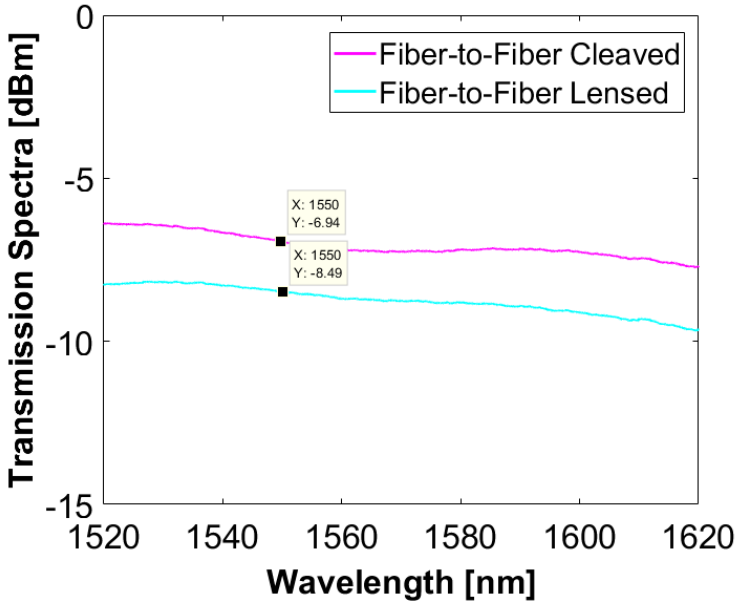

Figure B.2. Fiber-to-fiber optical transmission spectra measured for cleaved fibers and lensed fibers.

After setup characterization, the losses of the straight waveguides were measured. These measurements will be used to normalize the output power for the rest of the devices. The straight waveguides have SSC both in the input and the output, so, we characterized them with cleaved fibers. Next, Figure B.3 shows the transmission spectra of all the straight waveguides. It should be highlighted here two important issues from measurements. On one hand, the high variability in the waveguide losses (maximum output power) ranges from -9dBm@1550nm to -20dBm@1550nm (without considering the fluctuations). On the other hand, the oscillations indicate reflections and variability of their extinction ratio with the wavelength and even between different samples. Next, Table B. 1. shows the Free Spectral Range (FSR) of the fluctuations for each device as well as the cavity length corresponding to that FSR calculated from Equation (5.1) with a group index of 3.2:

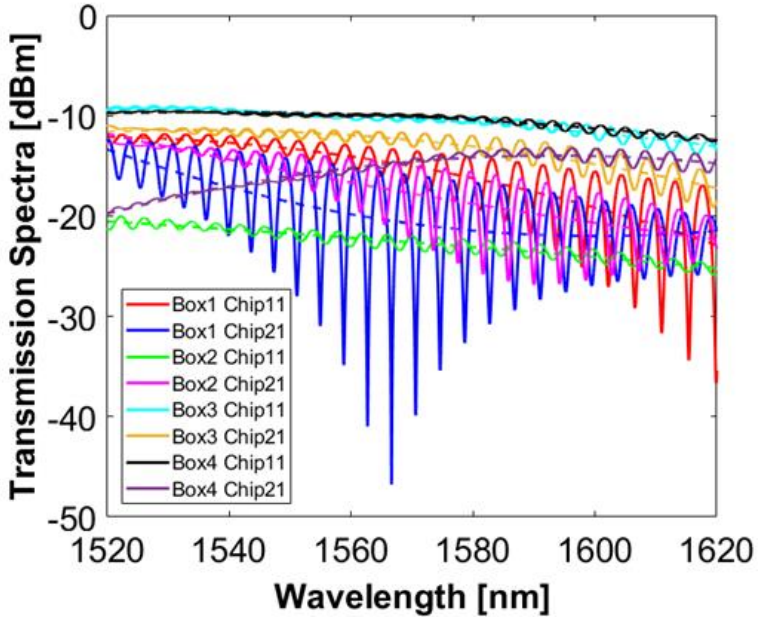

Figure B.3. Optical transmission spectra of all the straight waveguides.

Table B. 1. Experimental data extracted from the straight waveguides measurements, including fluctuations data and maximum spectrum output power.

Device	FSR	L_{cavity}	ER_{max} @ λ	Pmax @ λ
Box1 Chip11	4.4nm	170.6µm	19.78dB@1620nm	-11.8dB@1533nm
Box1 Chip21	4nm	187.7µm	31.34@1567nm	-12.33dB@1520nm
Box2 Chip11	4nm	187.7µm	1.63dB@1587nm	-20dB@1522nm
Box2 Chip21	4.2nm	178.75µm	11dB@1584nm	-12.7@1521nm
Box3 Chip11	4nm	187.7µm	1.92dB@1606nm	-8.92dB@1528nm
Box3 Chip21	4.2nm	178.75µm	3.86dB@1617nm	-10.93dB@1520nm
Box4 Chip11	4nm	187.7µm	1.14dB@1597nm	-9.45dB@1528nm
Box4 Chip21	4nm	187.7µm	1.88dB@1612nm	-13.14dB@1592nm

$$L_{cavity} = \frac{\lambda^2}{FSR \cdot n_g} \tag{5.1}$$

Moreover, the maximum extinction ratio and the corresponding wavelength are also shown in the Table B. 1. for each device. This cavity length has no correspondence with any important distance in the chip (the SSCs length is 1350µm, the length of the chip is 6mm, etc.). After talking with HHI foundry, they said that maybe some light couples into substrate modes while traveling through the waveguide which then might travel at different velocities.

The fact is that due to the high variability obtained from measurements, it is not trivial to give a value for the waveguide and SSC insertion losses. Therefore, it is not possible to estimate the propagation losses and coupling losses accurately. Anyway, we are going to do the calculations for the best case measured (Box 3 Chip11) and the data provided by HHI. On one hand, we obtain for the straight waveguide in Box 3 Chip11, that the insertion losses are IL_{WG} = 9.7dB @1550nm, and the setup losses $IL_{set\text{-}up}$ = 5dB @1550nm. On the other hand, we know from HHI design manual that the butt-coupling insertion losses are $IL_{coupling}$ = 2dB (from the validation report of 06-05-2020), and the typical propagation losses for the E200 waveguide of IL_{prop} = 2dB/cm (from the design manual 6.0 16-04-2020). Using these dates, we can make the next calculations:

From experimental measurements:

$$IL_{WG} = IL_{set-up} + 2 \cdot IL_{coupling} + IL_{\mathrm{Pr}op} \cdot L \tag{5.2}$$
$$IL_{WG} - IL_{set-up} = 2 \cdot IL_{coupling} + IL_{\mathrm{Pr}op} \cdot L = 9.7dB - 5dB = 4.7dB$$

From HHI design manual:

$$2 \cdot IL_{coupling} + IL_{\mathrm{Pr}op} \cdot L \approx 2 \cdot 2dB + 2\frac{dB}{cm} \cdot 0.6cm = 5.2dB \tag{5.3}$$

Where L is the length of the waveguide. In this case, for the best case measured, we obtain even better results than that provided by HHI. Anyway, the high variability makes it very difficult for us to draw clear conclusions.

Semiconductor Optical Amplifier characterization

Straightaway, we move on to the next building block to characterize the SOA shown in Figure B.4. We use SOAs in the design to amplify the input signal in this non-high index contrast technology. As can we observe at Figure B.4. (a)., we design three SOAs with different lengths (500µm, 700µm and 1000µm). They have two optical ports, input/output, accessible by edge-coupling through SSCs, and two electrical DC inputs to drive them, as shown in Figure B.4. (b).

(a)

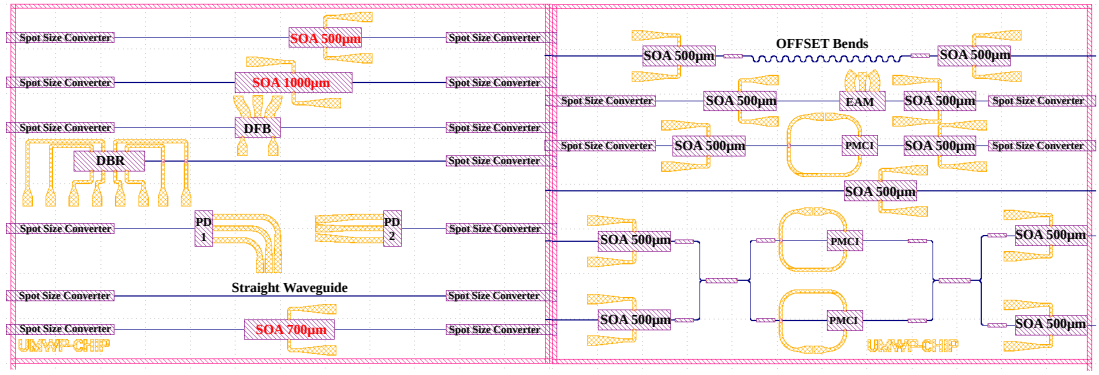

(b)

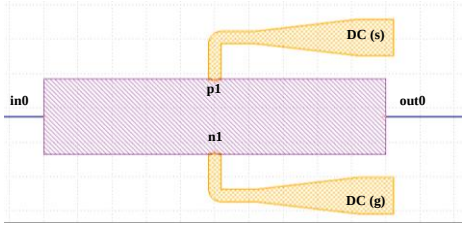

Figure B.4. (a) Disposal of SOAs (highlighted in red) in chip and (b) Mask layout of a standalone SOA showing the electrical pads and the optical ports.

HHI data provided for SOAs in the design manual version 6.0 are shown in the next Table B. 2.

Table B. 2. SOAs data provided by HHI Foundry.

	Value provided
Gain	20dB/mm @ 400mA/mm
Saturation output power	13dBm
Propagation loss when unpumped	~30 dB/mm
Emitted polarization	TE

Using the data of the gain per length provided in the design manual, for the 500µm length SOA the gain will be 10dB at 200mA, the gain for the 700µm length SOA will be 14dB at 280mA, and the gain for the 1000µm length SOA will be 20dB at 400mA. Moreover, in the HHI validation report (6th May 2020 version), they showed that the gain of a 900µm long SOA in TE is 8dB at 100mA.

For SOAs characterization, we used the setup in Figure B.5. They were driven by two DC probes directly connected to a source meter (Power supply, Keithley 2401) through two micropositioners (Microworld S725PLM/PRM). Then, the light generated by a laser (Yenista T100R) was passed through a polarization controller before being injected into the input cleaved fiber. After the chip, the light was collected by the cleaved output fiber and divided by a 50/50 optical splitter to a power meter (Greenlee 560XL) and an optical

spectrum analyzer (Yokogawa AQ6370C) with the aim of align the fibers maximizing the output power with the power meter and simultaneously measure the spectrum in the OSA.

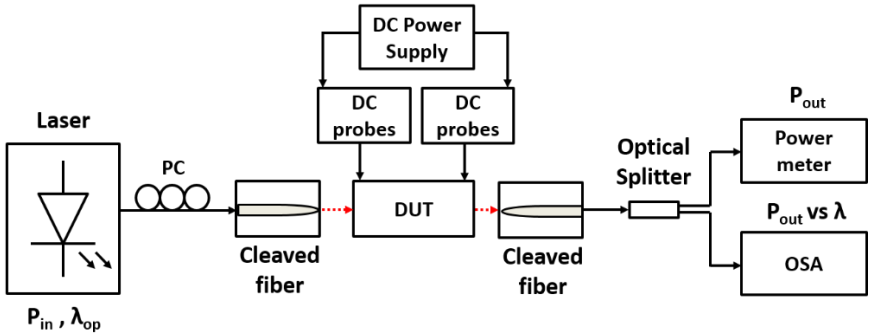

Figure B.5. Setup used for SOAs characterization.

Then, the amplified spontaneous emission regime was characterized. For that, the laser was kept turned off and the current fed to the SOAs was swept, by using a Python script. Then, the spectrum was measured, in the OSA, and saved for each current. Results for SOAs in one of the samples are shown in Figure B.6. (a). Then, Figure B.6. (b) and (c) are the ASE spectra measured and shown in the HHI Design manual respectively for a SOA sample of 500µm.

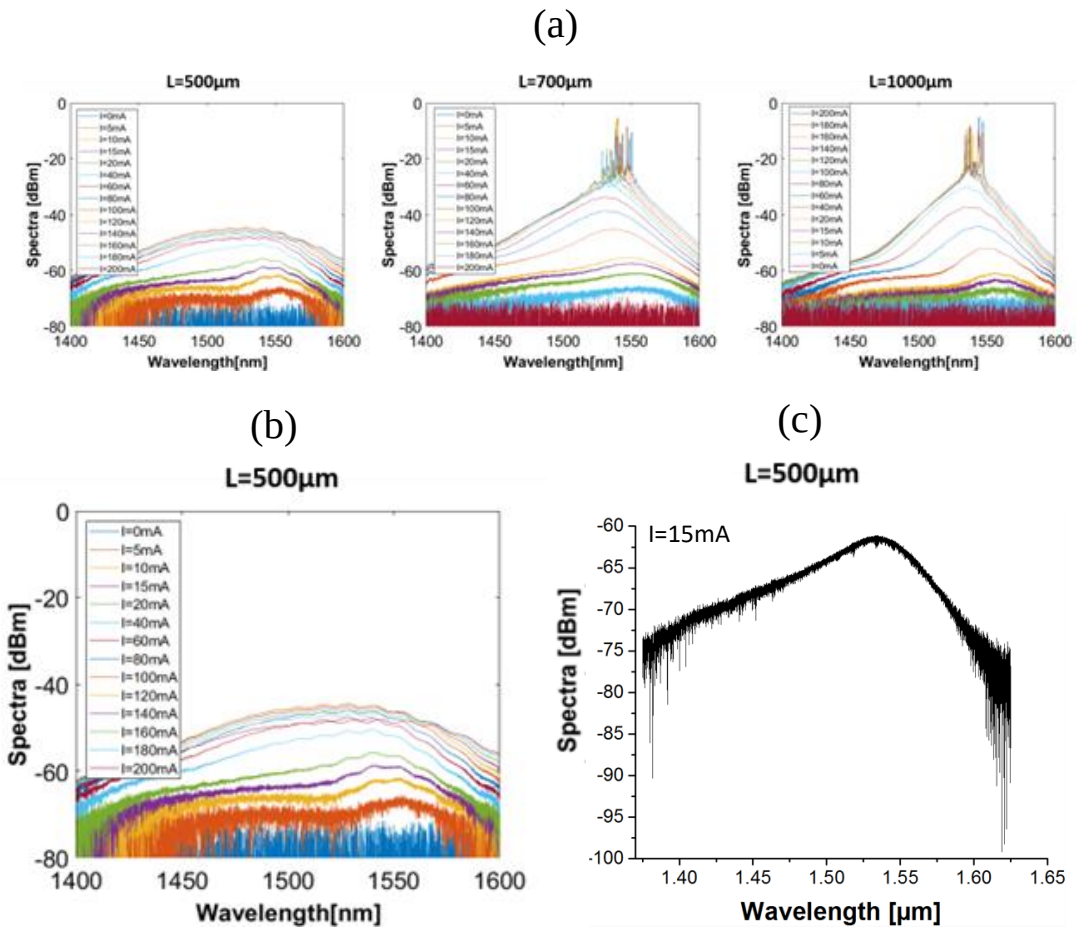

Figure B.6. (a) ASE spectra were measured for different currents for the three lengths of SOAs samples. (b) ASE spectra measured for different currents for 500µm SOA length vs. (c) ASE obtained from foundry design manual for 15mA of current and 500µm SOA length.

As we observe in Figure B.6. (b) and (c) the ASE measured fits as expected according to the manual.

After ASE regime, we measured the laser output power signal as a function of the input signal to obtain the gain. For that, we turned the laser on, and measured the output signal. As reference, we have the design manual output power versus input power curves and gain curves for a 900µm length SOA (@1540nm), as shown in Figure B.7. (a). In addition, Figure B.7. (b) shows the optical input power versus optical output power curves for a sample of SOAs. It was measured by sweeping the currents through a Python script for different optical input powers, and for each current and input power, the spectrum measured in the OSA was saved. Then, we obtained the optical input power versus optical output power curves by a post-processing of the measured spectra.

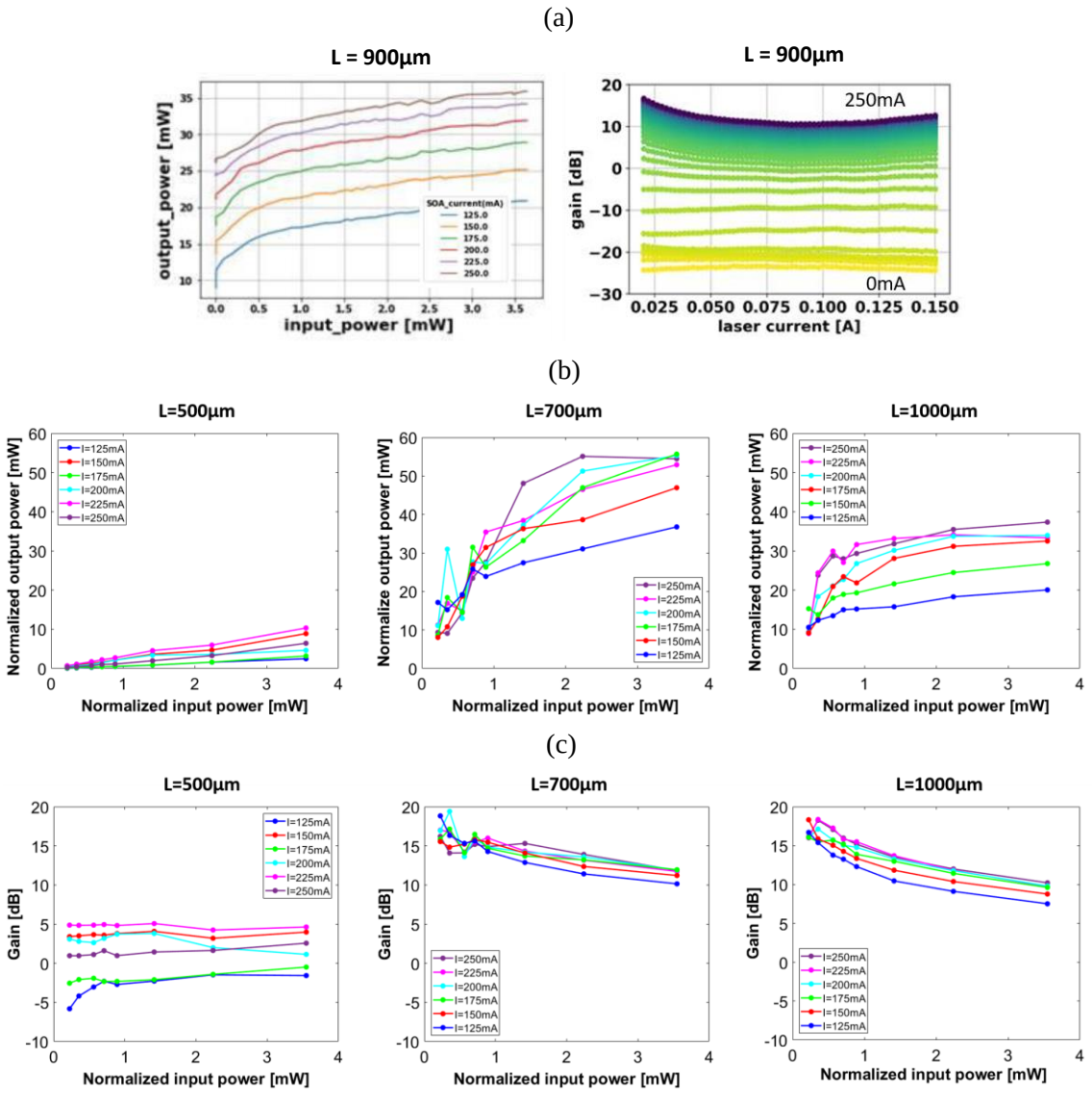

Figure B.7. (a) Experimental curves from HHI showing the output power versus input power (left) and the gain (right) curves for a 900µm length SOA. (b) Optical output power versus optical input power (c) Gain versus optical input power for SOAs with different lengths

Moreover, Figure B.7. (c) shows the gain that was obtained by subtracting the normalized input power from the normalized output power. As can be observed, the shorter SOA (L=500µm) showed a lower gain than expected and the longer SOAs (L=700µm and

L=1000µm) showed higher gains. However, no negative gain was obtained, as expected from HHI report curves (Figure B.7. (a) right), indicating the measurements were not properly carried out, probably due to the polarization somehow changing during measurement. The measurements are highly sensible to the polarization and it changes with the current changes.

The measurements were repeated for other SOAs samples. This time the optical input power was swept (instead of the current) by using a Python script for different currents (instead of different optical input powers) to avoid the polarization changes. Moreover, we obtained more points of each curve (by taking a lower optical input power step). For each input power and current, the spectrum measured in the OSA was saved. As can be observed in Figure B.8 (a) and (b), the trends of the curves are similar to than expected.

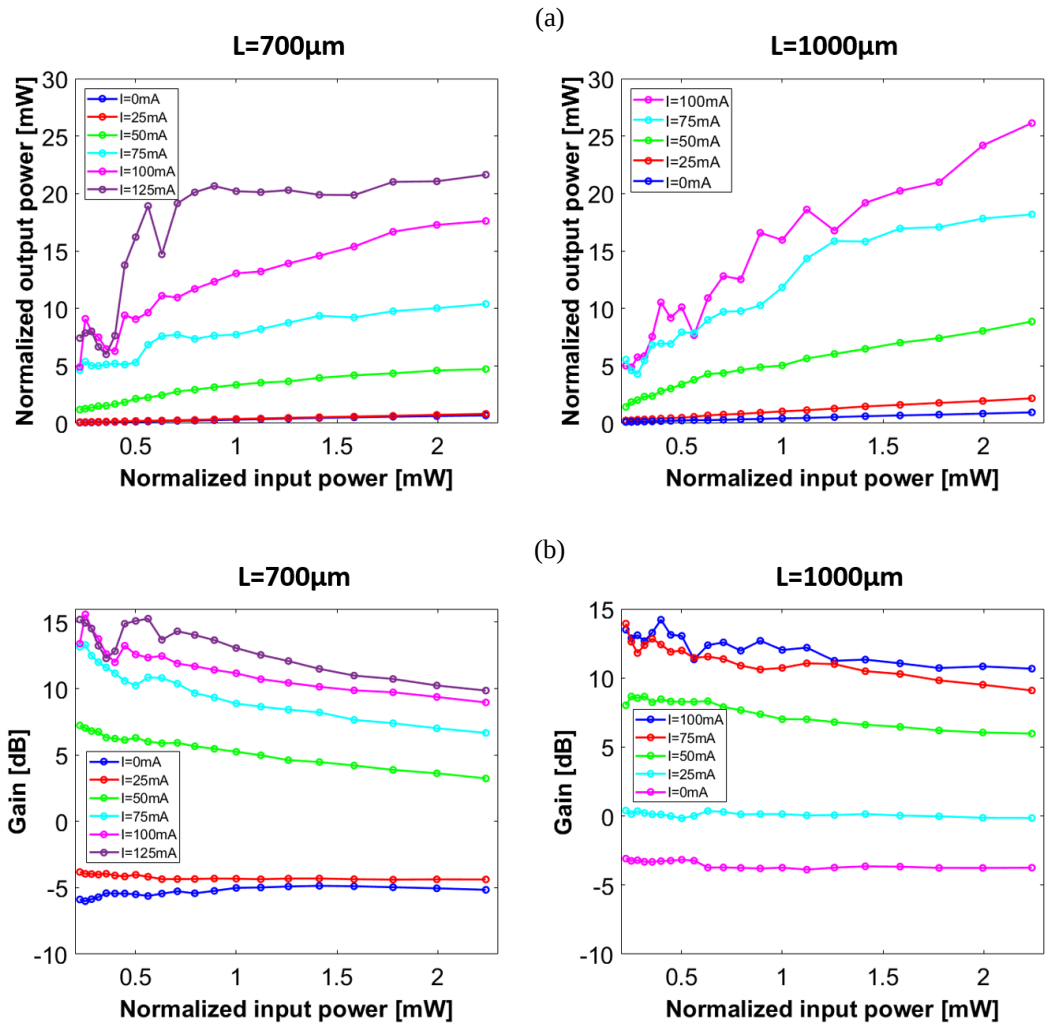

Figure B.8. (a) Optical output power versus optical input power and (b) Gain for SOAs with different lengths.

In conclusion, most of the measured SOAs worked well showing a good amplification. However, the measurements, again, show a high variability, and it is not possible to obtain an accurate value of gain per length. Next Table B. 3, shows the gains provided by HHI taking into account the data provided in the design manual (Gain = 20dB/mm @ 400mA/mm) and the validation report (Gain (L=900µm) = 8dB @100mA). Moreover, in the last column, it is shown the gain obtained experimentally by us. As mentioned, it is difficult

to obtain from our side an accurate number for the gain per length due to the high variability in the results.

Table B. 3. Gain provided by HHI and our experimental gain, as a function of the SOA length.

Length	Gain provided by HHI	Our experimental gain
L=500µm	10dB@200mA	3dB@200mA
L=700µm	14dB@280mA	14dB@250mA (Box1 Chip11) 13.5dB@125mA (Box3 Chip11)
L=900µm	8dB@100mA 18dB@360mA	--
L=1000µm	20dB@400mA	15dB@250mA (Box1 Chip11) 12.5dB@100mA (Box3 Chip11)

Distributed Feedback Laser characterization

The next device to characterize is a distributed feedback laser see Figure B.9. It is based on a Multiple-quantum-well (MQW) ridge-waveguide structure. The complex-coupled grating is defined on top of- and etched into the MQW structure. Light exits both sides of the device. The DFB laser is driving through RF electrical pads (g1, s1, g2). In addition, it contains an internal heater (pads e1, e2) to allow the designer to tune the wavelength of the output signal as can you observed in the mask layout and in the fabricated devise, Figure B.9. (b) and (c), respectively.

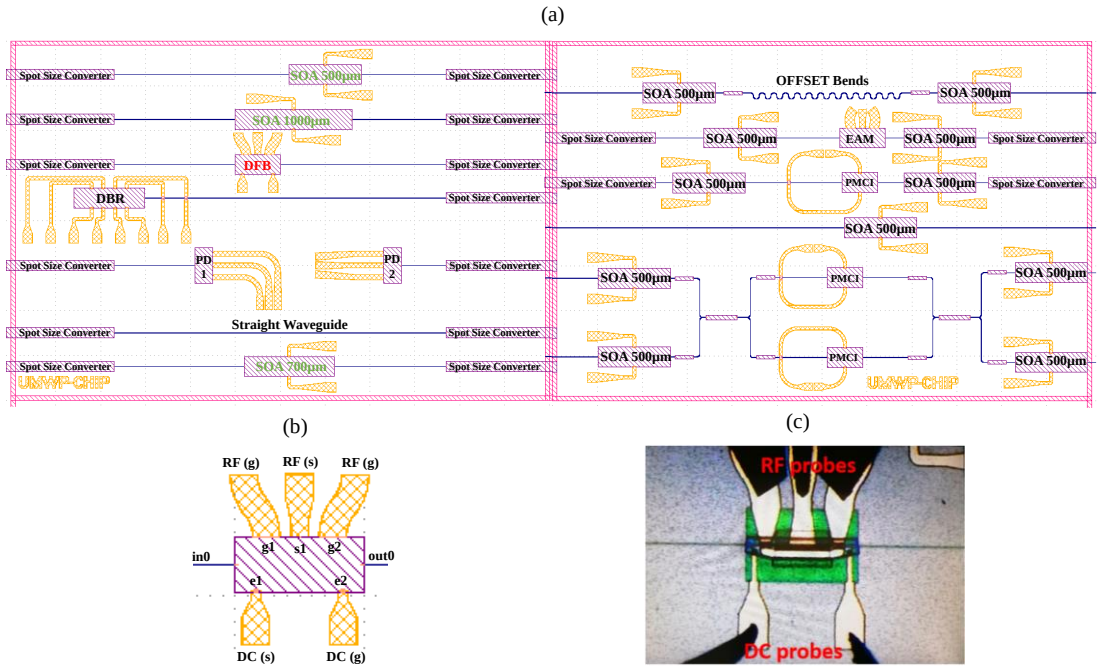

Figure B.9. (a) Disposal of DFB in the design chip (highlighted in red), (b) DFB mask layout showing the electrical pads and the optical ports, and (c) Fabricated device during the measurements.

The HHI Foundry details provided for DFBs in the design manual (version 6.0) are shown in Table B. 4. Moreover, in the validation report, they included: DFB power @50mA = 5dBm (3.162mW) and a wavelength deviation of 6nm.

Table B. 4. DFBs data provided by Fraunhofer HHI.

Parameter	Value provided
Wavelength tuning range	3nm
Side-mode suppression	>50dB
Single-sided output power	>5mW @ 150mA
Resistance heater	45Ω
Threshold current	10mA
Linewidth	5MHz
Relative intensity noise	<-140 dB/Hz

Afterward, we make the tuning and driving characterization using the setup shown in Figure B.10. Setup used for DFBs tuning and driving characterization. The driving was carried out by using a Ground-Signal-Ground (GSG) 150µm pitch RF probe (50A-GSG-150-DP from GGB Industries) while the tuning was carried out by two DC probes. In both cases, the probes were directly connected to a source meter (Power supply, Keithley 2401) through two micro-positioners (DC probes, Microworld S725PLM/PRM, and RF probes XYZ 300ML, Quarter Research and Development Inc.). The light emitted by the DFB laser is collected by the cleaved output fiber and divided by a 50/50 optical splitter to a power meter (Greenlee 560XL) and an optical spectrum analyzer (Yokogawa AQ6370C) with the aim of align the output fiber maximizing the output power with the power meter and simultaneously measure the spectrum in the OSA.

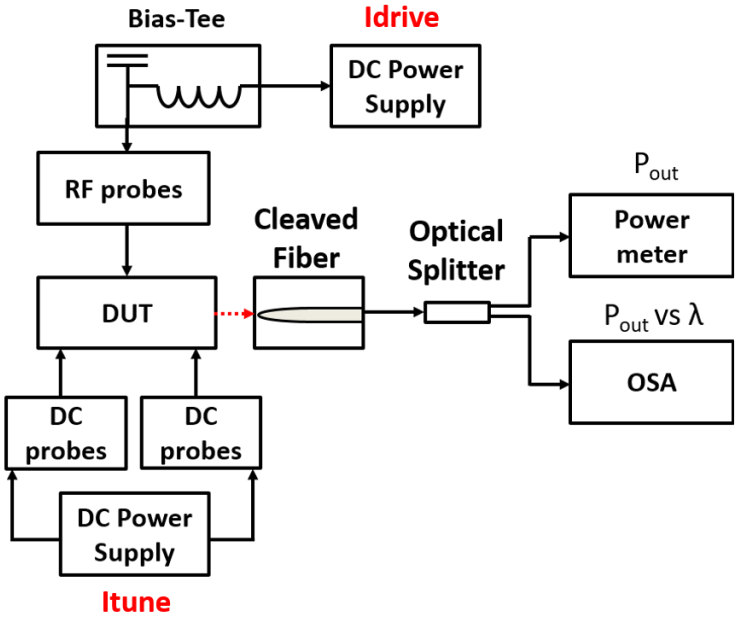

Figure B.10. Setup used for DFBs tuning and driving characterization.

Figure B.11. (a) shows the Light-Current-Voltage (LIV) curves of the DFB devices (sample Box1 Chip 11) with different wavelengths for 50°C (measurements are single-sided, i.e., only half the generated power is measured). We obtained the voltage-current curves by sweeping the tuning current (I_{tune}) using a Python script. The tuning heater of the first DFB measured (Box1 Chip11) was broken at 125mA. As it can be observed, the DFB in Box1 Chip11 was measured at 25°C and 50°C and we obtained higher output power for the 25°C case (the LIV curves from HHI are measured at 50°C). Then, the LIV curves of the

other two measured DFBs samples were measured at 25°C. Moreover, the output power is lower than expected. From HHI LIV curves, we expected 6mW at 120mA driving current for a wavelength of 1550nm. In our case, we obtained around 2mW at 120mA and a maximum output power of 4.6mW at 100mA, 4.3mW at 105mA, and 4mW at 85mA for the DFBs in the Chip11 of Box 1, Box3 and Box 4, respectively. Finally, the threshold current was around 10mA in all the measured DFBs, as expected from HHI specs.

Next, Figure B.11. (b) shows the spectra of different DFB lasers over the supported wavelength range, and it is measured at 50°C and for 40mA driving current demonstrating the tuning capability. It was measured by sweeping the tuning current (I_{tune}) and using a Python script. For each tuning current, the spectrum measured in the OSA was saved. As can be observed from measured spectra, the DFBs showed a side-mode suppression ratio >50dB, as expected from HHI specs.

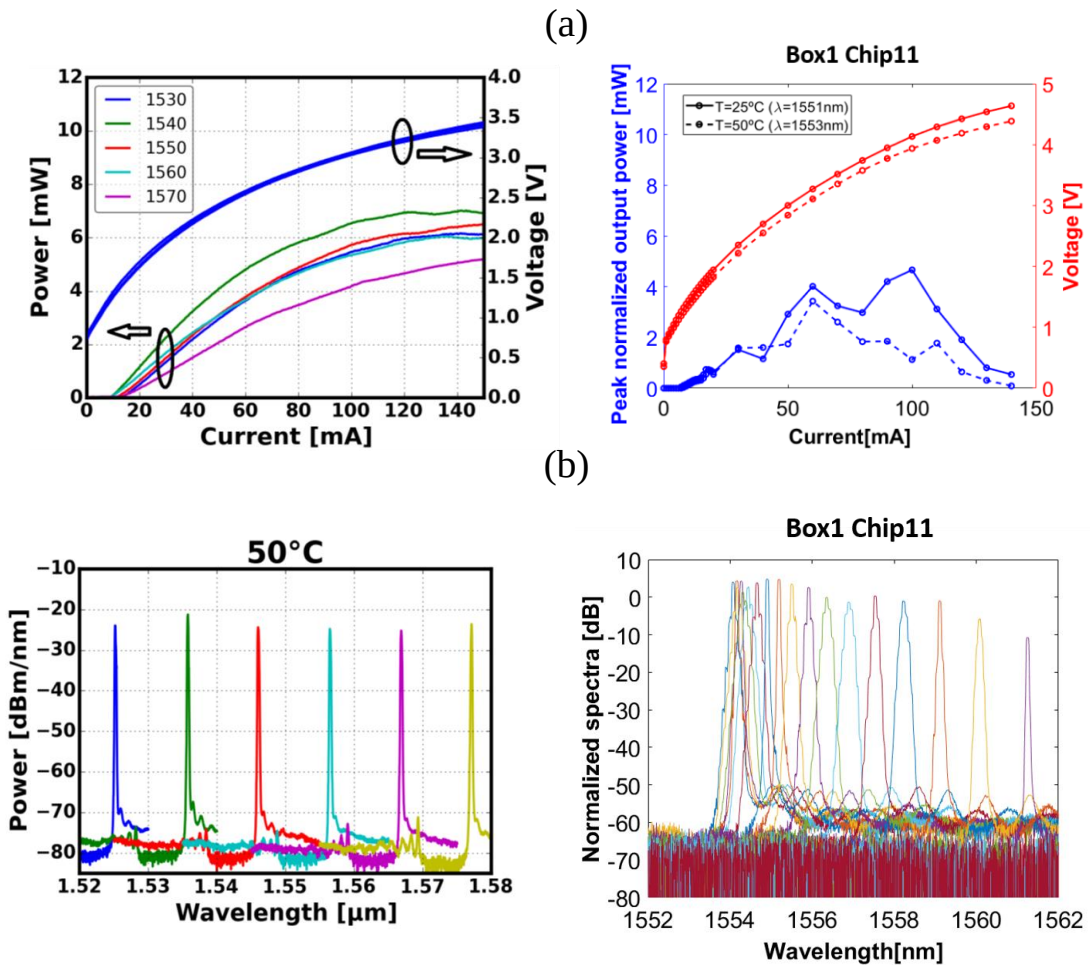

Figure B.11. (a) Pulsed LIV curves for DFB devices with different wavelengths for 50°C provided in the design manual (left) vs. measured in the test (right). (b) Spectra of different DFB lasers measured at a temperature of 50°C and a drive current of 40mA provided in the design manual (left) vs. measured in the test (right).

From the above figures, we can obtain the wavelength shift as a function of the current and the normalized peak output power as a function of the wavelength, see Figure B.12 left and right, respectively. In the first case, we observe that the wavelength shift is not linear with the tuning current (the higher the current, the higher the wavelength shifts). In the second case, we can observe a wavelength tuning range up to 3nm, as expected from HHI specs. It should be highlighted here that the normalization was done by subtracting

only half of the straight waveguide losses as only one side with only one SSC of the DFB is measured.

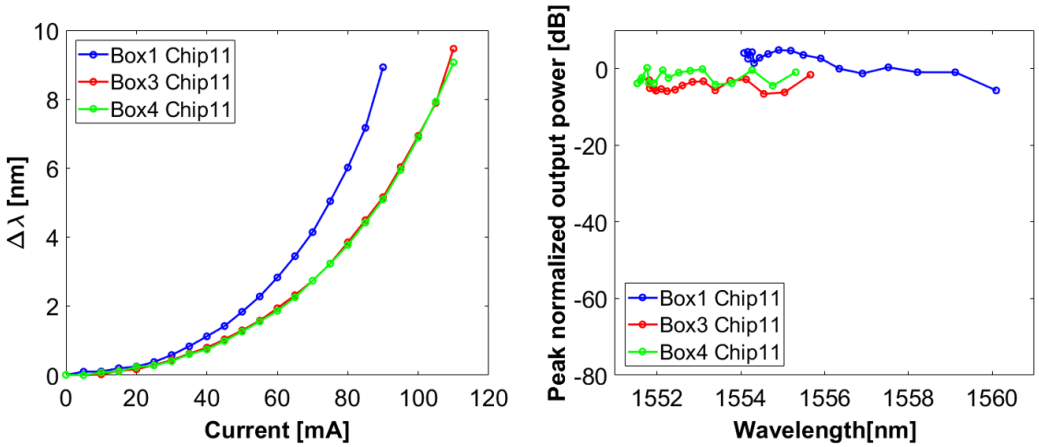

Figure B.12. Wavelength shift versus tuning current (left) and normalized output power of the lasing mode as a function of the wavelength.

After the driving and tuning measurements, direct modulation of the lasers was carried out. The setup used is shown in Figure B.13. As previously, DC probes are used to tune the laser, although in this case, the direct-modulation RF responses have been measured without tuning current (I_{tuning}=0mA) and only for different driving currents, which is fed to the DFBs through a RF GSG probe (50A-GSG-150-DP from GGB Industries) with the RF signal by using a BiasT (SHF BT 45A). The driving current is provided by a power supply (Keithley 2401) and the RF signal is provided by the electrical port of the optical network analyzer (PNA-X, Agilent N4373C). The modulated light is collected by the cleaved output fiber and photo-detected by the internal photodetector in one of the optical input ports of the light-wave analyzer LCA (Agilent N4373C). This allows us to measure the electro-optic (EO) transmission parameter (S_{21}).

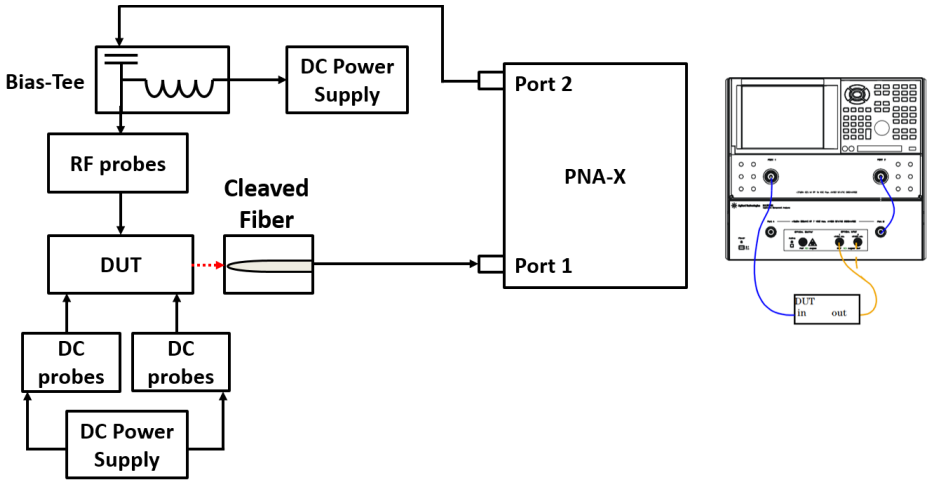

Figure B.13. Setup used for DFBs direct modulation measurement.

The direct-modulation RF responses for different driving currents provided by HHI in the design manual are shown in Figure B.14. (a). Then, our results for the measured DFBs are shown in Figure B.14. (b). Finally, a summary of the EO 3dB bandwidth estimated from the RF responses is presented in Table B. 5. We obtained lower 3dB bandwidths compared to HHI results, but it could be maybe because PNA-X was not calibrated

previously to the measurements (no calibration kit was available in the lab). However, the behaviour measured with the current was appropriate as higher driving currents presented more broadband responses, and therefore, higher 3dB EO bandwidths.

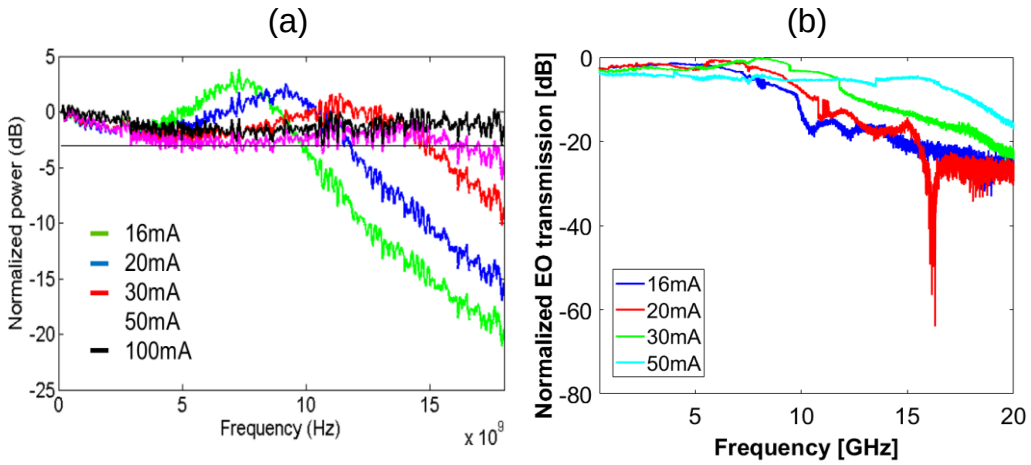

Figure B.14. (a) Direct-modulation RF responses measured by HHI and (b) Direct-modulation RF responses measured by us for different bias currents (Chip 11 – Box1).

Table B. 5. EO 3dB bandwidth obtained from direct-modulation RF responses both from HHI and from our experiments.

I_{drive}	BW_{3dB} provided by HHI	BW_{3dB} DFB Box1 Chip11	BW_{3dB} DFB Box3 Chip11	BW_{3dB} DFB Box14Chip11
16mA	≈ 10GHz	≈ 7GHz	≈ 2GHz	≈ 3GHz
20mA	≈ 12GHz	≈ 9GHz	≈ 4GHz	≈ 5GHz
30mA	≈ 15GHz	≈ 12GHz	≈ 6.5GHz	≈ 8GHz
50mA	≈ 17Ghz	≈ 17Ghz	≈ 10GHz	≈ 11GHz
100mA	>20GHz	--	≈ 11.5GHz	≈ 12GHz

Distributed Bragg Reflector Laser characterization

The next device we decided to include in the chip design is a Distributed Bragg Reflector Laser see Figure B.15. The DBR laser is based on ridge-waveguide structures and contains internally a QW-based SOA (p2/n2 pads) which is used to drive the DBR and a rear DBR grating (p1/n1 pads), a current-injection phase modulator (p3/n3 pads) and a front DBR grating (p4/n4 pads) which are used to tune the DBR observe Figure B.15. (b) and (c). The QWs are only contained in the SOA sections, and the gratings are index-coupled gratings inside a 250nm Q (1.3) core layer. Light exits right sides of the device. By default, we maintained the lengths of this device like: Length front reflector (FR) = 100µm, Length front isolation (IF) = 30µm, Length middle isolation (IM) = 30µm, Length rear isolation (IR) = 30µm, Length Phase section (PS) = 100µm, Length Rear Reflector (RR) = 100µm, Length SOA = 100µm, Wavelength FR = 1550nm, Wavelength RR = 1550nm.

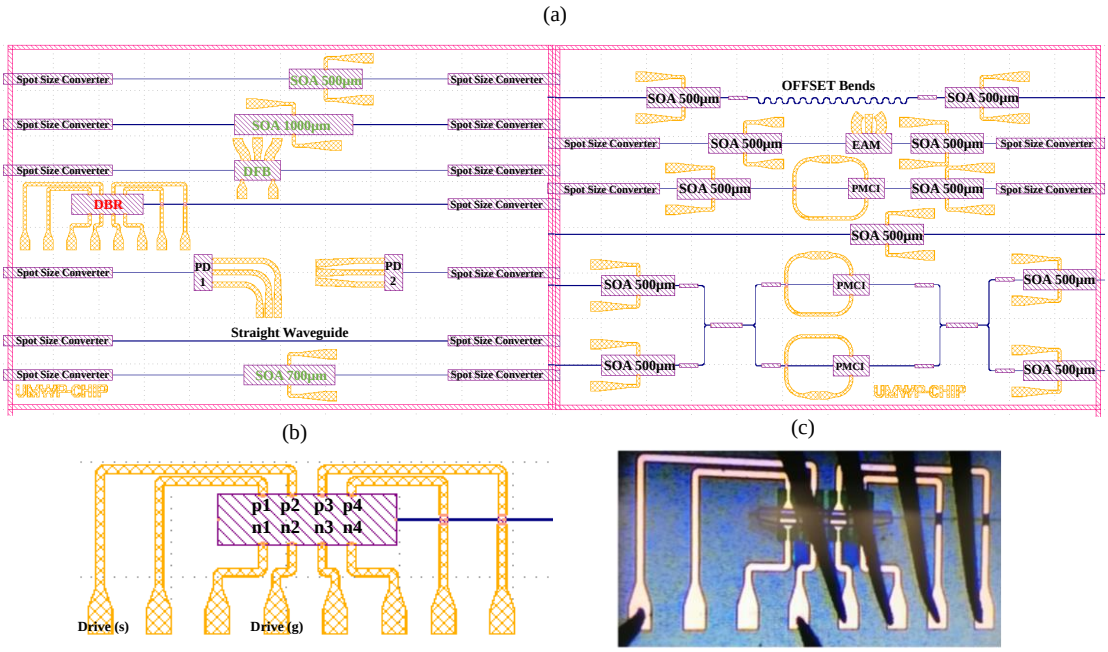

Figure B.15. (a) Disposal of DBR in the design of the chip (highlighted in red), (b) DBR mask layout showing the electrical pads and the optical port, and (c) Fabricated device during the measurements with 2x DC probes and a DC multi-contact probe.

Then, we measured six DBRs in total and only one of them worked. The HHI data provided for DBRs in the design manual 6.0 are shown in Table B. 6.

Table B. 6. DBRs specification data provided by HHI Fraunhofer.

Parameter	Value provided
Wavelength tuning range	3nm
Wavelength accuracy	±5nm
Side-mode suppression	>50dB
Single-sided output power	3mW @ 150mA
Linewidth	1MHz
Threshold current	25mA

For tuning and driving characterization we used the setup shown in Figure B.16. Both driving and tuning should be carried out by using DC probes. There are eight heater pads per laser, so, we used a multi-contact DC probe of 250µm pitch and 2 standalone DC probes as not all the tips in the multi-contact were in good condition. The probes were directly connected to two source meters (Power supplies, Keithley 2401) through micro-positioners microworld S725PLM/PRM in the case of standalone DC probes and through a micro-positioner XYZ 300ML Quarter Research and Development Inc. in the case of the multi-contact DC probe. The light emitted by the DBR laser is collected by the cleaved output fiber and divided by a 50/50 optical splitter to a power meter (Greenlee 560XL) and an optical spectrum analyzer (Yokogawa AQ6370C) with the aim of align the output fiber maximizing the output power with the power meter and simultaneously measure the spectrum in the OSA.

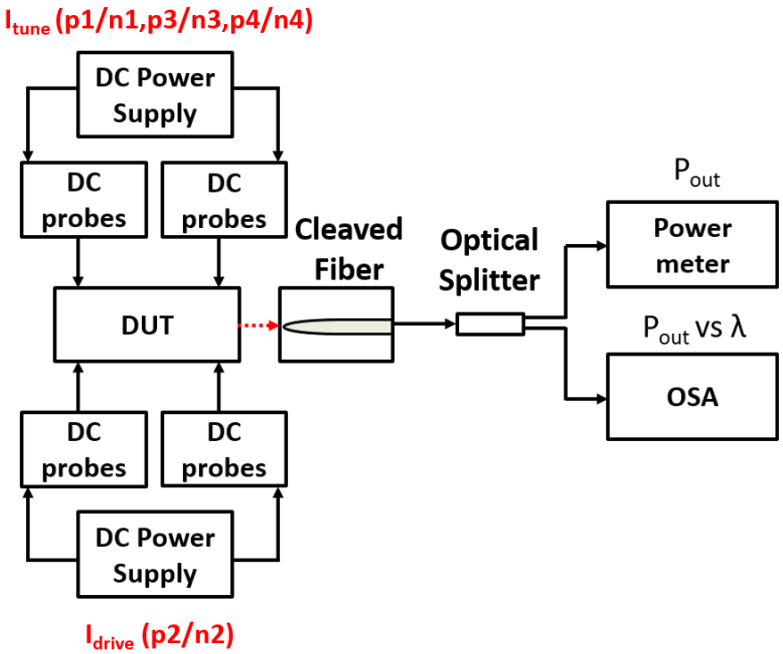

Figure B.16. Setup used for DBRs tuning and driving characterization.

From Figure B.17. (a), which shows the measured spectra for different driving currents, and making a post-processing we obtained the LIV curve of the DBR (sample Box3 Chip11). It is shown in Figure B.17. (b). As it can be observed by comparing with the curve provided by the design manual of the device (Figure B.17. (c)), it was obtained a lower output power than expected. Moreover, no output power was measured in the measured wavelength range for driving currents above 100mA, probably due to peak mode hopping. Measured threshold current was about 10mA, much below the value provided by HHI (25mA). The side-mode suppression was >50dB, as expected. It should be highlighted here that the normalization was done by subtracting only half of the straight waveguide losses as only one side with only one SSC is presented in the DBR.

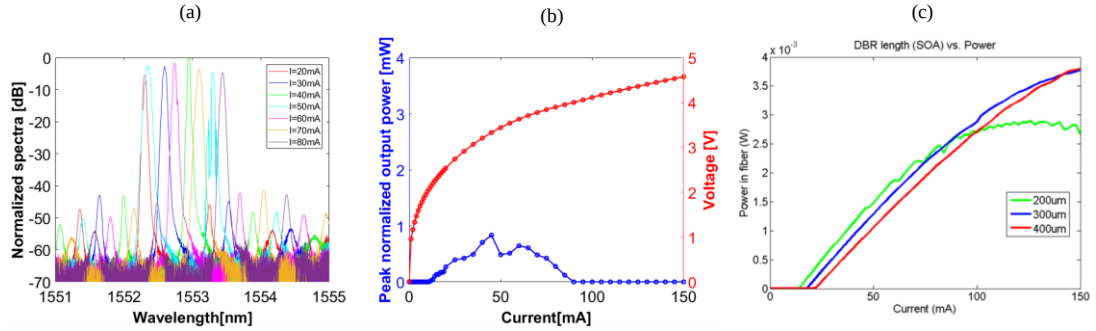

Figure B.17. (a) Box3 Chip21 DBR spectra for different driving currents, (b) LIV curve obtained from measured spectra, and (c) LIV curve provided by HHI in the design manual 6.0.

After driving characterization, we characterized the tuning capability. For that, we swept separately the tuning current of each tuner element by using a Python script. For each tuning current, we saved the spectrum measured in the OSA. Results are shown in Figure B.18. The left column shows the measured spectra for different tuning currents, the middle column shows the output power as a function of the tuning current and the right column shows the wavelength shift as a function of the tuning current.

Figure B.18. (a) shows the results obtained by tuning the front grating element of the DBR, Figure B.18. (b) shows the results obtained by tuning the phase section element of the DBR and Figure B.18. (c) shows the results obtained by tuning the rear grating element of the DBR. As it can be extracted in general from measured curves, there is a random behaviour in the wavelength shift when tuning is carried out. In addition, jumps in the peak wavelength are observed, we did not obtain a continuous tuning and we could not check the wavelength range of 3nm provided by HHI in the design manual version 6.0.

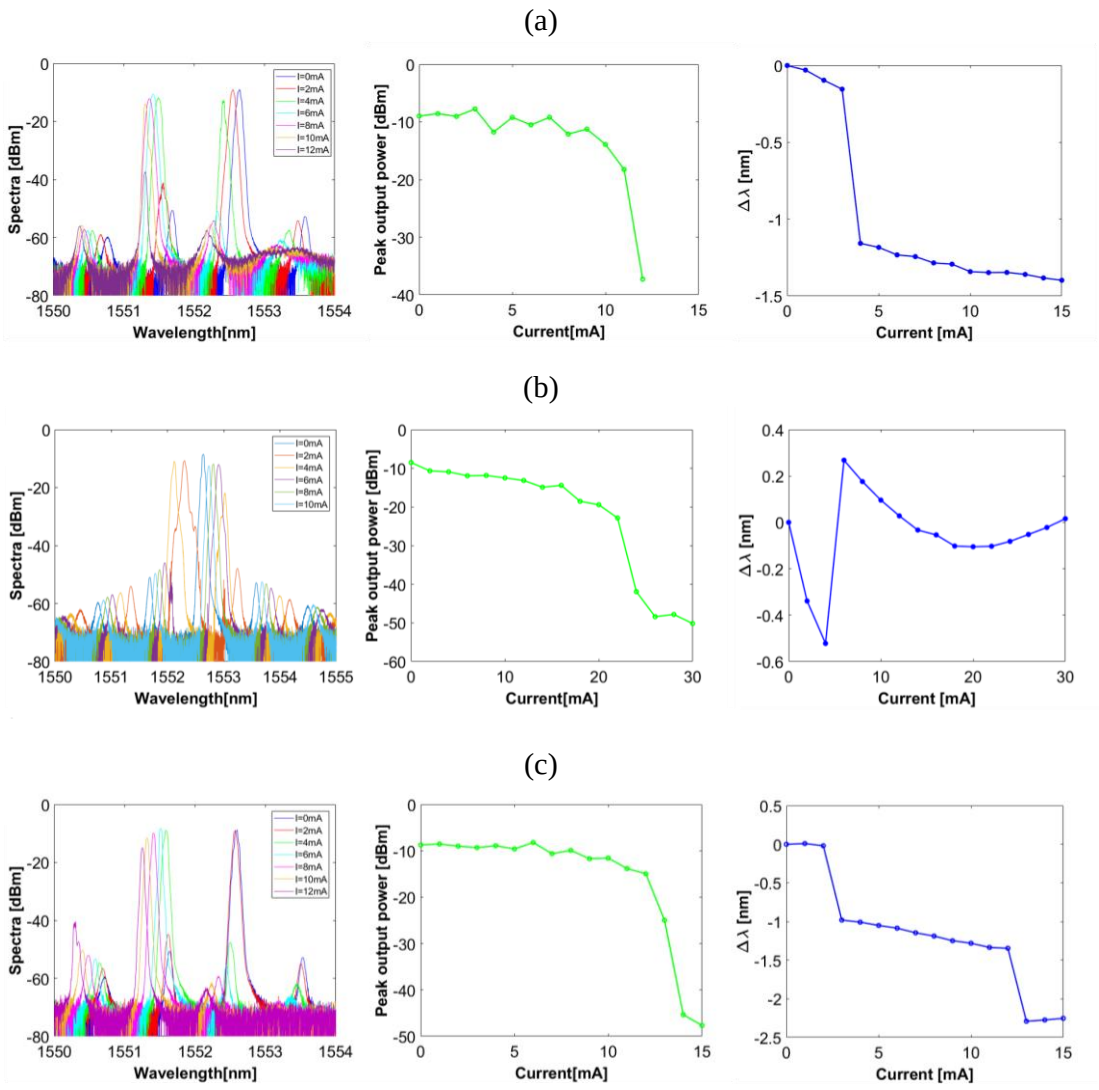

Figure B.18. Measured spectra for different tuning currents (left column), peak output power as a function of the tuning current (middle column), and wavelength shift as a function of the tuning current (right column), tuning the (a) Front grating tuner (p4/n4), (b) Phase section (p2/n2) and (c) Rear grating tuner (p1/n1).

In conclusion, DBRs don't work (only one worked from six measured). The only working DBR measured presented in general good parameters except the output power, which was lower than expected.

Photodetectors characterization

After that, we want to test the performance of the high-speed PIN photodiodes shown in Figure B.19. (a). In order to test how bends affect the RF metallization, we placed the tracks and pads of two photodetectors as shown in Figure B.19. (b). One of them with bent tracks (PD_1) and the other with straight tracks (PD_2).

(a)

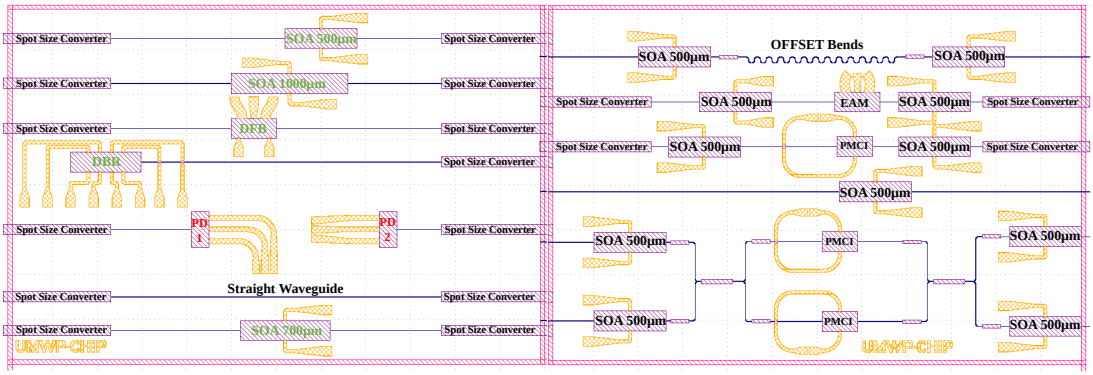

(b)

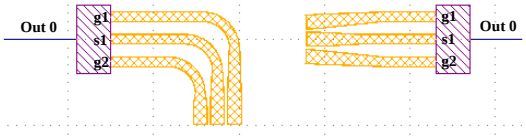

Figure B.19. (a) Disposal of PDs in the chip (highlighted in red), (b) PDs mask layout showing the electrical pads and the optical ports.

The PDs expected performance is shown in Table B. 7. The data are provided in the design manual version 6.0. As can be observed in the table, the expected responsivity was 0.8A/W @1550nm. However, in the HHI validation report (version 06-05-2020) it is said that PD+SSC responsivity is 0.45A/W due to fabrication issues.

Table B. 7. PDs specification data provided by HHI Fraunhofer.

Parameter	Value provided
Sensitivity (Responsivity)	0.8A/W@ 1550nm
Linear regime input powers	<10dBm
Polarization dependence	<0.8dB
Dark current	<10nA @ -2V
3 dB bandwidth	~ 45GHz
Maximum reverse voltage before failure	-6V

First, we started with the static characterization to obtain the PDs responsivities. Moreover, PDs were characterized in both dark (laser turned off) and illumination (laser turned on) regimes. In dark regime, the VI curve was obtained by sweeping the PD bias voltage with a Python script. In illumination regime, the objective was to obtain the optical power versus the output photo-detected current curve. For that, we should sweep the optical input power by using a Python script and save the VI curve obtained from the source meter for each optical input power. The setup we used is shown in Figure B.20. (a). The light emitted by a laser (Yenista T100R), after a polarization controller, is introduced to the photodetector through the cleaved input fiber. Moreover, the bias voltage of the PD is applied by the source-meter (Keithley 2401) through a GSG RF probe with 100µm pitch (50A-GSG-100-DP from GGB Industries), as shown in the sketch of Figure B.20. (b). Then, the photo-detected current is measured in the source-meter. To obtain the optical input power versus the output photo-detected current curve, the fiber input was aligned by maximizing the photocurrent measured in the source-meter with the laser turned on. It should be mentioned that all the measurements carried out were repeated with the same setup but

added a biasT (SHF BT-45) between the source and the RF probes. The results were the same with and without the biasT.

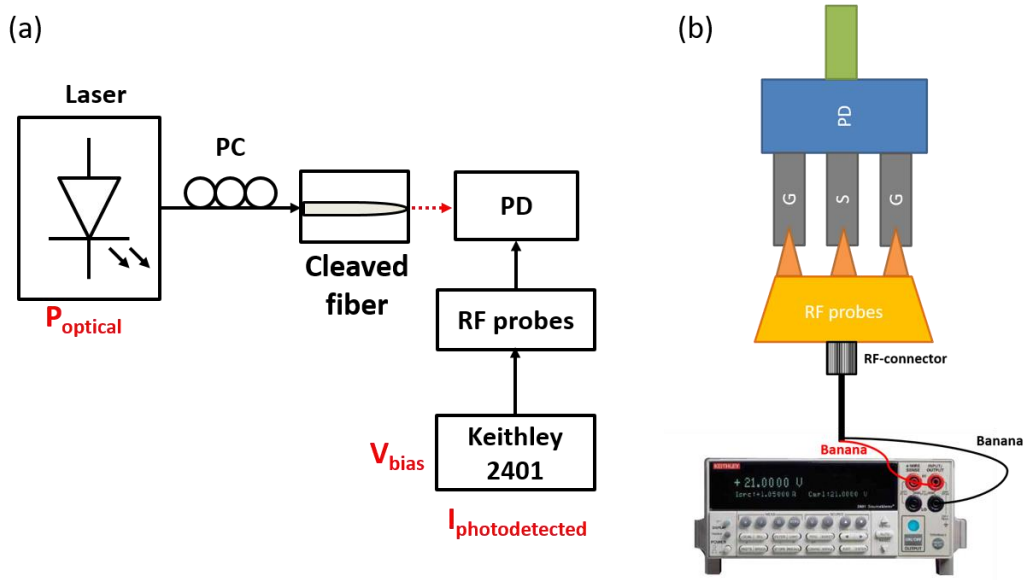

Figure B.20. (a) Setup used for PDs static characterization and (b) sketch indication of the connection between the source meter Keithley 2401 and the PDs.

Different events happened during different PDs characterizations. Some PDs were maybe broken during the dark regime characterization. It should be highlighted here that reverse bias voltage never was decreased below -4V (maximum reverse voltage before failure is -6V according to data in the design manual version 6.0). Figure B.21 shows the VI curve measured in dark regime for PD_1 (Figure B.21. (a)) and PD_2 (Figure B.21. (b)) in Box1 Chip11. As it can be observed, dark currents in the order of µA in PD_1 and mA in PD_2, much above the expected (<10nA@-2V) from the design manual, were measured the first time we measured the VI curve. The PDs may be broken at any point during the first VI measurement because much lower dark currents were obtained the second time.

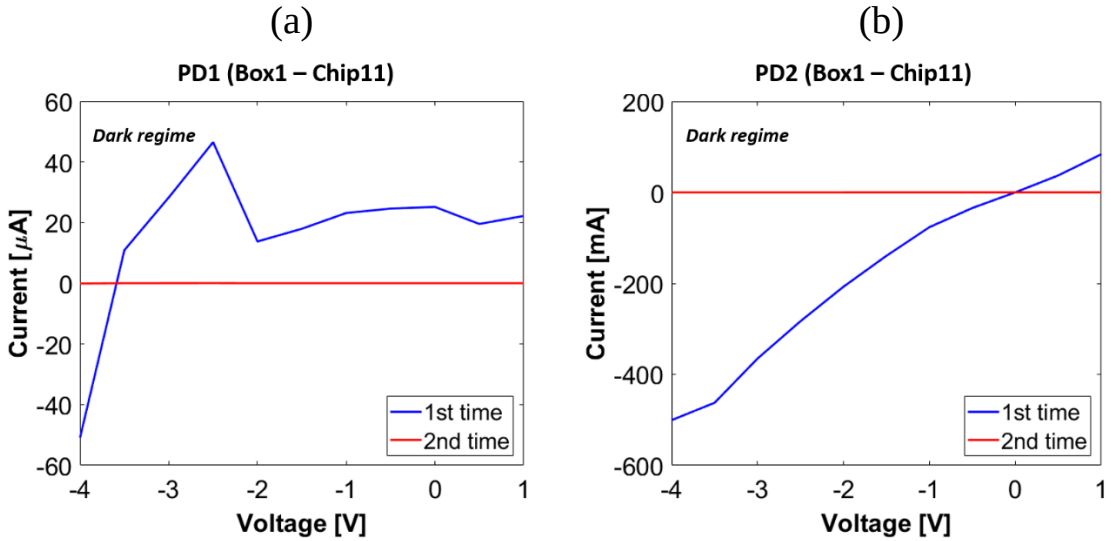

Figure B.21. Measured VI curve in dark regime of PDs in Box1 Chip11.

Other PDs showed a shortcut behaviour, when the input levels exceed the maximum levels, it causes the “OVERFLOW” message in the power-supply (Keithley 2401), and they could not be measured.

PD_2 (Box2 Chip11) showed the typical VI diode performance, but low photocurrent was measured. Therefore, a very low responsivity was obtained. Figure B.22. shows the measured results in both dark and illumination regimes. In the top part of the figure, it is shown the VI curves for different optical input powers. On the other hand, the bottom part shows the calculated responsivity (as photo-detected current divided by the optical input power). As can be observed from IV curves, low photo-detected currents in the order of µA were measured. Hence, a responsivity below 0.005A/W (constant only between 0V and -2V) was obtained. We took the opportunity with this PD to test the influence of a biasT between the power supply (Keithley 2401) and the RF probes. As can be observed by comparing Figure B.22. (a) and Figure B.22. (b), the biasT did not affect the measurement.

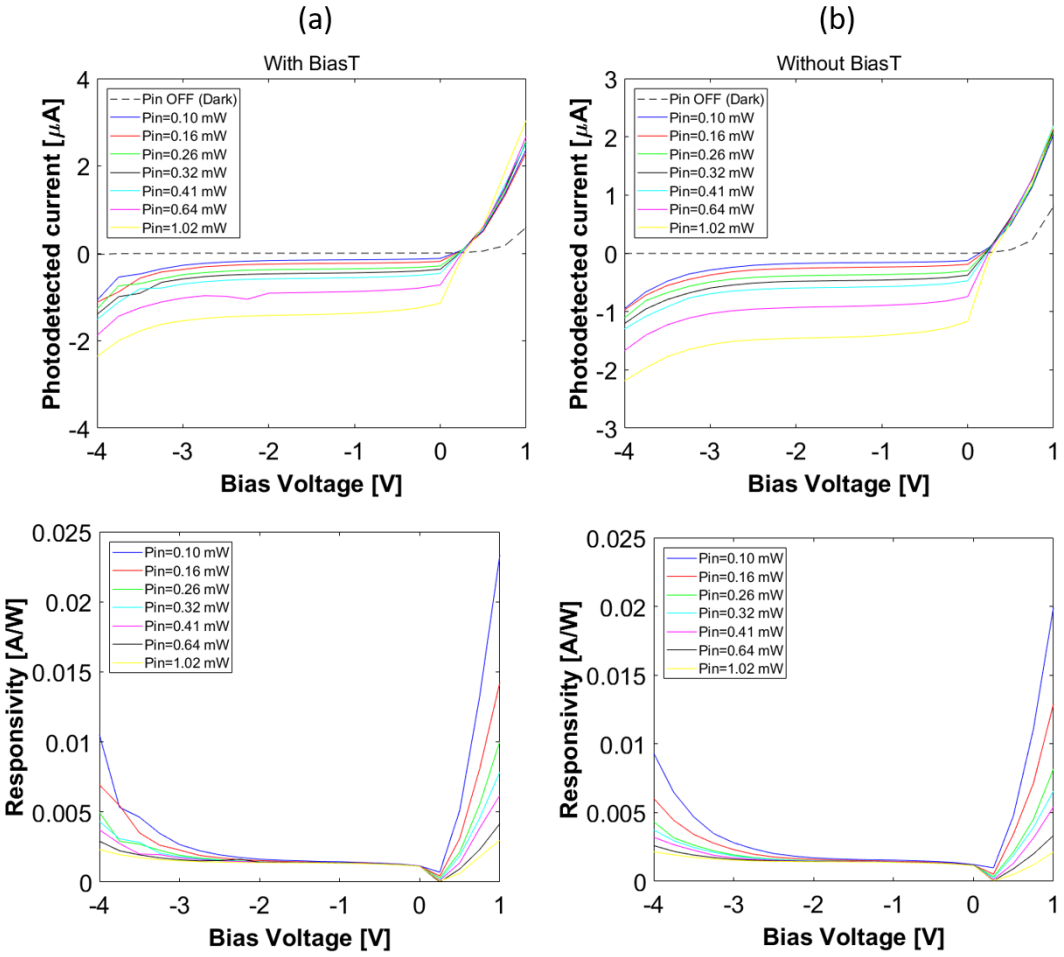

Figure B.22. Measured VI curves (up) and responsivity (down) for different optical input powers, in dark and illumination regimes of PD2 in Box2 Chip11 measured (a) with biasT and (b) without biasT.

Several PDs burst during the dark regime measurement at bias voltages well above -6V. Pictures are shown in Figure B.23. The Figure B.23. (a) shows the PD_2 (Box3 Chip21) which exploded at V_{bias} = -4V. Then, Figure B.23. (b) shows the PD_2 (Box4 Chip11) which exploded at V_{bias} = -4V. Finally, Figure B.23. (c) shows the PD_2 (Box4 Chip21) burst at V_{bias} = -3V.

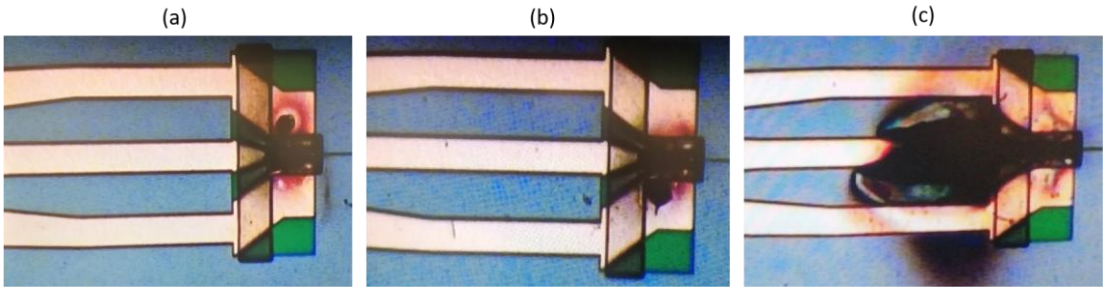

Figure B.23. Pictures of different samples of PD_2 burned trying to measure the VI curve in dark regime. (a) Box3 Chip21, (b) Box4 Chip11 and (c) Box4 Chip21.

Next, Table B. 8. shows a summary of what happened during the measurement of the different photodetectors. As we already anticipated at the beginning of this section, no photodetector working well was found.

Table B. 8. Characterized PDs and state they are in after their measurements.

Box	Chip	Device	Comment
BOX 1	CHIP 1_1	PD1	Broken in the dark regime measurement
		PD2	Broken in the dark regime measurement
	CHIP 2_1	PD1	Never measured, directly it didn't work
		PD2	Broken in the dark regime measurement
BOX 2	CHIP 1_1	PD1	Never measured, directly it didn't work
		PD2	Measured → Responsivity too low
	CHIP 2_1	PD1	Never measured, directly it didn't work
		PD2	Never measured, directly it didn't work
BOX 3	CHIP 1_1	PD1	Measured → Responsivity too high (high dark current)
		PD2	Exploded in the dark regime measurement
	CHIP 2_1	PD1	Measured → Responsivity too high (high dark current)
		PD2	Exploded in the dark regime measurement
BOX 4	CHIP 1_1	PD1	Measured → Responsivity too high (high dark current)
		PD2	Exploded in the dark regime measurement
	CHIP 2_1	PD1	Measured → Responsivity too high (high dark current)
		PD2	Exploded in the dark regime measurement

After the static measurements, direct modulation of a pair of PDs was carried out. The setup used is shown in Figure B.24. As previously, RF probes are used to bias the PD, and in this case, we used a biasT (SHF BT-45) to extract the photodetected RF signal. Again, a RF GSG probe (50A-GSG-100-DP from GGB Industries) is used, and the bias voltage is provided by the power supply (Keithley 2401). This time, the light injected into the photodetector is provided by one of the output optical ports of the light-wave component analyzer (LCA, Agilent N4373C). Then, the photodetected RF signal is introduced to one of the electrical ports of the optical network analyzer PNA-X (Agilent N4373C), allowing to measure of the opto-electric (OE) transmission parameter (S_{21}).

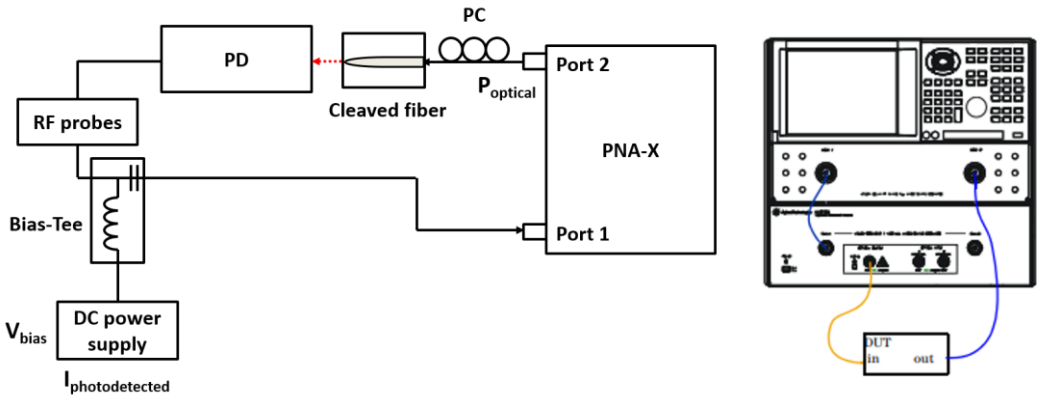

Figure B.24. Setup used for PDs direct modulation.

Measured OE S_{21} RF-responses are shown in Figure B.25. (a) and Figure B.25. (b) for PDs_1 (Box3 Chip21 and Box4 Chip11, respectively). Figure B.25. (c), also shows the RF-responses provided by HHI in the design manual version 6.0. As it can be observed, we obtained much lower 3dB bandwidths compared to HHI results. It could be maybe because PDs are not working well, and the PNA-X was not calibrated previously to the measurements (no calibration kit was available in the lab). However, the behaviour measured with the bias voltage was correct as higher bias voltages presented more broadband responses, and therefore, higher 3dB EO bandwidths.

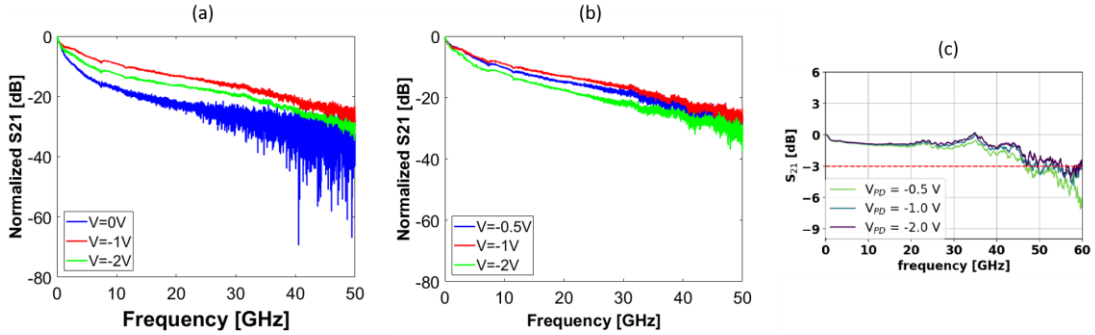

Figure B.25. Direct-modulation RF responses for different PD bias voltages measured for PD1 in (a) Box3 Chip21, (b) Box4 Chip11 and (c) provided by HHI in the design manual 6.0.

Electro Absorption Modulator characterization

Now, we want to characterize the Electro Absorption Modulator (EAM) building block. This intensity modulator is based on the Quantum-Confined Stark Effect (QCSE) and it is 200µm length. Next, Figure B.26 (a) and (b) show the disposal of the EAM in the design chip layout and the mask layout of one EAM, respectively. As can be seen, they have two optical ports (input/output) accessible by edge-coupling through SSCs and three RF pads to drive it.

(a)

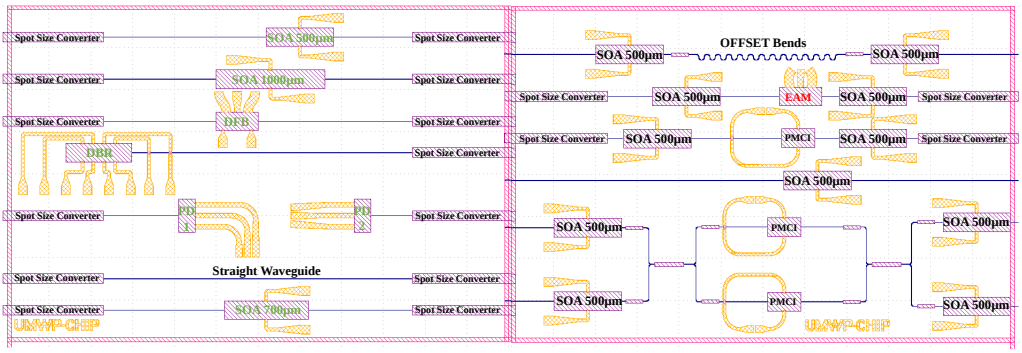

(b)

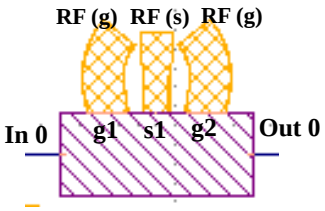

Figure B.26. (a) Disposal of the EAM (highlighted in red) in the design2 chip and (b) mask layout of a standalone EAM showing the pads and the optical ports.

Next, data provided for EAMs in the design manual v.6.0 are shown in Table B. 9.

Table B. 9. EAMs data provided by HHI Fraunhofer design manual.

Parameter	Value provided	For L=200µm length
Extinction ratio (DC) per length	0.1dB/µm	20dB
Optical losses TE	3 dB + 25 dB/mm	8dB
Optical losses TM	3 dB + 5 dB/mm	4dB
3dB frequency	20GHz	--
Series resistance	4Ωmm	20Ω

All the EAMs were measured in DC regime. The setup used is shown in Figure B.27. They were driven by using a GSG 150µm pitch RF probe (50A-GSG-150-DP from GGB Industries) connected to a source meter-power supply (Keithley 2401) after a biasT (SHF BT-45). The aim of using the biasT is to be able to measure later the RF response by only adding the RF input through a micro-positioner (XYZ 300ML from Quarter Research and Development Inc). The light injected by a tunable laser (AQ4321D ANDO) was passed through a polarization controller before being injected into the input cleaved fiber. After the chip, the light was collected by the cleaved output fiber and divided by a 50/50 optical splitter to a power meter (Greenlee 560XL) and an optical spectrum analyzer (Yokogawa AQ6370C) with the aim of align the fibers maximizing the output power with the power meter and simultaneously measure the spectrum in the OSA.

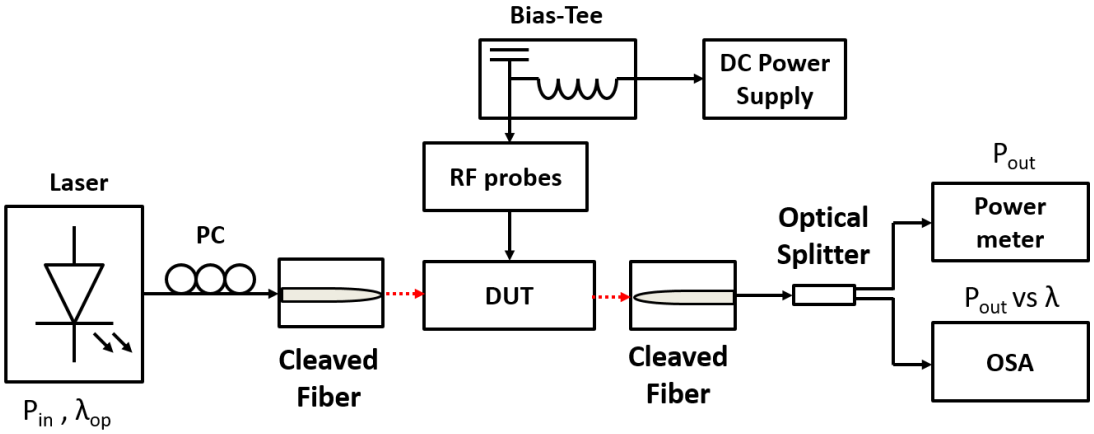

Figure B.27. Setup used for EAM DC regime characterization.

To obtain the EAM transmission for different bias voltages, we swept the bias voltage by using a Python script and we saved the spectrum for each bias voltage. First, we obtained the VI curves, and they are shown for all the EAMs in Figure B.28.

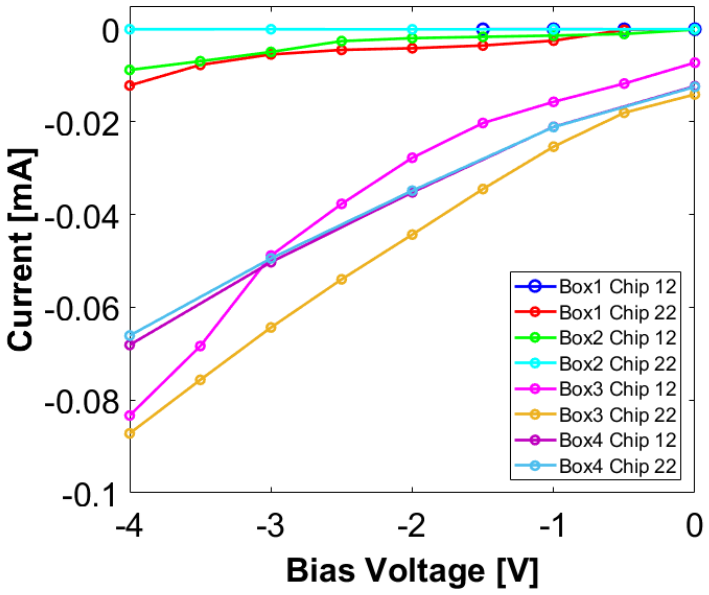

Figure B.28. VI curves were measured for all the EAMs available in the chips.

The measured transmission spectra of all EAMs are shown in Figure B.29. As it can be extracted, very low extinction ratios are obtained, compared with expected (ER>20dB). Maximum ER measured is 4.65dB @1550nm for a bias voltage of -4V in the EAM (placed in Box3 Chip22). Definitively, we can say that EAMs were not working. Then, RF frequency response was not measured.

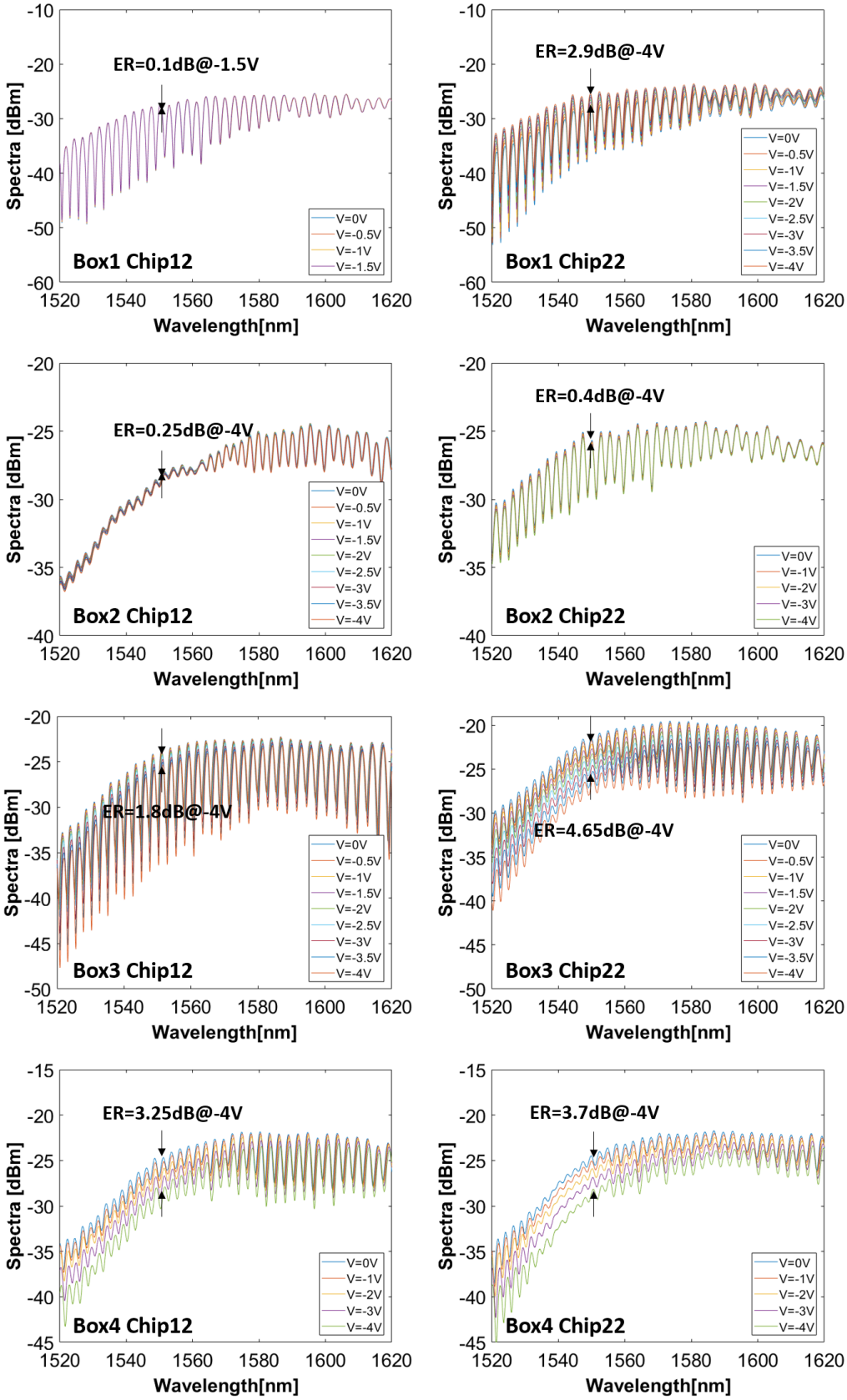

Figure B.29. EAMs transmission spectra measured for different bias voltage. In each case, the extinction ratio at 1550nm is indicated.

Current-Injection Phase Modulator characterization

The Current-Injection Phase Modulator (PMCI) is based on a bulk ridge waveguide structure. The ridge-waveguide stripe is around 2.4µm wide and the modulator has a length of 100µm. Figure B.30 (a) and (b) show the disposal of the PMCI in the design chip layout and its standalone mask layout, respectively. As it can be viewed, it has two optical ports (input/output) accessible by edge-coupling through SSCs and a pair of DC pads to drive it.

(a)

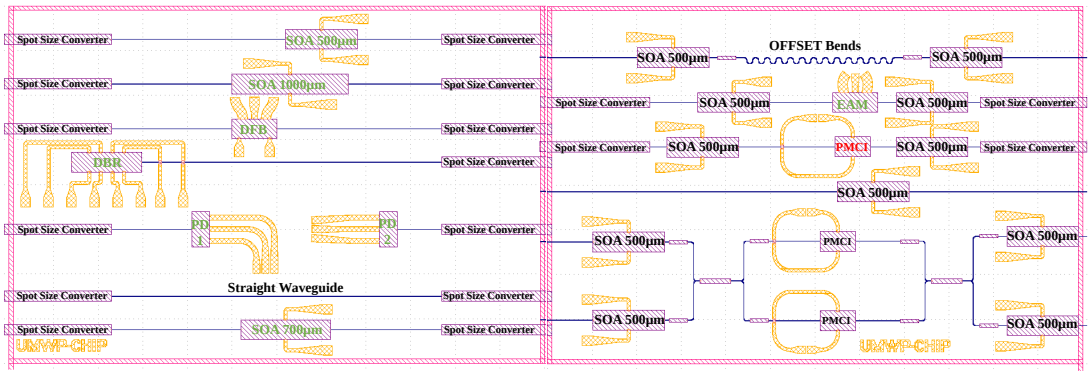

(b)

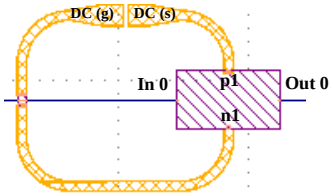

Figure B.30. (a) Disposal of the EAM in the design2 chip and (b) mask layout of a standalone EAM showing the pads and the optical ports.

Next, data provided for PCMIs in the design manual v.6.0 are shown in Table B. 10.

Table B. 10. PMCI data provided by HHI Fraunhofer design manual.

Parameter	Value provided	For L=100µm length
Insertion loss	9 dB/cm	0.09dB
$I\pi \times L$	1.25 mA x mm	0.125mA
$V\pi \times L$	8 V x mm	0.8V
Electro-optic 3dB bandwidth	~200MHz	--

The PMCI was measured in DC regime. The setup used is shown in Figure B.31. They were driven by two DC probes directly connected to a source-meter (power supply Keithley 2401) through two micro-positioners (Microworld S725PLM/PRM). The light injected by a tunable laser (AQ4321D ANDO) was passed through a polarization controller before being injected into the input cleaved fiber. After the chip, the light was collected by the cleaved output fiber and divided by a 50/50 optical splitter to a power meter (Greenlee 560XL) and an optical spectrum analyzer (Yokogawa AQ6370C) to align the fibers maximizing the output power with the power meter and simultaneously measure the spectrum in the OSA.

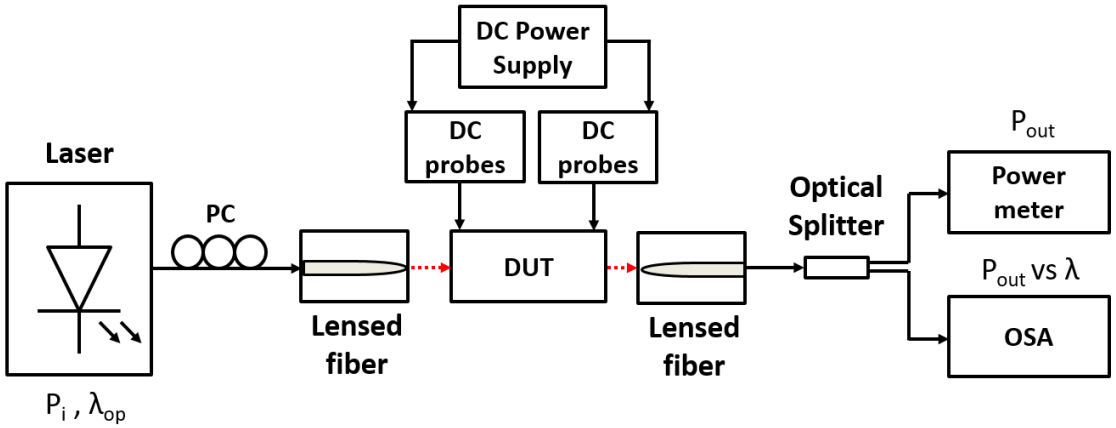

Figure B.31. Setup used for PMCI characterization.

A pair of examples of measured transmission spectra for different bias voltages are shown in Figure B.32. (a) and (b) for two PMCI samples (Chip12 from Box3 and Box4, respectively). Finally, Figure B.32. (c) shows the normalized output power (respect to a straight waveguide with SSC in both input and output sides) measured at 1550nm as a function of the bias voltage. Anyway, as they are phase modulators, it is easy to measure the intensity response of an interferometric structure with these phase modulators in each arm (see next section).

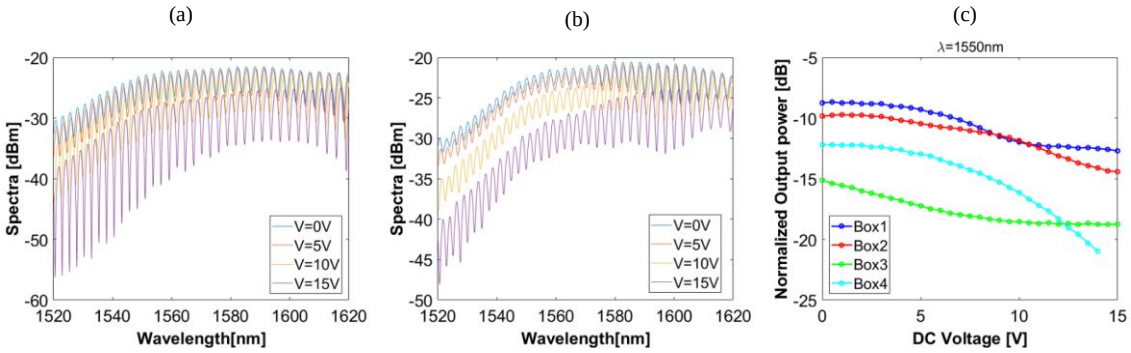

Figure B.32. EAMs transmission spectra measured for different bias voltage. In each case, the extinction ratio at 1550nm is indicated.

Programmable unit cell characterization

Finally, we placed the previous PMCI in both arms of a Mach-Zehnder Interferometer-based PUC structure, as shown in Figure B.33. The length of the PMCIs is again 100µm.

The expected performance of a Mach-Zehnder structure with a 250µm long PMCI on both arms is provided in the design manual v.6.0 and it can be seen in Figure B.34. (a). As it can be extracted from figure, a current of around 5mA is needed for a π-phase shift. In our case, as the PCMIs are shorter (100µm) the I_π should be lower. The driving of the PMCIs was carried out in the same way explained in the previous section. Then, transmission spectra for different currents of our PUC with a 100µm long PMCI on both arms were measured by tuning the PMCI Down and the PMCI Up. Finally, the switching curve was obtained by taking the optical output power at 1550nm operational wavelength from the measured spectra. As can be observed in Figure B.34. (b), it is not a typical intensity modulator response as expected. This means that the PCMIs are probably not working. We measured several PUCs and although the results from only one PUC are shown here, the rest showed the same performance.

(a)

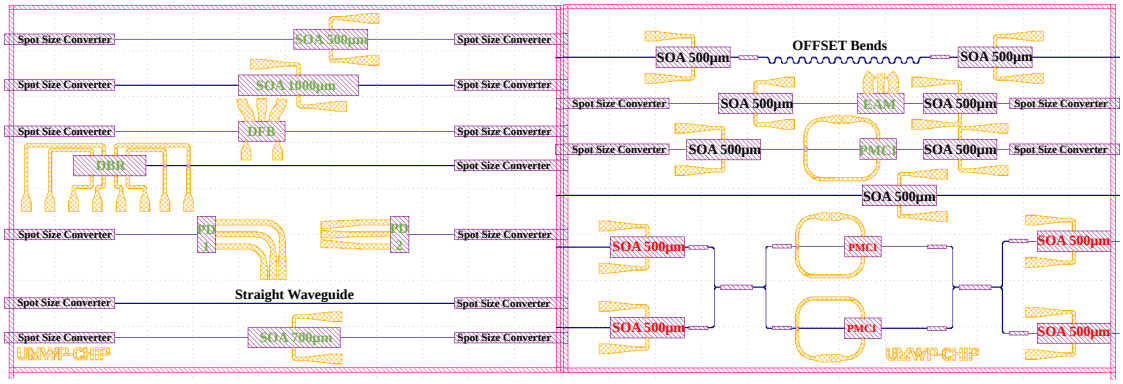

(b)

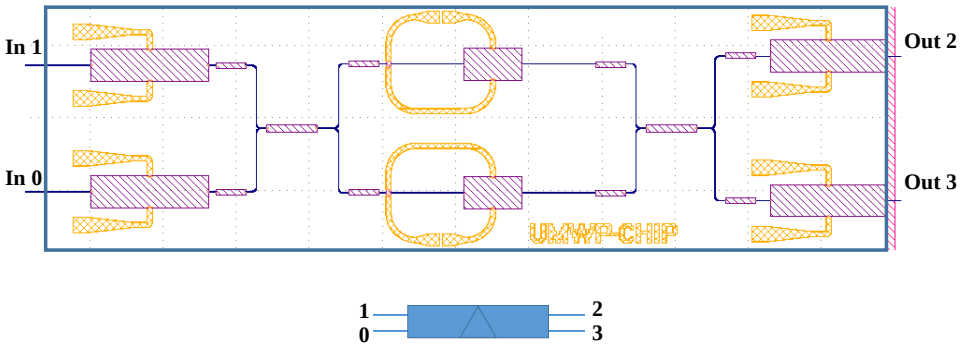

Figure B.33. (a) Disposal of the PUC in the chip design and (b) Mask layout of the PUC forming by two PMCI in each arm of a MZI structure and schematic of the equivalent PUC.

(a) (b)

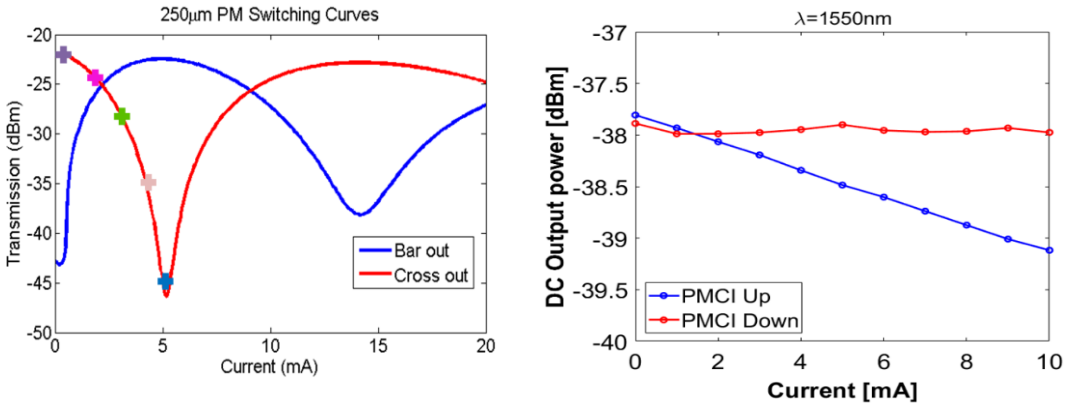

Figure B.34. (a) Switching curve of a Mach-Zehnder structure with a 250µm long PMCI on both arms provided by HHI Fraunhofer design manual. (b) Switching curve obtained by taking the optical output power at 1550nm operational wavelength.

List of publications

Journals

J.1. E. Sánchez, A. López; D. Pérez-López, "Simulation of Highly Coupled Programmable Photonic Circuits" Journal of Lightwave Technology, 2022, vol. 40, no 19, p. 6423-6434, (2022).

J.2. E. Sánchez, D. Pérez-López, P. DasMahapatra, and J. Capmany, "Modeling amplified arbitrary filtered microwave photonic links and systems," Opt. Express 29, 14757-14772 (2021).

J.3. E. Sánchez, D. Pérez-López, D. Pérez-Galacho, D. Wessel & J. Capmany, "Modeling amplified arbitrary filtered heterodyne microwave photonic links." Optics Express, 30(5), 6519-6530, (2022).

J.4. D. Pérez-López, A. M. Gutierrez, **E. Sánchez**, P. DasMahapatra, & J. Capmany, "Integrated photonic tunable basic units using dual-drive directional couplers." Optics Express, 27(26), 38071-38086. (2019).

J.5. D. Pérez-López, **E. Sánchez**, & J. Capmany, "Programmable true time delay lines using integrated waveguide meshes." Journal of Lightwave Technology, 36(19), 4591-4601. (2018).

J.6. D. Pérez-López, A. M. Gutierrez, D. Sánchez, A. López, M. Gutierrez, **E. Sánchez**, J. Fernández, A. Cruz, A. Quirós, Z. Xie, J. Benitez, N. Bekesi, D. Pérez-Galacho, P. DasMahapatra and J. Capmany. "General-purpose programmable photonic processor for advanced radiofrequency applications." in review at Nature Communications (2023).

Conference proceedings

C.1. A. López, **E. Sánchez**, D. Pérez, "Simulation of an Arbitrary Optical Switch on a Dense Programmable Photonic Processor" at European Conference and Exhibition on Optical Communication (ECOC). Optica Publishing Group, 2022. p. We5. 22.

C.2. E. Sánchez, D. Pérez-López, P. DasMahapatra, and J. Capmany, "Modeling amplified arbitrary filtered microwave photonic links and systems," at 2020 IEEE International Topical Meeting on Microwave Photonics (MWP), IEEE Conference, 2020, p. 195-198

C.3. D. Perez, A. M. Gutierrez, **E. Sanchez**, P. DasMahapatra, and J. Capmany, "Dual-drive directional couplers for programmable integrated photonics." IEEE Photonics Society Summer Topical Meeting Series (SUM) (pp. 1-2). IEEE. (2019)

C.4. D. Pérez, **E. Sánchez**, D. Doménech, P. Muñoz, and J. Capmany, "Silicon Nitride Tunable Directional Coupler for programmable waveguide meshes." (2018)

C.5. D. Pérez-López, A. López, M. Gutiérrez, D. Sánchez and **E. Sanchez**. "Dynamically reconfigurable Photonic Integrated Circuits and Its Control Algorithms", Conference on Lasers and Electro-Optics (CLEO), Invited presentation, (AM2Q.3), (2023).

References

[1] D. Marpaung, C. Roeloffzen, R. Heideman, A. Leinse, S. Sales, and J. Capmany, “Integrated microwave photonics,” *Laser Photon Rev*, vol. 7, no. 4, pp. 506–538, 2013.

[2] E. J. Norberg, R. S. Guzzon, J. S. Parker, L. A. Johansson, and L. A. Coldren, “Programmable photonic microwave filters monolithically integrated in InP–InGaAsP,” *Journal of Lightwave Technology*, vol. 29, no. 11, pp. 1611–1619, 2011.

[3] H.-W. Chen *et al.*, “Integrated microwave photonic filter on a hybrid silicon platform,” *IEEE Trans Microw Theory Tech*, vol. 58, no. 11, pp. 3213–3219, 2010.

[4] P. Dong *et al.*, “GHz-bandwidth optical filters based on high-order silicon ring resonators,” *Opt Express*, vol. 18, no. 23, pp. 23784–23789, 2010.

[5] J. Lloret *et al.*, “Tunable complex-valued multi-tap microwave photonic filter based on single silicon-on-insulator microring resonator,” *Opt Express*, vol. 19, no. 13, pp. 12402–12407, 2011.

[6] D. Marpaung, C. Roeloffzen, A. Leinse, and M. Hoekman, “A photonic chip based frequency discriminator for a high performance microwave photonic link,” *Opt Express*, vol. 18, no. 26, pp. 27359–27370, 2010.

[7] W. Xue, S. Sales, J. Capmany, and J. Mørk, “Wideband 360 microwave photonic phase shifter based on slow light in semiconductor optical amplifiers,” *Opt Express*, vol. 18, no. 6, pp. 6156–6163, 2010.

[8] P. Berger, J. Bourderionnet, F. Bretenaker, D. Dolfi, and M. Alouini, “Time delay generation at high frequency using SOA based slow and fast light,” *Opt Express*, vol. 19, no. 22, pp. 21180–21188, 2011.

[9] M. Pu *et al.*, “Widely tunable microwave phase shifter based on silicon-on-insulator dual-microring resonator,” *Opt Express*, vol. 18, no. 6, pp. 6172–6182, 2010.

[10] M. Burla *et al.*, “On-chip CMOS compatible reconfigurable optical delay line with separate carrier tuning for microwave photonic signal processing,” *Opt Express*, vol. 19, no. 22, pp. 21475–21484, 2011.

[11] Pérez López Daniel, “Integrated Microwave Photonic Processors using Waveguide Mesh Cores,” Universitat Politècnica de València, Valencia, 2017.

[12] J. Capmany and D. Pérez, *Programmable integrated photonics*. Oxford University Press, 2020.

[13] D. Pérez *et al.*, “Multipurpose silicon photonics signal processor core,” *Nat Commun*, vol. 8, no. 1, p. 636, 2017.

[14] D. Pérez, I. Gasulla, and J. Capmany, “Field-programmable photonic arrays,” *Opt Express*, vol. 26, no. 21, pp. 27265–27278, 2018.

[15] L. Zhuang, C. G. H. Roeloffzen, M. Hoekman, K.-J. Boller, and A. J. Lowery, “Programmable photonic signal processor chip for radiofrequency applications,” *Optica*, vol. 2, no. 10, pp. 854–859, 2015.

[16] V. J. Urick, K. J. Williams, and J. D. McKinney, *Fundamentals of microwave photonics*. John Wiley & Sons, 2015.

[17] D. Marpaung, J. Yao, and J. Capmany, “Integrated microwave photonics,” *Nat Photonics*, vol. 13, no. 2, pp. 80–90, 2019.

[18] J. Yao and J. Capmany, “Microwave photonics,” *Science China Information Sciences*, vol. 65, no. 12, p. 221401, 2022.

[19] C. J. S. R. A. Pérez López Daniel and Gasulla Ivana, “Honeycomb lattice meshes for reconfigurable universal microwave photonics processors,” *SPIE - Real-time Photonic Measurements, Data Management, and Processing II*, vol. 10026, p. 1002602, 2016.

[20] W. Bogaerts *et al.*, “Programmable photonic circuits,” *Nature*, vol. 586, no. 7828, pp. 207–216, 2020.

[21] A. Sobhanan *et al.*, “Semiconductor optical amplifiers: recent advances and applications,” *Adv Opt Photonics*, vol. 14, no. 3, pp. 571–651, 2022.

[22] Michael J Connelly, *Semiconductor optical amplifiers*. Springer Science & Business Media, 2007.

[23] W. Bogaerts *et al.*, “Programmable photonic circuits,” *Nature*, vol. 586, no. 7828, pp. 207–216, Oct. 2020, doi: 10.1038/s41586-020-2764-0.

[24] D. Pérez-López, A. M. Gutierrez, E. Sánchez, P. DasMahapatra, and J. Capmany, “Integrated photonic tunable basic units using dual-drive directional couplers,” *Opt Express*, vol. 27, no. 26, pp. 38071–38086, 2019.

[25] D. Pérez-López, E. Sánchez, and J. Capmany, “Programmable true time delay lines using integrated waveguide meshes,” *Journal of Lightwave Technology*, vol. 36, no. 19, pp. 4591–4601, 2018.

[26] D. Pérez, I. Gasulla, J. Capmany, and R. A. Soref, “Reconfigurable lattice mesh designs for programmable photonic processors,” *Opt Express*, vol. 24, no. 11, pp. 12093–12106, 2016.

[27] D. Perez *et al.*, “Silicon photonics rectangular universal interferometer,” *Laser Photon Rev*, vol. 11, no. 6, p. 1700219, 2017.

[28] E. Knill, R. Laflamme, and G. J. Milburn, “A scheme for efficient quantum computation with linear optics,” *Nature*, vol. 409, no. 6816, pp. 46–52, 2001.

[29] P. Kok, W. J. Munro, K. Nemoto, T. C. Ralph, J. P. Dowling, and G. J. Milburn, “Linear optical quantum computing with photonic qubits,” *Rev Mod Phys*, vol. 79, no. 1, p. 135, 2007.

[30] J. L. O’brien, A. Furusawa, and J. Vučković, “Photonic quantum technologies,” *Nat Photonics*, vol. 3, no. 12, pp. 687–695, 2009.

[31] M. G. Thompson, A. Politi, J. C. F. Matthews, and J. L. O’Brien, “Integrated waveguide circuits for optical quantum computing,” *IET circuits, devices & systems*, vol. 5, no. 2, pp. 94–102, 2011.

[32] A. Politi, J. C. F. Matthews, M. G. Thompson, and J. L. O’Brien, “Integrated quantum photonics,” *IEEE Journal of Selected Topics in Quantum Electronics*, vol. 15, no. 6, pp. 1673–1684, 2009.

[33] A. Politi, M. J. Cryan, J. G. Rarity, S. Yu, and J. L. O’brien, “Silica-on-silicon waveguide quantum circuits,” *Science (1979)*, vol. 320, no. 5876, pp. 646–649, 2008.

[34] K. Kieling, J. L. O’Brien, and J. Eisert, “On photonic controlled phase gates,” *New J Phys*, vol. 12, no. 1, p. 13003, 2010.

[35] J. B. Spring *et al.*, “Boson sampling on a photonic chip,” *Science (1979)*, vol. 339, no. 6121, pp. 798–801, 2013.

[36] M. A. Broome *et al.*, “Photonic boson sampling in a tunable circuit,” *Science (1979)*, vol. 339, no. 6121, pp. 794–798, 2013.

[37] A. Crespi *et al.*, “Integrated multimode interferometers with arbitrary designs for photonic boson sampling,” *Nat Photonics*, vol. 7, no. 7, pp. 545–549, 2013.

[38] Y. Shen *et al.*, “Deep learning with coherent nanophotonic circuits,” *Nat Photonics*, vol. 11, no. 7, pp. 441–446, 2017.

[39] H.-T. Peng, M. A. Nahmias, T. F. De Lima, A. N. Tait, and B. J. Shastri, “Neuromorphic photonic integrated circuits,” *IEEE Journal of Selected Topics in Quantum Electronics*, vol. 24, no. 6, pp. 1–15, 2018.

[40] D. P. López, “Programmable integrated silicon photonics waveguide meshes: optimized designs and control algorithms,” *IEEE Journal of Selected Topics in Quantum Electronics*, vol. 26, no. 2, pp. 1–12, 2019.

[41] J. C. Mikkelsen, W. D. Sacher, and J. K. S. Poon, “Dimensional variation tolerant silicon-on-insulator directional couplers,” *Opt Express*, vol. 22, no. 3, pp. 3145–3150, 2014.

[42] D. Pérez and J. Capmany, “Scalable analysis for arbitrary photonic integrated waveguide meshes,” *Optica*, vol. 6, no. 1, pp. 19–27, 2019.

[43] A. López, D. Pérez, P. DasMahapatra, and J. Capmany, “Auto-routing algorithm for field-programmable photonic gate arrays,” *Opt Express*, vol. 28, no. 1, pp. 737–752, 2020.

[44] D. S. Gunderson, *Handbook of mathematical induction: Theory and applications*. CRC Press, 2014.

[45] D. Pérez-López, A. López, P. DasMahapatra, and J. Capmany, “Multipurpose self-configuration of programmable photonic circuits,” *Nat Commun*, vol. 11, no. 1, p. 6359, 2020.

[46] B. J. Shastri *et al.*, “Photonics for artificial intelligence and neuromorphic computing,” *Nat Photonics*, vol. 15, no. 2, pp. 102–114, 2021.

[47] D. P. López, A. L. Hernández, P. DasMahapatra, and J. Capmany, “Field-Programmable Photonic Array for multipurpose microwave photonic applications,” in *2019 International Topical Meeting on Microwave Photonics (MWP)*, 2019, pp. 1–4.

[48] J. Yao, “Microwave photonics,” *Journal of lightwave technology*, vol. 27, no. 3, pp. 314–335, 2009.

[49] J. Capmany and D. Novak, “Microwave photonics combines two worlds,” *Nat Photonics*, vol. 1, no. 6, p. 319, 2007.

[50] T. Berceli and P. R. Herczfeld, “Microwave photonics—a historical perspective,” *IEEE Trans Microw Theory Tech*, vol. 58, no. 11, pp. 2992–3000, 2010.

[51] C. H. Cox III, “Analog Photonic Links: Theory and Practice.” Cambridge University Press, Cambridge, UK, 2004.

[52] I. Gasulla and J. Capmany, “Analytical model and figures of merit for filtered microwave photonic links,” *Opt Express*, vol. 19, no. 20, pp. 19758–19774, 2011.

[53] Y. Liu, A. Choudhary, D. Marpaung, and B. J. Eggleton, “Integrated microwave photonic filters,” *Adv Opt Photonics*, vol. 12, no. 2, pp. 485–555, 2020.

[54] Y. Liu, D. Marpaung, A. Choudhary, J. Hotten, and B. J. Eggleton, “Link performance optimization of chip-based Si 3 N 4 microwave photonic filters,” *Journal of lightwave technology*, vol. 36, no. 19, pp. 4361–4370, 2018.

[55] V. J. Urick, M. E. Godinez, P. S. Devgan, J. D. McKinney, and F. Bucholtz, “Analysis of an analog fiber-optic link employing a low-biased Mach–Zehnder modulator followed by an erbium-doped fiber amplifier,” *Journal of Lightwave Technology*, vol. 27, no. 12, pp. 2013–2019, 2009.

[56] T. Nakasyotani, H. Toda, T. Kuri, and K. Kitayama, “Wavelength-division-multiplexed millimeter-waveband radio-on-fiber system using a supercontinuum light source,” *Journal of lightwave technology*, vol. 24, no. 1, p. 404, 2006.

[57] C. G. Bottenfield, V. A. Thomas, and S. E. Ralph, “Analytic Equations for Photonic Frequency Converter Design,” *Journal of Lightwave Technology*, vol. 39, no. 24, pp. 7706–7715, 2021.

[58] E. Desurvire, “Erbium-doped fiber amplifiers,” *in Principle and applications*, 1992.

[59] INPHENIX, “Semiconductor Optical Amplifier Device (Booster Type),” Livermore, California, 2020.

[60] E. Sánchez, D. Pérez-López, J. Capmany, and others, “Modeling amplified arbitrary filtered microwave photonic links and systems,” *Opt Express*, vol. 29, no. 10, pp. 14757–14772, 2021.

[61] G. Roelkens *et al.*, “Micro-transfer printing for heterogeneous Si photonic integrated circuits,” *IEEE Journal of Selected Topics in Quantum Electronics*, vol. 29, no. 3: Photon. Elec. Co-Inte. and Adv. Trans. Print., pp. 1–14, 2022.